

**BOND ORDER POTENTIALS FOR ATOMISTIC STUDIES OF  
DISLOCATIONS AND OTHER EXTENDED DEFECTS IN TiAl**

Stefan Znám

A Dissertation

in

Materials Science and Engineering

Presented to the Faculties of the University of Pennsylvania in Partial  
Fulfillment of the Requirements for the Degree of Doctor of Philosophy

2001

---

Professor Vaclav Vitek  
Supervisor of Dissertation

---

Professor Peter Davies  
Graduate Group Chairperson

To my father ...

## ACKNOWLEDGMENTS

I would like to express my greatest thanks to Professor Vaclav Vitek, my academic advisor, whom I am indebted not only for his excellent scientific guidance, but also for his personal encouragement, fatherly patience, help and willingness to share his extensive knowledge and experience.

I owe an incalculable amount to Dr. Duc Nguyen-Manh from the University of Oxford, through whose vital help and scientific contribution the construction of the Bond Order Potential for TiAl was possible. I very much appreciated all his friendship and support. I would like to thank Professor David G. Pettifor from the University of Oxford for providing his valuable suggestions and deep scientific insight. I am indebted to Dr. Mojmír \_ob and Dr. Václav Paidar from the Czech Academy for their advice and encouragement. I also want to express my thanks to current and former members of Prof. Vitek's group – Dr. Roman Siegl, Dr. Alexey Girshick, Dr. Khantha, Dr. Kazuhiro Ito, and Dr. Mang-Mang Ling - for their help and interest in my work.

I owe my greatest appreciation to many people from the LRSM, most of all to Ms. Irene Clements and Ms. Pat Overend, whose help, kindness and good humor were enlightening my stay at LRSM. I would also like to thank all my friends, especially Zden\_k Bene\_, Matou\_ Mrov\_c and Radoslav Po\_ízek, since their friendship and support accompanied me through all the ups and downs of my graduate student life.

My greatest thanks belong to my mother, for her support and constant readiness to help in the moments of need. Finally, I want to thank my wife, Dana, for all her love, patience, understanding, and unconditional support.

## ABSTRACT

# BOND ORDER POTENTIALS FOR ATOMISTIC STUDIES OF DISLOCATIONS AND OTHER EXTENDED DEFECTS IN TiAl

Stefan Znám

Dr. Václav Vítek

The main theme of this thesis is development of potentials that are a necessary precursor for computer simulations of lattice defects in TiAl at atomic level. Extended defects, such as dislocations and stacking-fault type defects, play an important role in controlling the overall mechanical behavior of crystalline materials. Understanding their key structural properties at the atomistic level is a necessary prerequisite for gaining a deeper insight into the macroscopic scale deformation processes. The main focus of the computer simulation presented in this work is on studying the core structure of dislocations in L<sub>1</sub><sub>0</sub> TiAl. Results of atomistic simulation of dislocation cores provide then a framework for analyzing the experimentally observed deformation modes in this material. An appropriate description of atomic interactions is needed for physically meaningful computer simulation studies. For this purpose a substantial part of this thesis was devoted to the development of the Bond order potentials (BOP) for TiAl. BOP represents a semi-empirical real-space tight-binding based scheme that is computationally efficient and at the same time capable to capture directionality of bonding arising from the unfilled *d* band in this material. The new BOP for TiAl was extensively tested and its

ability to describe different bonding environments in both TiAl and  $Ti_3Al$  demonstrated. Using this potential the core structures and possible dissociations of both the ordinary  $1/2\langle 110 \rangle$  dislocation and the  $\langle 101 \rangle$  superdislocation were investigated together with the energies of stacking fault type defects participating in dislocation splitting. Our results for the ordinary  $1/2\langle 110 \rangle$  dislocations indicate the existence of a non-planar core for screw and 60 degrees mixed dislocations. This core structure renders these dislocations sessile. In the case of the  $[10\bar{1}]$  it is observed to dissociate into partial dislocations and the two following configurations were found in our simulations:

$$[10\bar{1}] = 1/6[11\bar{2}] + SISF + 1/2[10\bar{1}] + CSF + 1/6[2\bar{1}\bar{1}]$$

$$[10\bar{1}] = 1/6[11\bar{2}] + SISF_{(111)} + 1/3[20\bar{1}] + SISF_{(1\bar{1}1)} + 1/6[1\bar{1}\bar{2}]$$

A planar configuration and a configuration spreading into two intersecting  $\{111\}$  type planes, which is, presumably, sessile.

## TABLE OF CONTENTS

Title	i
Acknowledgements	iii
Abstract	iv
Table of Contents	vi
List of Tables	x
List of Figures	xvi
<b>1. INTRODUCTION</b>	<b>1</b>
<b>2. INTRODUCTION TO Ti-Al ALLOYS</b>	<b>5</b>
2.1. Mechanical Properties of $\gamma$ -Ti-Al Alloys	5
<b>3. COMPUTER MODELING OF EXTENDED DEFECTS</b>	<b>28</b>
3.1. Modeling of the $\gamma$ -surfaces and Stacking Fault-Type Defects	30
3.2. Modeling of the Dislocation Core Structure	32

<b>4. BOND ORDER POTENTIALS</b>	<b>35</b>
4.1. The Tight-Binding Method	35
4.2. The Moment Theorem	49
4.3. The Recursion Method and the Green's Function Formalism	51
4.4. Many-Body Expansion for the Bond-Order	57
4.5. Truncating the Many-Body Expansion and Using the Sum Rules	66
4.6. Effective Electronic Temperature	71
<b>5. TRANSFERABILITY OF THE HAMILTONIAN MATRIX ELEMENTS AND THE CAUCHY PRESSURES PROBLEM</b>	<b>73</b>
5.1. The Hamiltonian Matrix Elements and their Transferability	73
5.2. The Problem of Negative Cauchy Pressures and the Environment- Dependent Term	79
<b>6. CONSTRUCTION OF BOPs FOR Ti AND TiAl</b>	<b>82</b>
6.1. Bond Order Potentials for hcp Ti	85
6.1.1. Construction of the Bond Part of BOPs for hcp Ti	86
6.1.2. Fitting of the Environmentally Dependent Repulsive Term	93

6.1.3. Fitting of the Pair Potential of BOPs for hcp Ti	96
6.2. Bond Order Potentials for TiAl	103
6.2.1. Construction of the Bond Part of BOPs for TiAl	104
6.2.2. Fitting of the Environmentally Dependent Term of BOPs for TiAl	110
6.2.3. Fitting of the Pair Potential of BOPs for TiAl	113
6.2.4. BOPs for TiAl with c/a =1.	119
<b>7. TESTING AND SOME APPLICATIONS OF THE BOND ORDER POTENTIALS FOR TiAl</b>	<b>122</b>
7.1. Testing of the Potentials	122
7.2. The (111) $\gamma$ -surface, Energies of Stacking-fault Type Defects and Interfaces	130
7.3. Point Defects	138
<b>8. STUDIES OF DISLOCATIONS IN L1<sub>0</sub> TiAl</b>	<b>143</b>
8.1. Review of Experimental Observations of Dislocations in L1 <sub>0</sub> TiAl	143
8.2. Atomistic Studies of $\langle 110 \rangle$ Type Ordinary and Superdislocations in L1 <sub>0</sub> TiAl	147
8.2.1. Ordinary 1/2 $\langle 110 \rangle$ Dislocation	148
8.2.2. $\langle 101 \rangle$ Superlattice Dislocation	154

8.3. Elastic Analysis of Ordinary and Super Dislocations in L1 <sub>0</sub> TiAl	161
8.4. Discussion of Results	170
<b>9. SUGGESTIONS FOR FUTURE RESEARCH</b>	<b>175</b>
<b>BIBLIOGRAPHY</b>	<b>180</b>

## LIST OF TABLES

Table 2.1 Selected properties of various intermetallic materials for turbine engine applications. (According to Dimiduk, Miracle and Ward (1992)).	6
Table 6.1 Parameters of the bond part for BOPs for hcp Ti	92
Table 6.2 The bond part cut-off polynomial tail parameters for BOPs for hcp Ti	93
Table 6.3 Parameters of the environmentally dependent term for BOPs for hcp Ti	95
Table 6.4 Cut-off tail parameters used in the environmentally dependent term for BOPs for hcp Ti	96
Table 6.5. Parameters of the pair potential in the bond-order potential scheme for Ti. Parameters $a_i$ - in units of eV/ $\overset{\circ}{\text{A}}^3$ , $r_i$ - in units of $\overset{\circ}{\text{A}}$	102

Table 6.6 Fitted equilibrium properties of hcp Ti calculated using the bond-order potential compared with the corresponding experimental values. $E_{coh}$ (in eV) has been taken from Kittel 1986, lattice parameters $a$ and $c$ (in Å) - from Pearson 1967, elastic moduli (in eV/Å <sup>3</sup> ) - from Simmons and Wang 1971.	103
Table 6.7 Parameters of the bond part for BOPs for TiAl.	109
Table 6.8 The bond part cut-off polynomial tail parameters for BOPs for TiAl	110
Table 6.9 Parameters of the environmentally dependent term for BOPs for TiAl. Values of the two parameters for the cross-interaction between Ti and Al are calculated as $B^{TiAl} = \sqrt{B^{TiTi} B^{AlAl}}$ and $R_c^{TiAl} = \frac{1}{2}(R_c^{TiTi} + R_c^{AlAl})$ .	112
Table 6.10 Cut-off tail parameters used in the environmentally dependent term of BOPs for TiAl	113
Table 6.11 Parameters for the Al-Al pair-potential interaction of the Bond order potentials for TiAl Parameters $A_i$ - in units of eV/Å <sup>3</sup> , $R_i$ - in units of Å.	118
Table 6.12. Parameters for the Ti-Al pair-potential interaction of the Bond order potentials for TiAl. Parameters $a_i$ - in units of eV/Å <sup>3</sup> , $r_i$ - in units of Å.	118

Table 6.13 Properties of L1 <sub>0</sub> TiAl calculated using the bond-order potential. The experimental lattice parameters $a$ and $c$ (in $\text{\AA}^\circ$ ) were taken from Pearson 1967, the elastic moduli (in $\text{eV}/\text{\AA}^3$ ) - from Tanaka 1996.	119
Table 6.14 Parameters of the Al-Al pair-potential for BOPs predicting ideal c/a=1. Parameters $a_i$ – in units of $\text{eV}/\text{\AA}^3$ , $r_i$ - in units of $\text{\AA}^\circ$ .	120
Table 6.15 Parameters of the Ti-Al pair-potential for BOPs predicting ideal c/a=1. Parameters $a_i$ – in units of $\text{eV}/\text{\AA}^3$ , $r_i$ - in units of $\text{\AA}^\circ$ .	121
Table 7.1 Energy differences (in eV/atom) between alternate crystal structures with 1:1 composition and the L1 <sub>0</sub> structure calculated ab-initio (Sob <i>et al.</i> 1997) using the FP-LMTO method and using the constructed BOP.	122
Table 7.2 Equilibrium properties of DO <sub>19</sub> Ti <sub>3</sub> Al. Comparison of the experimental values with those calculated using BOPs for TiAl.	125
Table 7.3 Energies of stacking fault-type defects (in $mJ/m^2$ ) calculated using four different descriptions of atomic interactions.	133

Table 7.4 Energies of the APB, CSF and SISF on the (111) plane, in $mJ/m^2$ . (a) Hug, Loiseau and Veyssiere 1988; (b) Hug, Phan-Courson and Blanche 1995; (c) Stucke, Vasudevan and Dimiduk 1995; (d) Wiezorek and Humphreys 1995. Experiments were performed on Ti <sub>46</sub> Al <sub>54</sub> (a,b and d) and Ti <sub>44</sub> Al <sub>56</sub> (c) at room temperature.	133
Table 7.5 The energies of $\gamma/\gamma$ interfaces calculated using the BOPs for TiAl compared to FP-LMTO (Vitek, <i>et al.</i> 1997a), FP-LAPW (C.L. Fu, unpublished results) and Finnis-Sinclair (FS) data (Vitek <i>et al.</i> , 1997a). A simulation block of 60 atoms was used in the BOP calculations for the ordered twin and twin with APB, while in the calculations of the other two interfaces blocks consisting of 240 atoms were used..	138
Table 7.6 Raw energies of point defects in TiAl (in $eV$ ). Comparison of results calculated by Bond order potentials for TiAl with Finnis-Sinclair (FS) data (Nomura and Vitek, to be published ) and Embedded Atom Method (EAM) data (Mishin and Herzig, 2000).	141
Table 7.7 Effective energies of point defects in TiAl (in $eV$ ). Comparison of results calculated by Bond order potentials for TiAl with Finnis-Sinclair (FS) data (Nomura and Vitek, to be published), Embedded Atom Method (EAM) data (Mishin and Herzig, 2000) and two ab-initio calculations (Woodward <i>et al.</i> 1998, Fu and Yoo 1990).	141

Table 7.8 Effective formation energies of point defects preserving stoichiometry. Comparison of results calculated by Bond order potentials for TiAl with Finnis-Sinclair (FS) data (Nomura and Vitek, to be published), Embedded Atom Method (EAM) data (Mishin and Herzig, 2000) and two ab-initio calculations (Woodward <i>et al.</i> 1998, Fu and Yoo 1990).	142
Table 8.1 $1/2[1\bar{1}0] = 1/6[1\bar{2}1] + CSF + 1/6[2\bar{1}\bar{1}]$ splitting of the ordinary dislocation. Interaction energy coefficients and equilibrium width of splitting for the screw, 60°-mixed and edge orientations of the dislocation line.	163
Table 8.2 $[10\bar{1}] = 1/6[5\bar{1}\bar{4}] + SISF + 1/6[11\bar{2}]$ splitting of the superdislocation. Interaction energy coefficients, self-energy coefficients and equilibrium width of splitting for the screw orientation of the total dislocation.	164
Table 8.3 $[10\bar{1}] = 1/2[10\bar{1}] + APB + 1/2[10\bar{1}]$ splitting of the superdislocation. Interaction energy coefficients, self-energy coefficients and equilibrium width of splitting for the screw orientation of the total dislocation.	165
Table 8.4 $[10\bar{1}] = 1/6[11\bar{2}] + SISF_{(111)} + 1/3[20\bar{1}] + SISF_{(1\bar{1}1)} + 1/6[1\bar{1}\bar{2}]$ splitting of the superdislocation. Interaction energy coefficients, self-energy coefficients and equilibrium splitting distances for the screw orientation of the total dislocation.	166

Table 8.5  $[10\bar{1}] = 1/2[10\bar{1}] + APB + 1/6[2\bar{1}\bar{1}] + SISF + 1/6[11\bar{2}]$  splitting of the superdislocation. Interaction energy coefficients, self-energy coefficients and equilibrium splitting distances for the screw orientation of the total dislocation.

168

Table 8.6  $[10\bar{1}] = 1/6[2\bar{1}\bar{1}] + CSF + 1/2[10\bar{1}] + SISF + 1/6[11\bar{2}]$  splitting of the superdislocation. Interaction energy coefficients, self-energy coefficients and equilibrium splitting distances for the screw orientation of the total dislocation

170

## LIST OF FIGURES

Figure 2.1 Phase diagram for Ti-Al system (after McCullough et al. 1989).

The shaded area corresponds to the fully lamellar structure.

7

Figure 2.2 tetragonal L<sub>1</sub><sub>0</sub> unit cell

8

Figure 2.3 hexagonal DO<sub>19</sub> structure

8

Figure 2.4 TiAl lamellar structure (Inui et al. 1992b)

10

Figure 2.5 PST - schematic picture

11

Figure 2.6 Polysynthetically twinned (PST) single crystal (Yamaguchi and

Inui 1993)

11

Figure 2.7 Burgers vectors of the 1/2⟨110], 1/2⟨112] and ⟨101] dislocations

in the L<sub>1</sub><sub>0</sub> structure.

13

Figure 2.8 Yield stress of the PST crystal as a function of the angle of the

loading axis with respect to the plane parallel to the lamellar boundaries.

(After Fujiwara *et al.* 1990).

15

Figure 2.9 Elongation to fracture of the PST crystal as a function of the angle  
of the loading axis with respect to the plane parallel to the lamellar boundaries  
(After Inui *et al.* 1992c).

16

Figure 2.10 PST loading experiment

16

Figure 2.11 “B” orientation

19

Figure 2.12 “N” orientation

19

Figure 2.13 “A” orientation

20

Figure 2.14 The (111) plane in the L<sub>1</sub><sub>0</sub> TiAl.

20

Figure 2.15 120° rotational fault

24

Figure 2.16 Twin

25

Figure 2.17 Pseudotwin

25

Figure 2.18 Stacking faults on the (111) plane in the L<sub>1</sub><sub>0</sub> TiAl

27

Figure 3.1 Schematic picture of the atomic block used in the $\gamma$ -surface calculations.	32
Figure 3.2 Schematic picture of the atomic block used in the dislocation calculations.	34
Figure 5.1 Electronic density of states of TiAl. Comparison of the full ab-initio (TB-LMTO) and the p-d TB model.	75
Figure 5.2 Bonding integrals in Ti-Al alloys calculated using TB-LMTO as a function of the separation of atoms.	78
Figure 6.1 The radial part of the $dd\sigma$ bond integral.	90
Figure 6.2 The radial part of the $dd\pi$ bond integral	91
Figure 6.3 The Ti-Ti pair potential.	100
Figure 6.4 The radial part of the $dp\sigma$ bond integral.	107
Figure 6.5 The radial part of the $dp\pi$ bond integral.	107

Figure 6.6 The radial part of the  $pp\sigma$  bond integral. 108

Figure 6.7 The radial part of the  $pp\pi$  bond integral. 108

Figure 6.8 The Ti-Al and Al-Al pair potentials. 116

Figure 7.1 Energy surface (in  $meV/atom$ ) for large homogeneous deformation of TiAl unit cell. 123

Figure 7.2 Tetragonal transformation. Comparison of BOPs (circles) with FP-LAPW ab-initio data (diamonds) from Paidar *et al.* (1999). A unit cell consisting of 2 atoms was used in the BOP calculation. 126

Figure 7.3 Trigonal transformation. Comparison of BOPs (circles) with FP-LAPW ab-initio data (diamonds) from Paidar *et al.* (1999). A unit cell consisting of 12 atoms was used in the BOP calculation. 127

Figure 7.4 Hexagonal transformation. Comparison of BOPs (circles) with FP-LAPW ab-initio data (diamonds) from Paidar *et al.* (1999). A unit cell consisting of 4 atoms was used in the BOP calculation. 128

Figure 7.5  $\gamma$ -surface for (111) plane in  $mJ/m^2$  – surface plot. A simulation block consisting of 60 atoms was used in the calculation.

131

Figure 7.6  $\gamma$ -surface for (111) plane in  $mJ/m^2$  – contour plot. A simulation block consisting of 60 atoms was used in the calculation.

132

Figure 7.7 The energy profile in the vicinity of the APB along the  $[1\bar{1}\bar{2}]$  direction. The x-axis measures the displacement from the APB in fractions of the  $\frac{1}{6}[1\bar{1}\bar{2}]$  vector.

136

Figure 8.1 The non-planar core of the  $1/2[1\bar{1}0]$  ordinary screw dislocation in TiAl depicted by the plot of the screw component parallel to  $[1\bar{1}0]$ .

151

Figure 8.2 The core structure of the  $1/2[1\bar{1}0]$  ordinary  $60^\circ$  mixed dislocation in TiAl depicted by the component of the displacement along the  $[10\bar{1}]$  direction (screw component).

152

Figure 8.3 The core structure of the  $1/2[1\bar{1}0]$  ordinary  $60^\circ$  mixed dislocation in TiAl depicted by the component of the displacement along the  $[\bar{1}2\bar{1}]$  direction (edge component).

153

Figure 8.4 The non-planar core of the screw  $[10\bar{1}]$  superdislocation split

into two  $\{111\}$  planes, forming a pair of SISFs, depicted by the screw component of the displacement.

157

Figure 8.5 The non-planar core of the screw  $[10\bar{1}]$  superdislocation split into two  $\{111\}$  planes, forming a pair of SISFs, depicted by the edge component of the displacement.

158

Figure 8.6 The planar core of the screw  $[10\bar{1}]$  superdislocation depicted by the screw component of the displacement.

159

Figure 8.7 The planar core of the screw  $[10\bar{1}]$  superdislocation depicted by the edge component of the displacement in the  $[\bar{1}2\bar{1}]$  direction.

160

## 1. INTRODUCTION

Titanium-aluminides, in particular  $\gamma$ -TiAl, belong to a very promising class of intermetallics with a broad variety of prospective applications as high-temperature materials. Among the most notable properties of the titanium-aluminides are their low weight, high strength, high melting temperature, superior oxidation and corrosion resistance. However, the limited ductility is the major impediment to large-scale utilization of these materials. Improved ductility can be achieved via inventive metallurgical processing. Aluminum rich alloys have a single phase ( $\gamma$ ) tetragonal L<sub>1</sub><sub>0</sub> structure, but near stoichiometric and titanium-rich alloys exhibit two-phase lamellar structure, consisting of layers of tetragonal L<sub>1</sub><sub>0</sub> TiAl and hexagonal DO<sub>19</sub> Ti<sub>3</sub>Al. Interestingly, the most ductile material is this two-phase lamellar alloy although its components are quite brittle in single crystalline form. The reasons behind this are not fully understood. Gaining deeper insight into the mechanical behavior of the material by means of both experimental and theoretical techniques is therefore important as it can lead to new processing technologies resulting in further enhancement of the ductility as well as improvement of other properties of titanium aluminides.

The ductility of a crystalline material is principally controlled by the motion of dislocations. It is a common feature of complex crystal structures that certain dislocations possess non-planar cores which impedes their glide (Duesberry and Richardson 1991; Vitek 1992). This characteristic of the atomic structure of dislocations

is further enhanced if the covalent component of bonding is significant, which is the case of TiAl-alloys. While dislocations with planar cores can usually glide relatively easily, those with non-planar cores are more difficult to move, since the core spreading into several planes is an obstacle to the dislocation glide. Such dislocations are commonly called sessile. The core structures of dislocations, therefore, play a key role in controlling the overall mechanical behavior. Fundamental understanding of these problems can be attained only at the atomic level by analyzing dislocations, stacking-fault type defects and interfaces present in the material. Detailed behavior of these extended defects at atomic level can be extremely complex and the only plausible way of studying such phenomena is by means of computer simulation. Moreover, comparing results of computer simulations with experiments can serve as a validation of analytical models and verification of the underlying fundamental theories. The computer simulation thus provides the much needed link between theory and experiment and between analyses on different scales.

An appropriate description of atomic interactions is an essential precursor for physically meaningful computer simulation studies. While the density functional theory and local density approximation (DFT-LDA) based ab-initio calculations are at present the state of the art, they are severely limited by the number of independent atoms that can be treated in such studies. Dislocations posses long-range elastic strain fields and therefore thousands of atoms may have to be included in dislocation calculations, in particular when studying their motion. Simple alternatives, such as the embedded-atom method or Finnis-Sinclair type potentials (Daw and Baskes 1984; Finnis and Sinclair

1984), that proved valuable in some metallic systems, are central force schemes and not sufficient if the covalent bonding is significant, which is the case of titanium aluminides (Fu and Yoo 1990; Woodward, Maclare and Rao 1991; Song *et al.* 1994; Siegl *et al.* 1997). What is then needed is an advanced semi empirical framework in which the required covalent character of bonding is explicitly included. The tight-binding method is a simple and elegant solution. In recent years the tight-binding approach has been reformulated in terms of the Bond Order Potentials (BOP) (Pettifor 1989; Pettifor and Aoki 1991; Pettifor 1995; Horsfield *et al.* 1996; Bowler *et al.* 1997) using the orthogonal basis and two-center hopping integrals. The BOPs, that are a real space technique, are very well suited for the above mentioned atomistic studies. They do not require the use of periodic boundary conditions that can be very limiting when dealing with extended defects such as dislocations. Moreover, the requirement of the local charge neutrality ensures that the method is partially self-consistent. In the course of this work Bond Order Potentials for Ti-Al have been developed. Testing of these potentials presented in this thesis demonstrates their capability to describe the atomic interactions in a broad variety of structures. Consequently, they serve well their purpose as a valuable tool for the intended atomistic studies of extended defects.

Studies of this type constitute then the second part of this thesis. Most importantly, the core structures and possible dissociations of both the ordinary  $1/2\langle 110 \rangle$  dislocation and the  $\langle 101 \rangle$  superdislocation are investigated together with the energies of stacking fault type defects participating in dislocation splitting. A number of computer simulations of the structure and properties of dislocations in TiAl have been made in the past

(Simmons, Rao and Dimiduk, 1993, Panova and Farkas 1995; Girshick, 1997). In all these works potentials based on central-force schemes were used to describe the atomic interactions in the material. Such potentials do not capture effects arising from covalent bonding and this is the reason why we decided to pursue the uneasy task of developing the Bond Order Potentials. The newly constructed potentials enabled us to account for the directionality of bonding and thus achieve a new and physically more founded insight into the atomistic behavior of extended defects in TiAl.

The thesis is divided into nine chapters. Chapter 1 gives a brief introduction and states the research problems that are addressed in the thesis. Chapter 2 comprises a general overview of structural and mechanical properties of TiAl alloys. In Chapter 3 modeling techniques employed in our studies of interfaces and dislocations are summarized. In Chapter 4 the fundamental theory behind the BOPs is presented in detail. Chapter 5 addresses the important issue of the transferability of bond integrals that are the most important physical quantities entering BOPs, and discusses the origin of the negative Cauchy pressures which leads to introduction of an additional empirical term to BOP. Chapter 6 gives a detailed account on the construction of the BOPs for TiAl developed in the course of this work. Testing of the potentials by comparison of results with experiments and other theoretical works is presented in Chapter 7. The results of our studies of dislocation cores in TiAl and their implications for the deformation behavior of TiAl, are presented in Chapter 8. Finally, Chapter 9 contains several suggestions for future research.

# 1. INTRODUCTION TO Ti-Al ALLOYS

## 1.1. Mechanical Properties of $\gamma$ -Ti-Al Alloys

Intermetallic compounds represent a class of ordered alloys that do not undergo order-disorder transition but remain ordered up to the melting. Their unique thermal and mechanical properties have attracted the attention of both the industrial and scientific community in the past two decades. The low specific weight and high melting temperature of many intermetallic alloys promise a broad range of application in the aerospace and automotive industry. With their high elevated-temperature strength, good resistance to oxidation and hydrogen absorption, together with excellent creep properties, these materials outperform the conventional alloys. Some intermetallics, such as NiAl-based alloys and Fe-Al alloys, have already been used for a long time. Among the most promising emerging intermetallic candidates are the  $\gamma$ -TiAl based alloys. In addition to the light weight, it is their high stiffness and excellent burn resistance that stand behind their prospective use in areas such as aircraft turbine blades or automobile exhaust valves (Dimiduk 1999). Table 1.1 shows a comparison of mechanical and thermal properties of several intermetallic materials. From this it can be seen that  $\gamma$ -TiAl alloys exhibit the best overall combination of properties among the materials listed. They have a very low density while displaying excellent creep and oxidation limits at the same time. These advantages however do not come without attendant drawbacks. The main problem with titanium-aluminides is their limited room-temperature ductility and also the relatively low fracture toughness. These limitations prohibit the use of inexpensive manufacturing

techniques such as casting and forging (Yamaguchi and Inui 1993) and thus impose a serious obstacle to large-scale production of  $\gamma$ -TiAl alloys. Detailed understanding of the key factors governing the mechanical behavior is therefore of a great importance.

	Density [g cm <sup>-3</sup> ]	Elastic Modulus [Mbar]	Room Temperature Fracture Toughness [MN m <sup>-3/2</sup> ]	Tensile Creep Limit [° C]	Oxidation Limit [° C]
Ti – based Superalloys	<b>4.5</b>	<b>1.10</b>	<b>35-60</b>	<b>600</b>	<b>600</b>
Ni – based Superalloys	<b>8.3</b>	<b>1.25</b>	<b>30-35</b>	<b>1100</b>	<b>&gt; 1100</b>
Ti <sub>3</sub> Al ( $\alpha_2$ )	<b>4.3</b>	<b>1.45</b>	<b>25</b>	<b>800</b>	<b>650</b>
TiAl ( $\gamma$ )	<b>3.8</b>	<b>1.76</b>	<b>25</b>	<b>950</b>	<b>900</b>
NiAl	<b>5.9</b>	<b>1.93</b>	<b>12-15</b>	<b>1100</b>	...
MoSi <sub>2</sub>	<b>6.5</b>	<b>3.79</b>	<b>4-5</b>	...	<b>&gt; 1700</b>
Nb-10at%Si	<b>7.5</b>	<b>1.45</b>	<b>25</b>	...	<b>~ 400</b>

Table 1.1 Selected properties of various intermetallic materials for turbine engine applications.

(According to Dimiduk, Miracle and Ward (1992)).

Depending on the composition, Ti-Al alloys exhibit a wide variety of microstructural forms with different mechanical properties. Figure 1.1 shows a part of the phase diagram for the Ti-Al system. The main constituent stoichiometric phases of interest are the TiAl tetragonal L1<sub>0</sub> structure (called the  $\gamma$ -phase) which corresponds to

50:50 composition and the  $\text{Ti}_3\text{Al}$  hexagonal  $\text{DO}_{19}$  structure ( $\alpha_2$ -phase) with 75:25 composition. The  $\text{L}1_0$  structure (Figure 1.2) is fcc-based and consists of alternating (002) planes of pure titanium and aluminum. The unit cell is non-cubic not only due to the non-ideal  $c/a$  ratio ( $c/a=1.016$ , from Pearson 1967) but also due to the presence of different species in the structure. The hexagonal  $\text{DO}_{19}$  structure is shown in Figure 1.3.

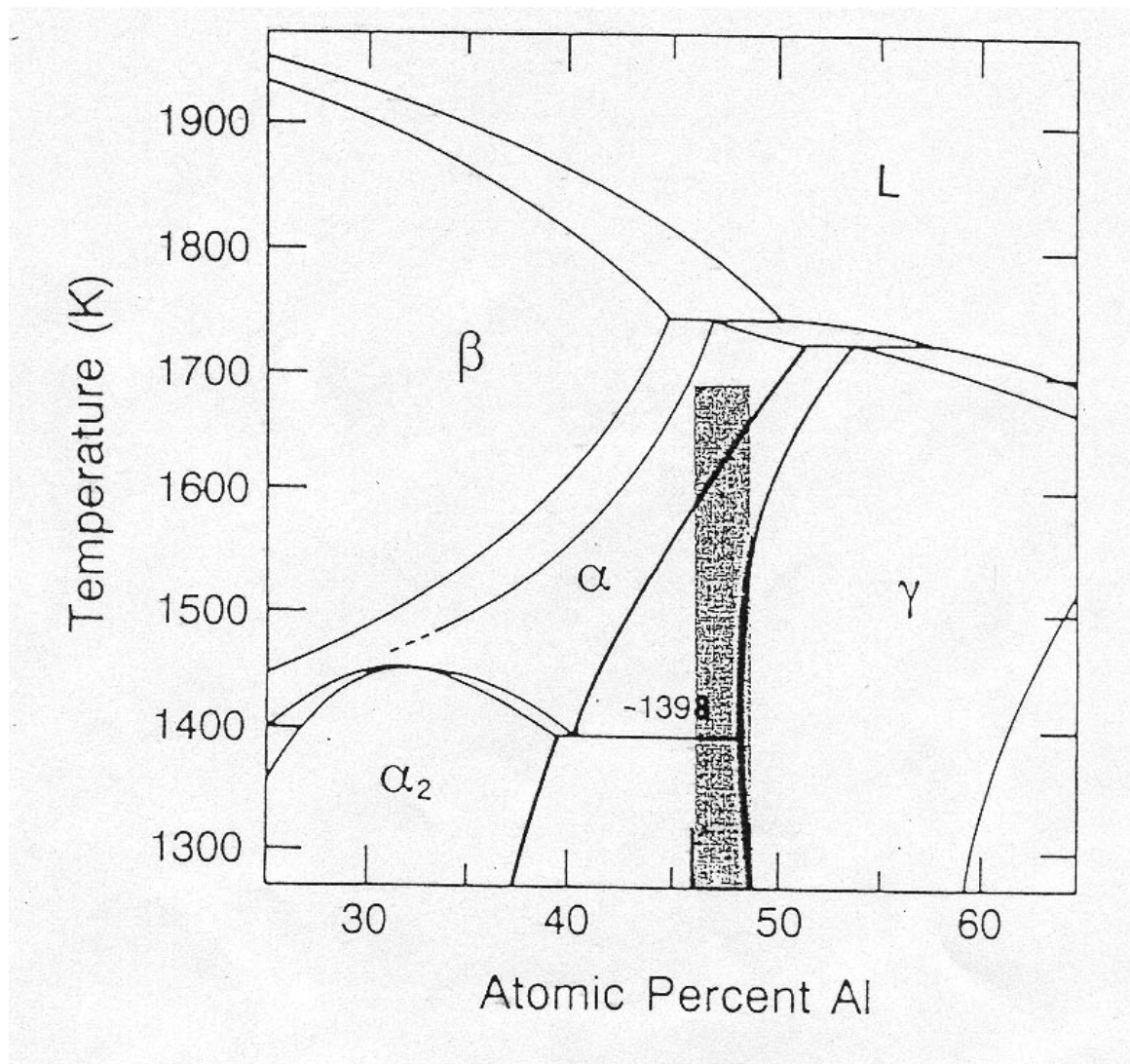


Figure 1.1 Phase diagram for Ti-Al system (after McCullough et al. 1989). The shaded area corresponds to the fully lamellar structure.

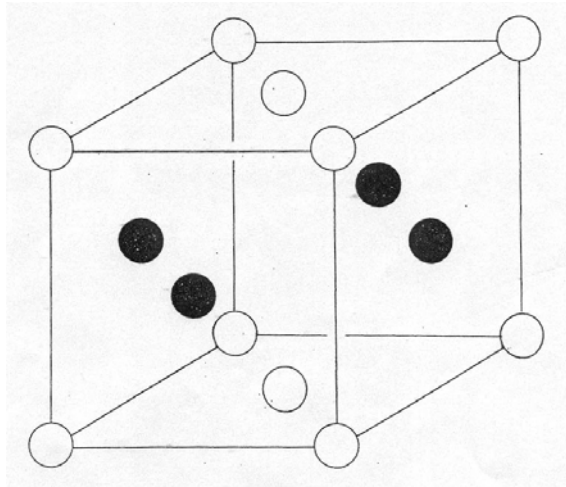


Figure 1.2 tetragonal  $L1_0$  unit cell

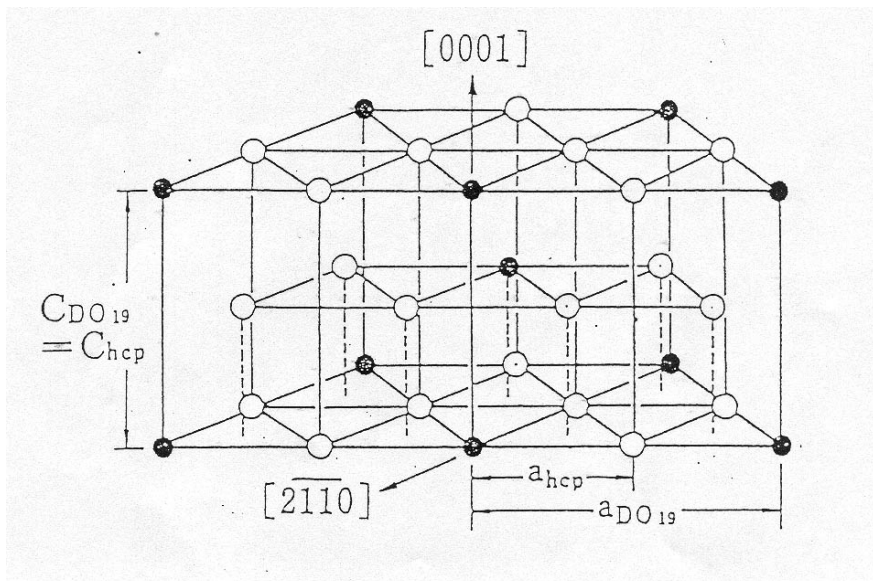


Figure 1.3 hexagonal  $DO_{19}$  structure

The  $\gamma$ -Ti-Al corresponds to the region on the phase diagram near the stoichiometric composition. The microstructural form and consequently the thermal and mechanical properties vary strongly with the Al content. The Al-rich region, for Al content above 54at%, results in a pure  $\gamma$ -phase polycrystalline structure while Al-concentrations below 49at % exhibit the so-called lamellar polycrystalline structure. For the region in between, Al content 49-54at% the resulting structure is a mixture of  $\gamma$  grains and grains with lamellar microstructure, also called the duplex structure.

The polycrystalline lamellar structure shown in Figure 1.4 consists of grains formed as stacks of parallel lamellae of  $\gamma$  and  $\alpha_2$  phase. Due to the nearly equiatomic composition, majority of the lamellae are of the  $\gamma$ -type (TiAl) and the occasionally occurring  $\alpha_2$ -lamellae ( $Ti_3Al$ ) only compensate for the higher Ti content. As a result of the lamellar stacking, there are many interfaces present in the structure (mostly of  $\gamma/\gamma$  and  $\gamma/\alpha_2$  type - again for compositional reasons) which dramatically influence the mechanical behavior of the material. It has been found that the lamellar interfaces always occur on the close-packed planes, namely  $\{111\}$  planes in  $L1_0$  and  $\{0001\}$  planes in the hexagonal  $DO_{19}$  (Inui *et al.* 1992b). As will be described later, the lamellar character, surprisingly, leads to improved mechanical properties, namely higher room-temperature ductility which is practically zero for TiAl in the pure  $\gamma$ -phase structure (Yamaguchi *et al.*, 1995). This phenomenon is evidently due to the presence of lamellar boundaries in the material. In order to study the mechanical properties of the lamellae and the consequences of the

presence of the lamellar boundaries on the mechanical behavior, Fujiwara *et al.*, 1990, grew “single” crystals of the lamellar structure, the so-called polysynthetically twinned (PST) crystals. Twinning is very frequent in the PST crystals, hence the name that comes from an analogous phenomenon of polysynthetical twinning in some geological materials. A PST crystal is shown schematically in Figure 1.5 while Figure 1.6 shows an experimental image of the PST structure.

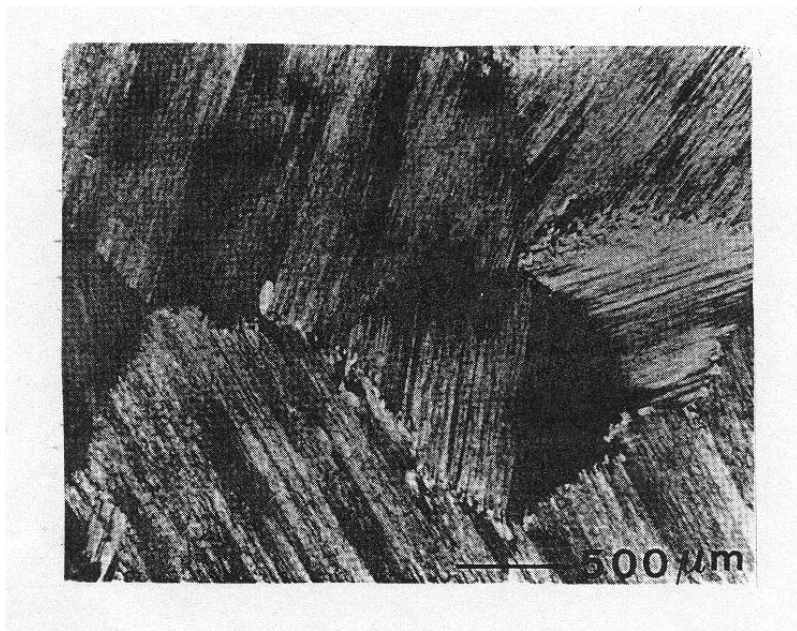


Figure 1.4 TiAl lamellar structure (Inui et al. 1992b)

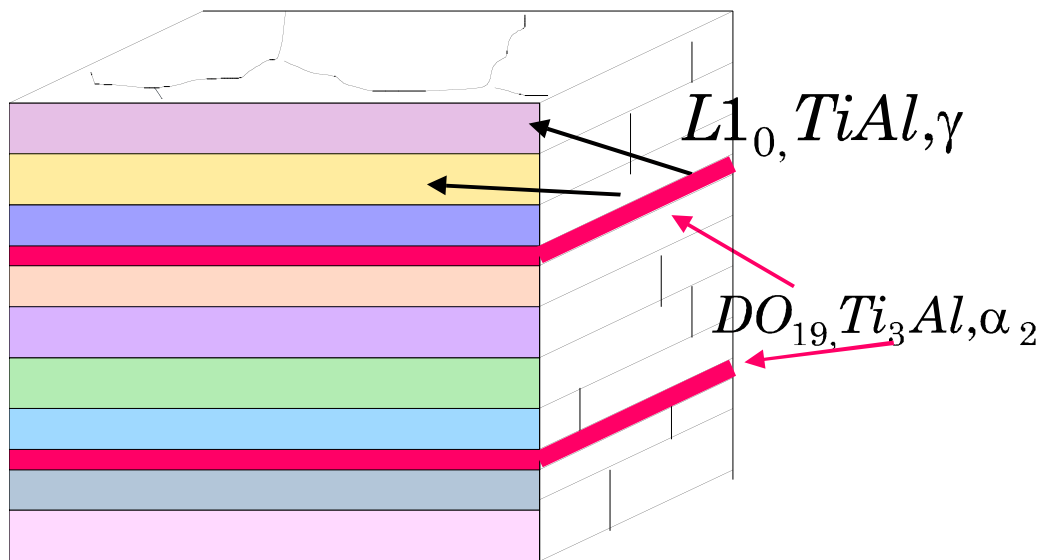


Figure 1.5 PST - schematic picture

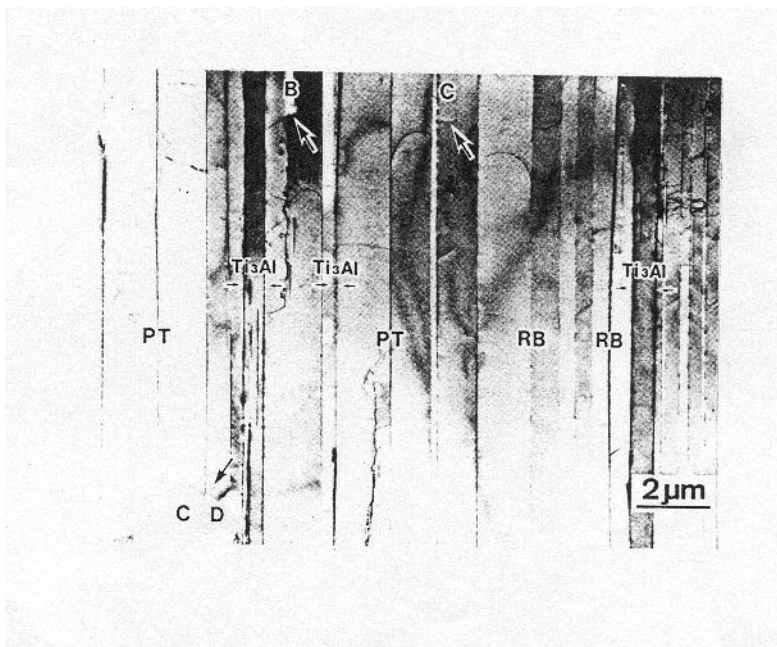


Figure 1.6 Polysynthetically twinned (PST) single crystal (Yamaguchi and Inui 1993)

Mechanical properties of  $\gamma$ -TiAl alloys depend very strongly on the microstructure and the composition of the material. Homogeneous duplex structures, for example, tend to have better ductility than the lamellar structures, but on the other hand the latter have higher fracture toughness and better high-temperature strength (Yamaguchi *et al.* 1995). The composition dependence is very pronounced in the case of the single crystals of the  $\gamma$ -phase. Their mechanical properties change with the composition so abruptly that, according to Yamaguchi *et al.* 1995, the alloy with Al content above 54at% can be regarded as a completely different material from the  $\gamma$ -phase present in two-phase  $\gamma$ -alloys. Thus, for proper understanding of the complex behavior of the  $\gamma$ -TiAl alloys it is important to consider the deformation mechanisms of both the constituent phases ( $\gamma$  and  $\alpha_2$ ) and the PST crystal.

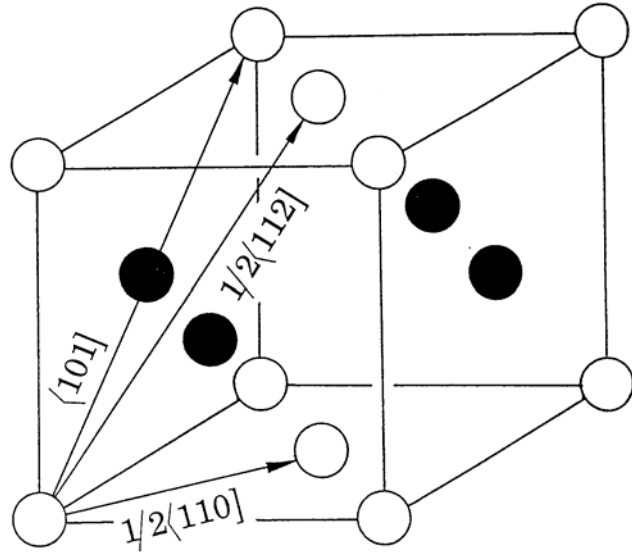


Figure 1.7 Burgers vectors of the  $1/2\langle 110 \rangle$ ,  $1/2\langle 112 \rangle$  and  $\langle 101 \rangle$  dislocations in the  $L1_0$  structure.

The main deformation modes in  $\gamma$ -TiAl are twinning and slip - both of them operating on the close-packed  $\{111\}$  planes. The slip can occur via three types of dislocations: two kinds of ordinary dislocations with Burgers vectors  $1/2\langle 110 \rangle$  and  $1/2\langle 112 \rangle$ , and a superdislocation with the Burgers vector  $\langle 101 \rangle$ . The  $1/2\langle 112 \rangle$  ordinary dislocation has a relatively long Burgers vector and is not observed to glide. The observed twinning is of the  $\{111\}\langle 11\bar{2} \rangle$  type. Since  $L1_0$  is a fcc-derived structure it is customary to use the cubic notation with the square bracket indicating the non-equivalence of the z-direction that arises from the tetragonality of the structure.

At low temperatures the pure  $\gamma$ -phase L1<sub>0</sub> is deformed primarily by  $\langle 101 \rangle$  superdislocations while both kinds of ordinary dislocations are inactive (Inui *et al.* 1997). The ductility of the single  $\gamma$ -phase is thus very low. As the temperature increases both slip by  $1/2\langle 110 \rangle$  ordinary dislocations and twinning become active. This is rather unusual because in most materials twinning is the low temperature deformation mode. At about 800° C the  $1/2\langle 110 \rangle$  ordinary dislocations start to dominate and the superdislocation slip becomes the hardest deformation mode (Yamaguchi *et al.* 1995, Inui *et al.* 1997). The DO<sub>19</sub>  $\alpha_2$ -phase is difficult to deform as all the slip modes have very high yield stresses. The least difficult to operate is the prism slip, then comes the slip on the basal plane and the highest yield stress mode is for the pyramidal plane slip (Inui, Toda and Yamaguchi 1993, Yamaguchi and Inui 1993). The PST crystals deform much more easily when compared to their constituent phases. At room temperature twining is the prevailing mechanism but glide of  $1/2\langle 110 \rangle$  ordinary dislocations in the  $\gamma$ -lamellae is also common. The glide of  $\langle 101 \rangle$  superdislocations is the hardest deformation mode (Inui *et al.* 1992b).

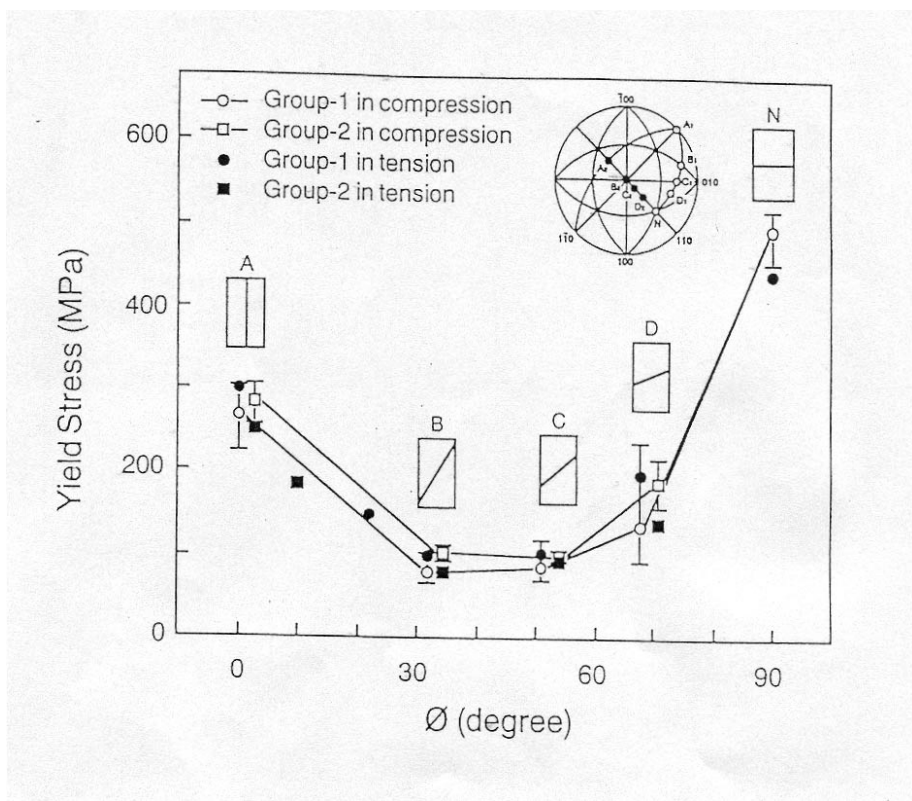


Figure 1.8 Yield stress of the PST crystal as a function of the angle of the loading axis with respect to the plane parallel to the lamellar boundaries.(After Fujiwara *et al.* 1990).

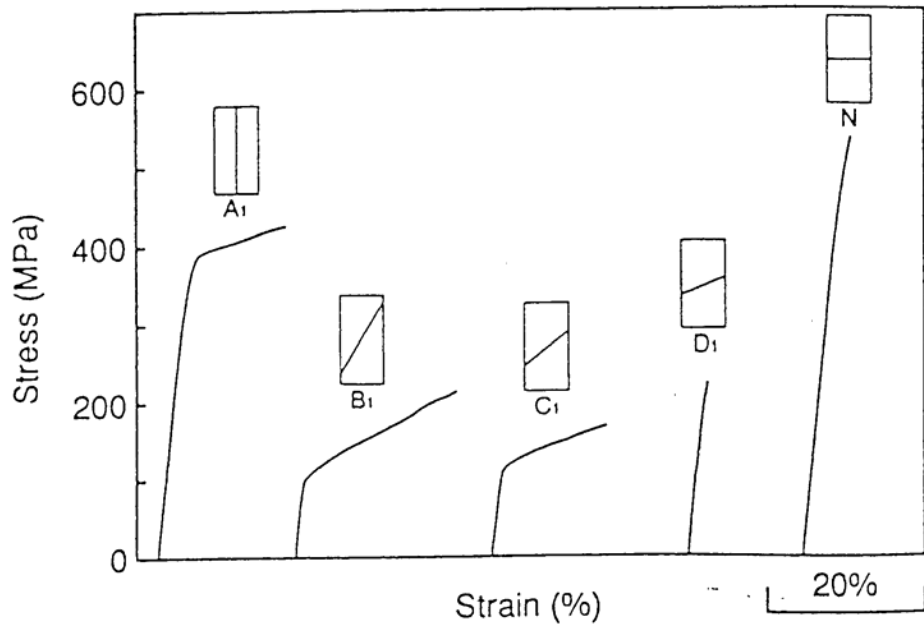


Figure 1.9 Elongation to fracture of the PST crystal as a function of the angle of the loading axis with respect to the plane parallel to the lamellar boundaries.(After Inui *et al.* 1992c).

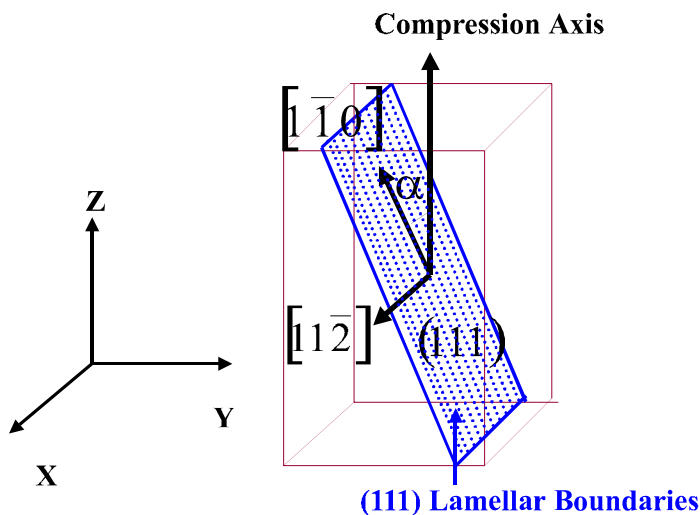


Figure 1.10 PST loading experiment

The deformation of PST crystals shows strong anisotropy arising from their lamellar character. Since the lamellar structure leads to improved ductility the mechanical behavior of the PST crystals has been a target of many experimental studies. Fujiwara *et al.* 1990 and Inui *et al.* 1992c studied the dependence of the yield stress and elongation to fracture on the orientations of the PST crystal. The results for the yield stress and for fracture toughness are shown in Figure 1.8 and Figure 1.9, respectively.  $\Phi$  is the angle between the loading axis and plane parallel to the lamellar boundaries (Figure 1.10). As can be seen from Figure 1.8 the yield stress shows concave dependence on the angle  $\Phi$ . For intermediate angles  $30^\circ < \Phi < 60^\circ$  (orientations B, C and D in Figure 1.8) the deformation occurs in the easily deformable  $\gamma$ -lamellae via shearing along  $\{111\}$ planes, inclined with respect to the loading axis and parallel to the lamellar boundaries. The hard-to-deform  $\alpha_2$ -lamellae practically do not participate in the deformation (Inui *et al.* 1992c). There is, therefore, a relatively early onset of yielding and consequently a low yield stress (see Figure 1.8). After the yielding starts, the sample deforms up to about 20 % elongation and then it fractures. Figure 1.11 shows the shearing of the sample loaded in compression. The negative change in the length of the sample in the direction of the compression,  $\Delta z$ , is compensated by elongation by the same amount  $\Delta y$  in the direction of the slip projected onto the plane normal to the loading axis ( $\Delta y = -\Delta z$ ). There is no extension or contraction in the x-direction that is perpendicular to the direction of shearing.

Figure 1.12 shows the “N” orientation when the loading axis is perpendicular to the lamellar boundaries. In this configuration there is no resolved shear stress and therefore no driving force for the slip on the {111}planes parallel to the lamellar boundaries. The slip must thus cross through the lamellar boundaries. In the  $\gamma$ -lamellae the deformation proceeds via normal slip on a set of inclined {111}planes, while in the  $\alpha_2$ -lamellae the only operational mode for this configuration is the pyramidal slip which as has been already mentioned is the hardest mode in the  $\alpha_2$ -phase. As a result the PST crystals loaded in the ”N” orientation have a very high yield stress and often fracture at elongation of about 20% without actually yielding (see Figure 1.9). Figure 1.12 shows that in this case the sample deforms in all three directions. When compressed along the loading z-axis it extends by the same amounts in the two perpendicular directions ( $\Delta y = \Delta x$ ).

The most interesting is the configuration “A” (Figure 1.13) where the loading axis z is parallel to the lamellar interfaces. In this case there is surprisingly no cross-lamellar slip and the deformation mechanism is a unique combination of  $\langle 110 \rangle \{111\}$ type slip and twinning. The contraction in the z-direction results in the elongation in the x-direction only ( $\Delta x = -\Delta z$ ) while there is no displacement in the direction perpendicular to the lamellar interfaces  $\Delta y = 0$  (Figure 1.13). This can be achieved only by a closely correlated action of twinning and slip that have to mutually cancel their lateral shifts in the y-direction. The yield stress for this configuration is also rather high, but there is still some significant plastic deformation before fracture that occurs at about 10% elongation

(see Figure 1.9). The important difference between this orientation and the “N” orientation is that in the case of “N” orientation there is no twinning mode available which could combine with slip. Thus, for the “N” orientation dislocation transmission is necessary which is the reason behind the high yield stress.

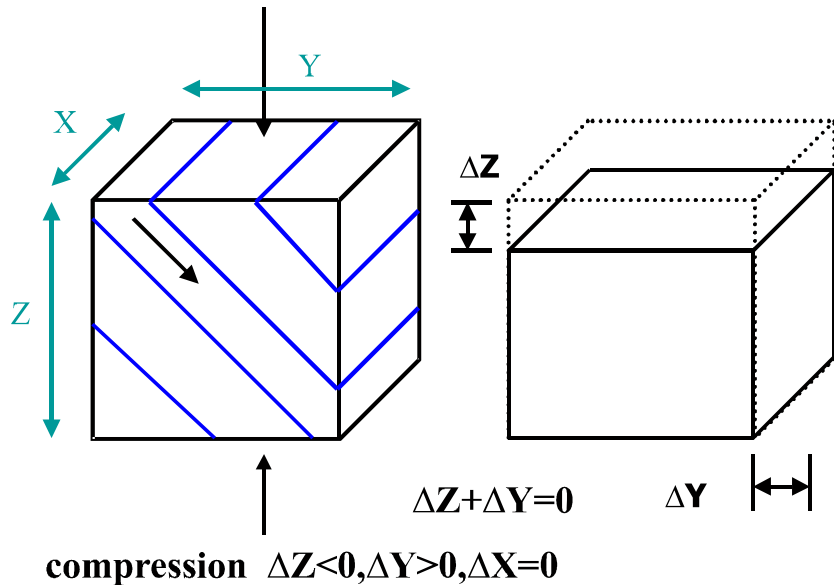


Figure 1.11 “B” orientation

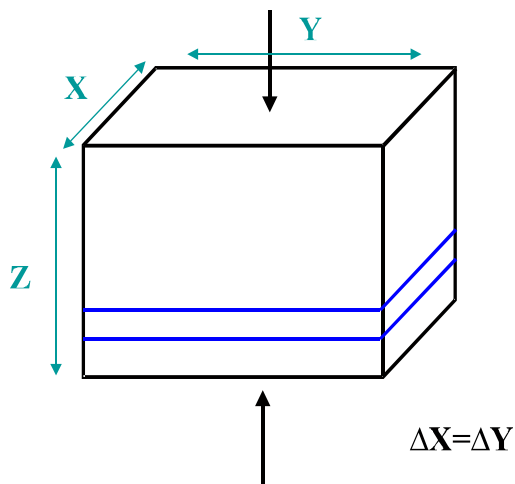


Figure 1.12 “N” orientation

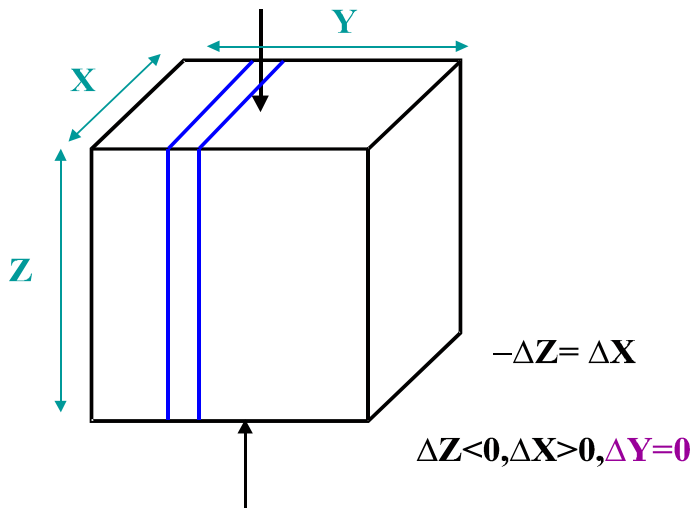


Figure 1.13 “A” orientation

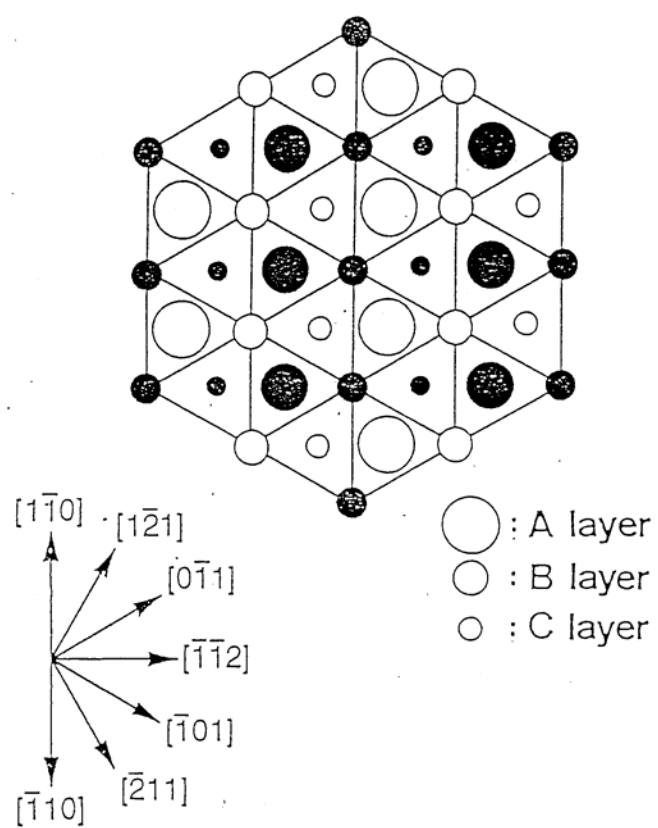


Figure 1.14 The {111} plane in the L1<sub>0</sub> TiAl.

The abundant presence of interfaces in PST crystals, both lamellar boundaries and domain boundaries, influences their fracture behavior. According to Inui *et al.* 1992c, for both the “N” (Figure 1.12) and “B” (Figure 1.11) orientations of the PST crystals fracture occurs in a cleavage-like mode along the lamellar interfaces, while in the case of “A” (Figure 1.13) orientation fracture is observed to occur in a cross-lamellar way. The energy of interfaces is a key factor influencing the propensity for crack nucleation and propagation along an interface. The higher the energy of the interface the more likely it is to be delaminated by fracture. It is therefore essential to study the energetics of different types of interfaces present in the PST crystal. A detailed classification of interfaces in the PST crystal can be found in Inui *et al.* 1992b. As mentioned earlier, due to the near equiatomic composition most of the interfaces are of the  $\gamma/\gamma$  type but some  $\gamma/\alpha_2$  type interfaces are also present. As in the polycrystalline lamellar phase, in PST crystals the lamellar interfaces always lie parallel to the set of close-packed planes, {111} planes in the  $\gamma$ -lamellae and {0001} basal planes in the hexagonal  $\alpha_2$ -lamellae. There are six possibilities for  $\gamma/\gamma$  interface configurations based on the relative orientation of two  $[1\bar{1}0]$  vectors lying in the close packed {111} planes on each side of the lamellar boundary (Inui *et al.* 1992b):

$$(1.1) \quad (a) [1\bar{1}0]\uparrow\uparrow[1\bar{1}0] \quad (b) [1\bar{1}0]\uparrow\uparrow[\bar{1}01] \quad (c) [1\bar{1}0]\uparrow\uparrow[01\bar{1}]$$

(1.2) (a)  $[1\bar{1}0]\uparrow\downarrow[1\bar{1}0]$  (b)  $[1\bar{1}0]\uparrow\downarrow[\bar{1}01]$  (c)  $[1\bar{1}0]\uparrow\downarrow[01\bar{1}]$

The parallel orientations are listed in (1.1) while the anti-parallel ones are summarized in (1.2). The orientation (1.1a) has the two  $[1\bar{1}0]$  vectors aligned and thus corresponds to the ideal crystal. For both (1.1b) and (1.1c) the corresponding  $[1\bar{1}0]$  vectors in the two lamellae are at an angle of  $120^\circ$  and the lamellar interface created this way is referred to as the rotational fault. This interface is shown in Figure 1.15, where the upper part is miss-oriented with respect to the lower part of the crystal by  $120^\circ$ . In an fcc structure such rotation would not create a boundary and the resulting structure would be an ideal crystal. Existence of this interface is due to the non-equivalence of the  $[1\bar{1}0]$  and  $[\bar{1}01]$  directions in the (111) plane of the  $L1_0$  structure (see Figure 1.14) which is caused both by the presence of different atomic species in the  $L1_0$  and the non-ideality of the c/a ratio. The fcc-like ...ABCABCABC... close-packed stacking is preserved across the interface, but as the result of the rotation the layout of atomic species changes. While in the lower part the columns of atoms along the direction perpendicular to the plane of the picture consist of the same atomic species, in the upper part the columns have alternating Ti and Al atoms (Figure 1.15).

The anti-parallel orientation (1.2a) corresponds to ordinary twin boundary (Figure 1.16) which comes about as a result of  $180^\circ$  rotation of the upper part of the crystal with respect to the lower part. In this case the ...ABCABCABC... stacking is not conserved across the boundary. The interface has a mirror symmetry, the upper part is a

mirror image of the lower part as can be seen in Figure 1.16. The remaining two orientations (1.2b) and (1.2c) are equivalent and they correspond to an interface called pseudotwin which can be looked at as a combination of the 120° rotational fault and the twin. The pseudotwin (Figure 1.17) can be formed from the twin by an additional 120° rotation of the upper part. The boundary thus has a twin-like mirror symmetry that connects atomic positions in the lower and upper grain. Due to the additional rotation, however, the corresponding atomic positions may be occupied by different atomic species. As in the case of the rotational fault, the columns of atoms perpendicular to the plane of the picture in the upper lamella shown in Figure 1.17 are occupied alternatively by Ti and Al. In addition to the above classification of interfaces based on the orientation of the lamellae there are other possible boundaries that can be created by shifting the lamellae with respect to each other. Among the possible shifts on the (111) plane, the so-called anti-phase boundary (APB) shift has been experimentally observed in the twin boundaries (Denquin and Naka 1994). Therefore, in the course of this work both coherent and shifted boundaries will be studied. Another point to mention is that due to the non-ideal c/a ratio some of the above mentioned interfaces will have regions of misfit. This happens in the case of the 120° rotational fault and the pseudotwin, where the two non-equivalent directions  $[1\bar{1}0]$  and  $[\bar{1}01]$  overlap. A network of misfit dislocations must compensate for the misfit in these cases. The deviation from non-ideality is very small (about 1.6%) and therefore misfit dislocations will be about 60 lattice spacings apart and there will be large coherent regions in between them (Hazzledine and Kad, 1995).

Similar orientation-based classification exists also for  $\gamma/\alpha_2$  interfaces and can be found in Inui *et al.*, 1992b. As these interfaces are much less frequent than those of the  $\gamma/\gamma$  type they will not be studied in this work.

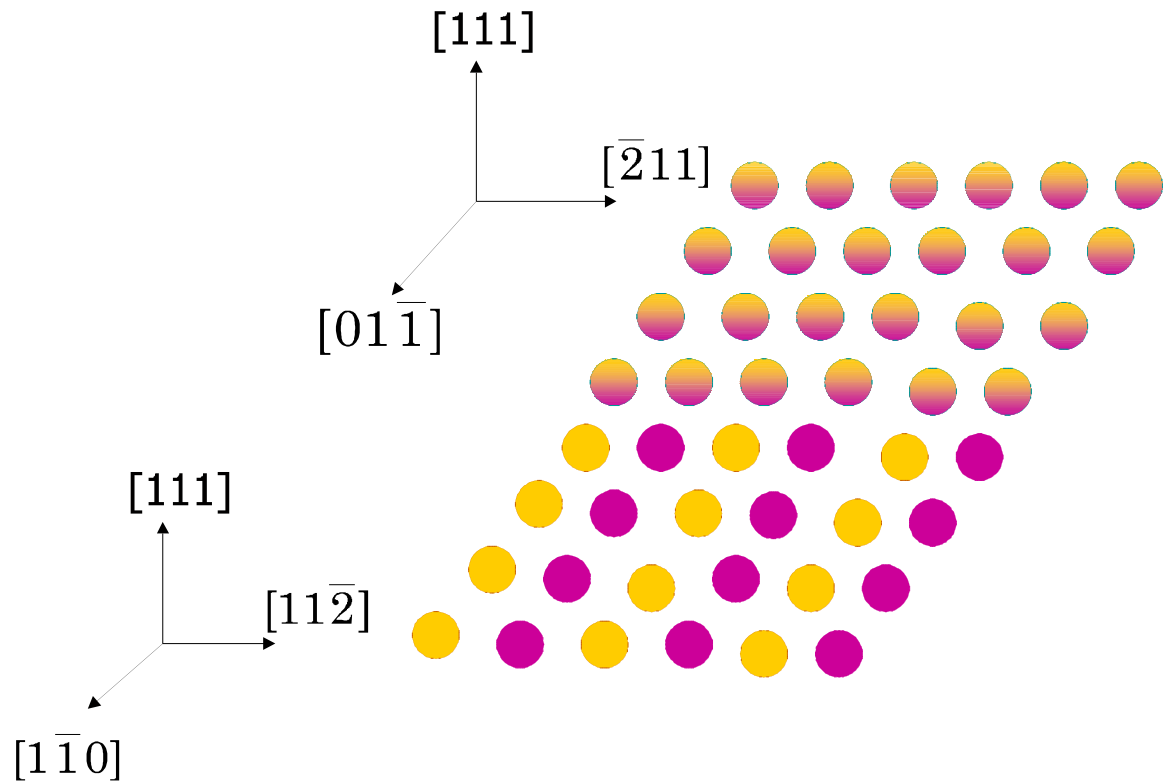


Figure 1.15 120° rotational fault

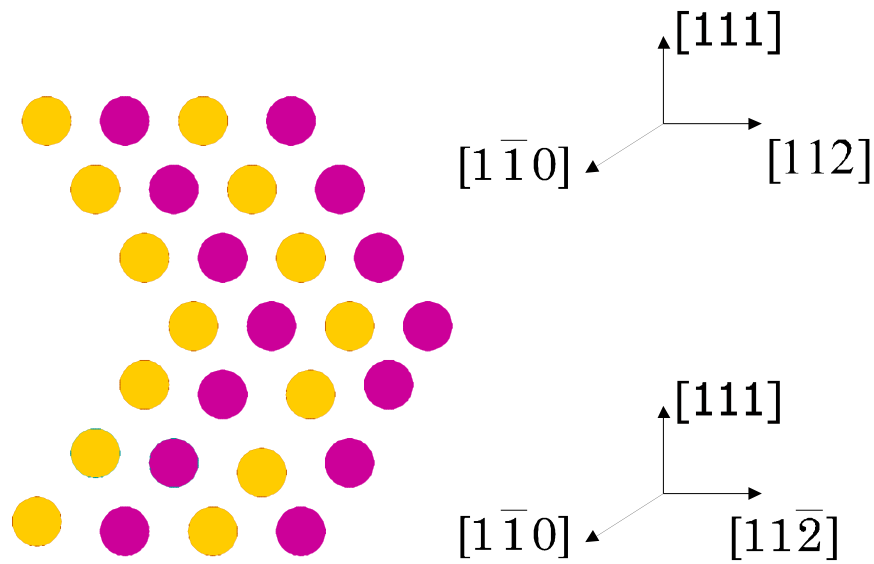


Figure 1.16 Twin

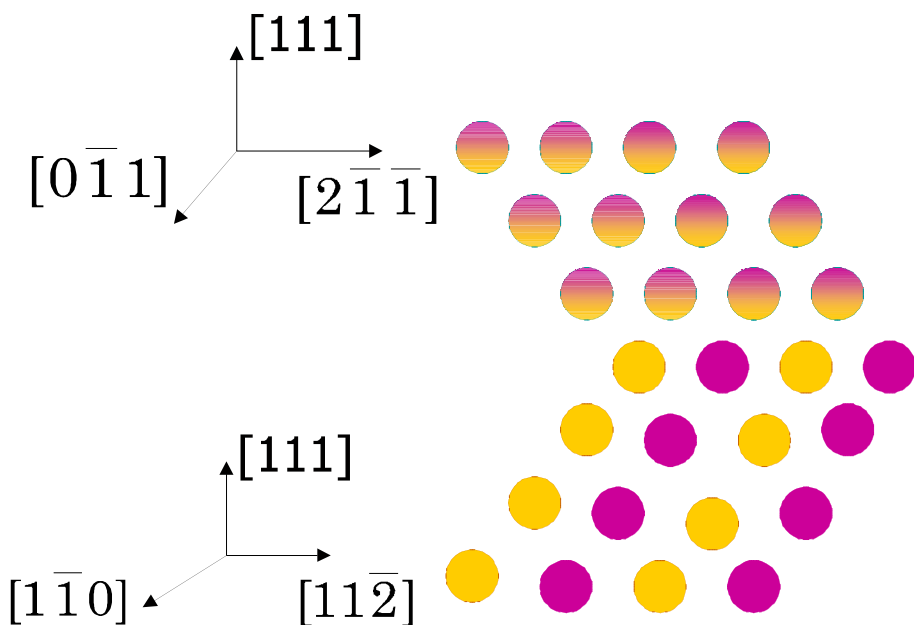


Figure 1.17 Pseudotwin

Similarly as in other materials, the deformation behavior of TiAl alloys, is strongly influenced by possible dissociation of dislocations. Dislocations with longer Burgers vectors may split into partials separated by stacking fault type defects. The energies of these defects play a decisive role in determining the most favorable way of dislocation splitting. There are three possible metastable stacking faults on the (111) plane in the L1<sub>0</sub> structure: the anti-phase boundary (APB), the super-lattice intrinsic stacking fault (SISF) and the complex stacking fault (CSF). They correspond to rigid body shifts by vectors  $1/2[\bar{1}01]$ ,  $1/6[11\bar{2}]$  and  $1/6[\bar{2}11]$  respectively (Figure 1.18). Out of these only the existence of the SISF is guaranteed by symmetry while the other two may but need not be metastable (Girshick, 1997). The stability and energies of these faults will be studied in detail later in his work.

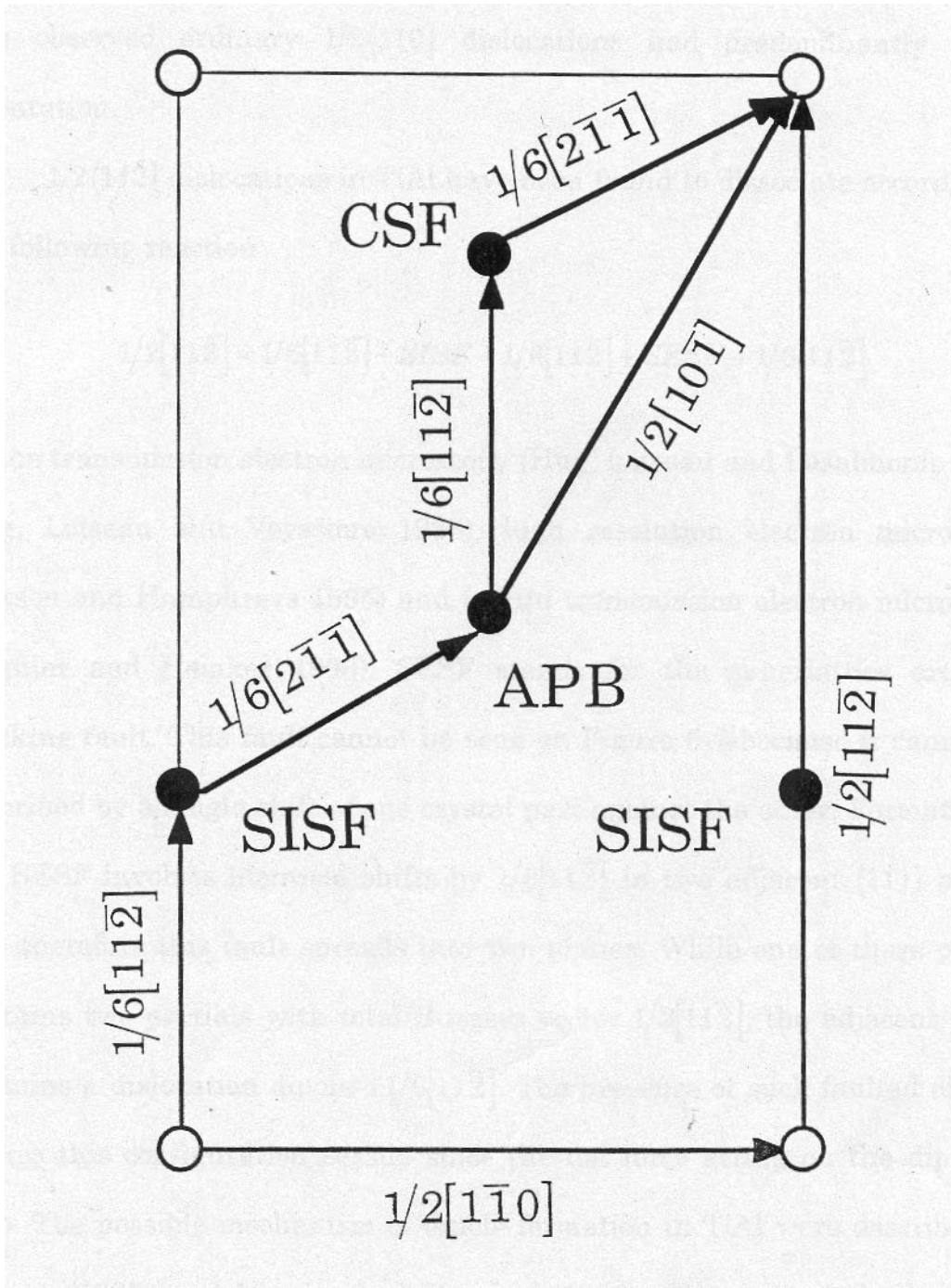


Figure 1.18 Stacking faults on the (111) plane in the  $L1_0$  TiAl

### **3. COMPUTER MODELING OF EXTENDED DEFECTS**

As discussed in Chapter 1, atomistic studies of extended defects, such as dislocations, stacking-fault type defects and interfaces, serve as means for attaining fundamental understanding of mechanical behavior of materials. Apart from using appropriate description of atomic interactions, which is an essential precursor, there are other aspects that need to be considered when performing computer modeling of such defects.

Firstly, it is the way the atomic simulation block is constructed and appropriate boundary conditions applied. Secondly, it is the simulation technique used in the process of relaxation of the constructed block.

There are numerous relaxation techniques – molecular dynamics, molecular statics and Monte Carlo being among the most common – that correspond to different ways of minimizing the energy and/or free energy of the system with the ultimate goal of finding the global minimum. The parameters, with respect to which the energy is minimized, are usually atomic coordinates, but other variables pertinent to the given study may be included. In all our calculations we employed the molecular statics technique - a direct and simple minimization method that does not include any temperature effects. In the relaxation process, the coordinates of the atoms in the simulation block are being varied according to a chosen minimization algorithm until a minimum energy configuration is attained. Unlike in the case of the molecular dynamics, the intermediate configurations of the system do not have any physical meaning. Within the molecular statics technique,

different minimization algorithms may be suitable for different cases studied. For systems with a large number of atoms we employed the steepest descent method which is the most straightforward minimization algorithm. At any given simulation step the atoms are shifted in the direction of forces exerted on them. The magnitude of this shift is related to the magnitude of the force via a proportionality coefficient that is being adjusted during the flow of the simulation. The main shortcoming of this method is that it usually finds the local minimum closest to the starting configuration that need not be the lowest one. When relaxing smaller systems we used more sophisticated minimization algorithms - the conjugate gradient and the variable metrics methods which have a higher probability of finding the global minimum than the steepest descent. In addition to the first derivatives of the energy (i.e. forces) these methods take into account forces calculated at previous iterations (conjugate gradient) or make use of higher (second) order derivatives of the energy (variable metrics) when determining the shift of the atomic positions at a given iteration step. For large number of atoms, these methods may, however, exhibit oscillations and/or instabilities in the convergence.

While using steepest descent, or any other relaxation technique, does not assure that the absolute energy minimum is found, this method is very well suited for investigating metastable configurations. These are of eminent interest for our studies of extended defects. Care must, however, be taken when considering, for example, metastable dislocation cores since different starting configuration may result in finding different local minima. It is therefore essential that the initial conditions be varied to reveal the existence of all achievable different metastable configurations.

The following two sections describe the construction of simulation blocks for modeling of stacking fault-type defects and dislocation cores, respectively, and provide some details of the applied relaxation schemes.

### **1.1. Modeling of the $\gamma$ -surfaces and Stacking Fault-Type Defects**

The concept of the  $\gamma$ -surface was introduced by Vitek (1968) when searching for the possible metastable stacking faults in bcc metals. It can be defined in the following way. The crystal is cut into two parts along a certain crystal plane, and the upper part is displaced with respect to the lower part by a vector  $\vec{f}$ , lying in the plane of the cut. The energy of the faults created in this way, plotted as a function of the displacement  $\vec{f}$ , forms the  $\gamma$ -surface. Due to the 2-dimensional periodicity of crystal plane along which the cut has been made, it is necessary to evaluate the energy only for the displacement within one period. Local minima on this surface determine possible metastable stacking faults on the crystal plane considered. The positions and energies of these faults are important for the analysis of possible dislocation dissociation schemes.

While all the possible metastable stacking faults on a given crystal plane can only be found if the corresponding  $\gamma$ -surface is calculated, existence of certain faults is dictated by crystal symmetry. The  $\gamma$ -surface always possesses extrema for displacements for which there are at least two non-parallel mirror planes in the ideal lattice: the first derivative of the  $\gamma$ -surface is then zero in two different directions (Yamaguchi, Vitek, Pope and Umakoshi 1981; Vitek 1992). Whether these extrema correspond to minima, and thus metastable stacking faults, can often be deduced by considering the first nearest

neighbor interactions. Such stacking faults are then common to all materials with a given crystal structure. However, for a particular material other minima than those dictated by symmetry may exist, and their existence depends on the details of atomic interactions.

In our calculations of  $\gamma$ -surfaces we always impose periodic boundary conditions in the two directions that lie in the plane of the cut, while in the direction perpendicular to the plane of the cut the block extends far away and is terminated by a free surface. Thus the calculations are effectively the same as when studying bicrystals. In the course of the simulation, the upper half of the block is displaced by the vector  $\vec{f}$  with respect to the lower part to create the generalized stacking fault with the corresponding displacement at the fault plane (Figure 3.1). For each displacement  $\vec{f}$ , the separation between the two parts of the block is varied to minimize the energy. The two parts are allowed to move only as rigid blocks (i.e. no relaxation of individual atoms is allowed) and only in the direction perpendicular to the plane of the cut.

A different approach is adopted when modeling a metastable interface or a metastable stacking fault-type defect, such as the SISF. In addition to the relaxation of the separation of the two parts of the block, we also include in this case relaxation of individual atomic positions. The block is always divided into two sub-blocks. The positions of atoms in the inner sub-block, which includes the plane of the cut, are adjusted so as to attain minimum of the energy. The atoms in the outer sub-block are kept fixed in the positions of the corresponding perfect lattice. Significant deviations of the atomic positions from those in the perfect lattice do not extend away from the fault plane beyond the distance comparable with the size of the period in this plane. Since this

period is usually short, generalized stacking faults are not associated with long-range elastic fields.

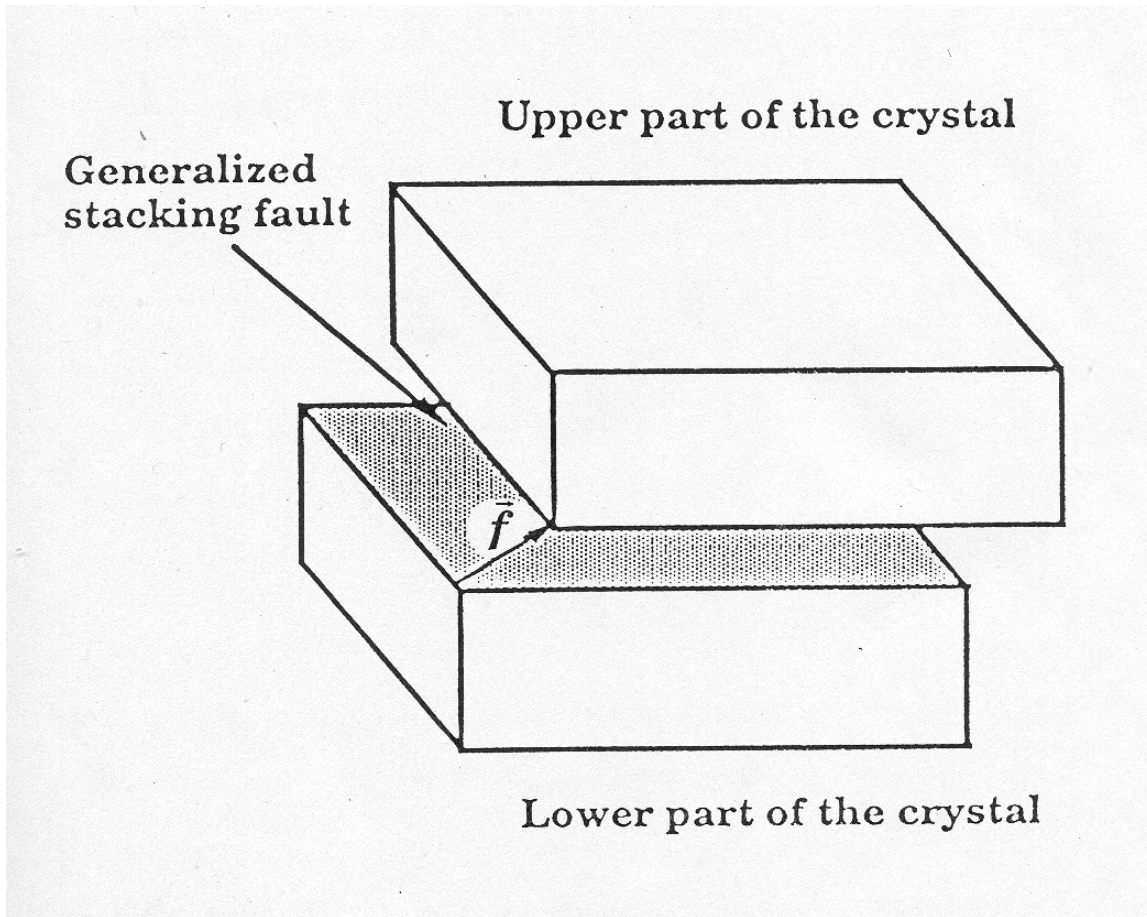


Figure 3.1 Schematic picture of the atomic block used in the  $\gamma$ -surface calculations.

## 1.2. Modeling of the Dislocation Core Structure

The situation becomes more complicated when modeling dislocations. The reason is the presence of long-range elastic field these defects are accompanied by. Existence of

such field implies that even far away from the dislocation core the atomic positions deviate significantly from those in the ideal lattice. Fortunately, this long-range strain field can be accurately represented by the elastic field that can be evaluated analytically from the continuum theory of dislocations even in the anisotropic case. The analytic expressions for the elastic field of straight infinite dislocations can be found in Hirth and Lothe, 1982.

In our calculations the block used in dislocation modeling has a one-dimensional periodicity in the direction parallel to the dislocation line. The simulation block is again divided into two parts (see Figure 3.2) - the inner region where the atomic positions are being relaxed (the so called active atoms) - and the outer region in which the atoms are kept at fixed positions (the so called inert atoms). Atoms in both regions are initially displaced according to the corresponding elastic field determined by the elastic theory of dislocations (Hirth and Lothe, 1982). During the relaxation the atoms in the outer region retain this displacement while the atomic positions in the inner region are relaxed until a minimum energy configuration is found. For achieving full compatibility, especially around the border regions of the inner and outer parts of the simulation block, it is essential that correct elastic constants are used in the evaluation of the analytical elastic field. When applying the continuum elasticity theory it is therefore important to use elastic constants predicted by scheme employed to describe atomic interactions in the relaxation calculations and not experimental (or other) values.

Other factors may also influence the actual outcome of the calculation. The size of the relaxed region is critical for the determination of the correct core structures, especially in

the case of broadly dissociated dislocations. As discussed earlier, the molecular statics technique does not guarantee that the absolute minimum of the energy is found. Several initial positions of the center of the elastic field of the dislocation in the atomic block should therefore be tried since different starting configurations may lead to different metastable core configurations.

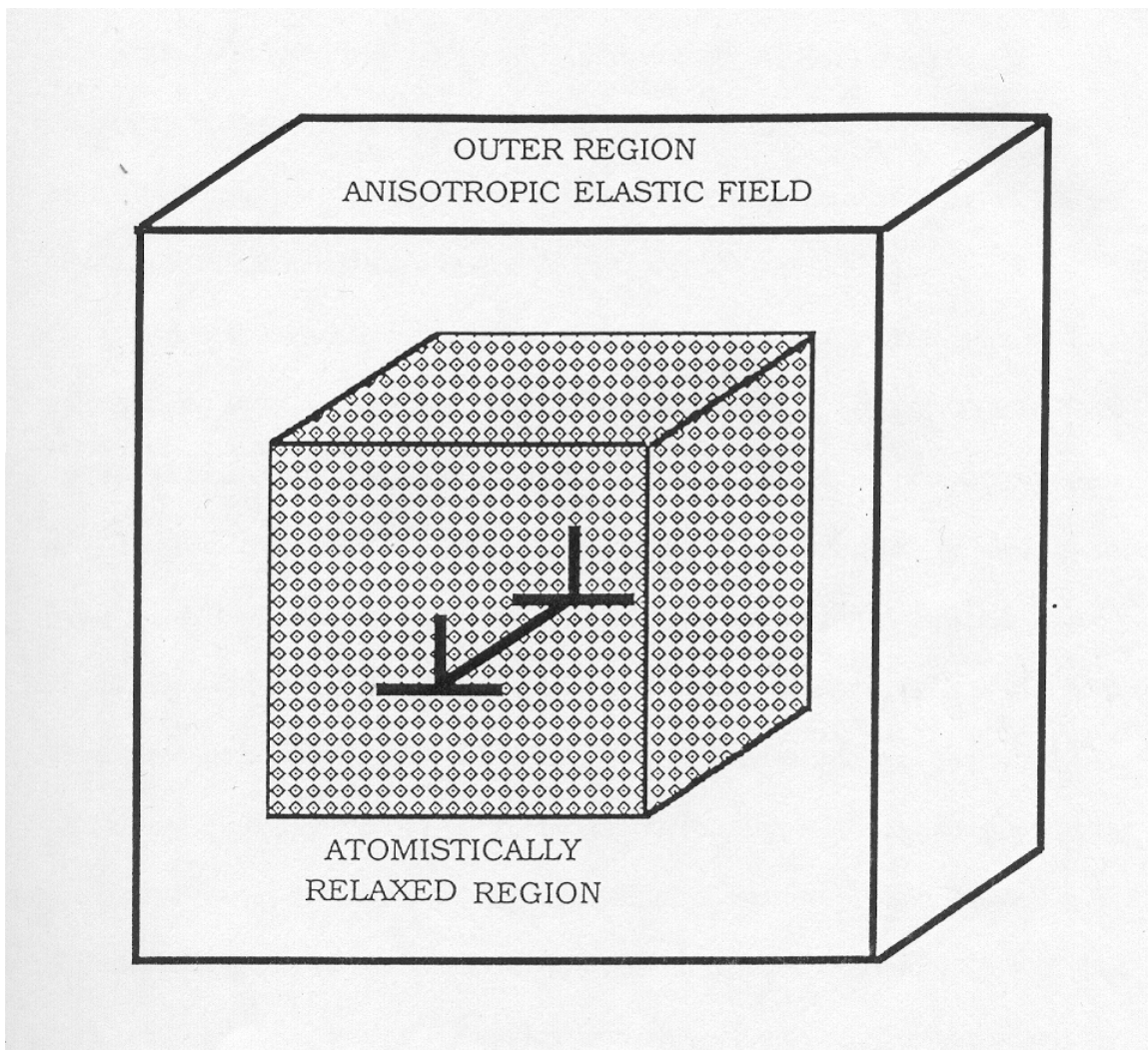


Figure 3.2 Schematic picture of the atomic block used in the dislocation calculations.

## 4 BOND ORDER POTENTIALS

This chapter gives an overview of the theory underlying the development of the Bond Order Potentials. For the actual implementation of this method the suit of computer codes available as Order N (OXON) package was used.

### 4.1 The Tight-Binding Method

The tight-binding method is an approximate approach for solving the quantum mechanical problems that correctly accounts for the nature of bonding, in particular when covalent bonding is significant. Although originally developed as a semi-empirical method it can now be rationalized on the basis of the density functional theory (Hohenberg and Kohn 1964, Kohn and Sham 1965). According to the density functional theory (DFT) the ground state energy  $E_{GS}$  of an interacting inhomogeneous electron gas in an external field  $v(r)$  can be expressed as a unique functional of the electronic density  $n(r)$

$$(4.1) \quad E_{GS} = E_{GS}[n(r)]$$

The energy functional is given as

$$(4.2) \quad E_{GS}[n(r)] = T[n(r)] + \int dr v(r)n(r) + \frac{1}{2} \iint dr dr' \frac{n(r)n(r')}{|r-r'|} + E_{xc}[n(r)]$$

where  $T[n(r)]$  and  $E_{xc}[n(r)]$  are the kinetic energy and the exchange-correlation energy of the interacting electron gas, respectively. The forms of these functionals are not known

a priori. Assuming a slowly varying density  $n(r)$  the so-called local density approximation (LDA) can be adopted for the exchange-correlation functional. In this approximation this functional takes up the following form

$$(4.3) \quad E_{xc}[n(r)] = \int dr n(r) \epsilon_{xc}[n(r)]$$

where  $\epsilon_{xc}[n(r)]$  is the exchange-correlation energy per electron of a uniform electron gas of density  $n$ .

The density  $n(r)$  can be found by functional minimization of the energy functional by requiring

$$(4.4) \quad \delta E_{GS}[n(r)] = 0$$

What is still unknown, however, is the kinetic energy functional. In order to obtain the kinetic energy functional an ingenious trick is used. A fictitious system of non-interacting electrons is considered that moves in an effective external potential  $v_{eff}(r)$  and has the same density  $n(r)$ , and therefore also the same kinetic energy  $T[n(r)]$ , as the interacting system. The ground state energy of the fictitious non-interacting system can be written as

$$(4.5) \quad E_{GS}^{fict.}[n(r)] = T[n(r)] + \int dr v_{eff}(r) n(r)$$

with the effective potential given by

$$(4.6) \quad v_{eff}(r) = v(r) + \int dr \frac{n(r)n(r')}{|r-r'|} + \mu_{xc}[n(r)]$$

where  $\mu_{xc}[n(r)]$  is defined as

$$(4.7) \quad \mu_{xc}[n(r)] = \frac{\delta E_{xc}[n(r)]}{\delta n(r)}$$

The kinetic energy expressed in terms of the energy of the non-interacting system then becomes

$$(4.8) \quad T[n(r)] = E_{GS}^{fict.}[n(r)] - \int dr v_{eff}(r)n(r)$$

Inserting (4.8) into (4.2) we obtain

$$(4.9) \quad E_{GS}[n(r)] = E_{GS}^{fict.}[n(r)] - \frac{1}{2} \iint dr dr' \frac{n(r)n(r')}{|r-r'|} - \int dr n(r)\mu_{xc}(r) + E_{xc}[n(r)]$$

In this way the problem is reformulated into an equivalent problem of finding the ground state energy of the fictitious system. Functional minimization of the ground state energy  $E_{GS}^{fict.}[n(r)]$  of the fictitious system (see equation (4.5)) with respect to the density  $n(r)$  is equivalent to solving an effective one-electron Schrodinger-like equation known as the Kohn-Sham equation

$$(4.10) \quad \left[ -\frac{\hbar^2}{2m} \nabla^2 + v_{eff}(r) \right] \varphi^{(n)}(r) = \epsilon^{(n)} \varphi^{(n)}(r)$$

where  $\varphi^{(n)}(r)$  are one-electron eigenfunctions used in the expression for the electron density

$$(4.11) \quad n(r) = \sum_{n(occ.)} |\varphi^{(n)}(r)|^2$$

and  $\epsilon^{(n)}$  are the corresponding eigenvalues. Unlike in the case of the Schrodinger

equation, in the Kohn-Sham equation the potential  $v_{eff}(r)$  depends on the density  $n(r)$ .

This equation must therefore be solved self-consistently in an iterative loop. After full self-consistency is achieved, the energy and other properties of the real system can be evaluated. The energy  $E_{GS}[n(r)]$  expressed in terms of the band energy

$E_{band}^{fict.} = 2 \sum_{n(occ)} \epsilon^{(n)}$  of the fictitious system becomes

$$(4.12) \quad E_{GS}[n(r)] = 2 \sum_{n(occ)} \epsilon^{(n)} - \frac{1}{2} \iint dr dr' \frac{n(r)n(r')}{|r-r'|} - \int dr n(r) \mu_{xc}(r) + E_{xc}[n(r)]$$

The solution of the Kohn-Sham equation provides a framework for the broad class of different ab-initio techniques. The achievement of self-consistency is the most complex and time consuming part of any ab-initio calculation.

Another level of approximation – the Harris-Foulkes functional (Harris 1985, Foulkes and Haydock 1989) drops the requirement of self-consistency and evaluates the energy based on the output density obtained after one iteration. The input density is usually taken as the superposition of atomic charge densities.

From the Harris-Foulkes approximation to the density functional theory the tight-binding model can be derived. To determine the total energy of the system of atoms  $E_{tot}$  we add the ion-ion interaction to the energy given by equation (4.12)

$$(4.13) \quad E_{tot} = 2 \sum_{n(occ)} \epsilon^{(n)} - \frac{1}{2} \iint dr dr' \frac{n(r)n(r')}{|r-r'|} - \int dr n(r) \mu_{xc}(r) + E_{xc}[n(r)] + E_{ion-ion}$$

The first term is the electronic band energy and the second term is the so-called double counting term. The band energy is the sum of the eigenvalues of the effective single-

particle Schrodinger equation (4.10) that we now rewrite using the bra-ket notation as

$$(4.14) \quad \hat{H}|n\rangle = \varepsilon^{(n)}|n\rangle$$

where  $\hat{H}$ ,  $|n\rangle$  and  $\varepsilon^{(n)}$  are the Hamiltonian operator, the single-particle eigenfunctions and the eigenvalues respectively. In order to find the solution of (4.14) the single particle eigenfunctions  $|n\rangle$  are usually expanded into a set of chosen atomic-like orbitals

$$(4.15) \quad |n\rangle = \sum_{i\alpha} C_{i\alpha}^{(n)} |i\alpha\rangle$$

where  $i$  is a site index,  $\alpha$  is the orbital index and  $C_{i\alpha}^{(n)} \equiv \langle i\alpha | n \rangle$ . Both the eigenfunctions  $|n\rangle$  and the atomic-like orbitals  $|i\alpha\rangle$  are assumed to form orthonormal and complete sets so that

$$(4.16) \quad \langle n | m \rangle = \delta_{n,m}, \quad \langle i\alpha | j\beta \rangle = \delta_{i\alpha,j\beta}$$

$$(4.17) \quad \mathbf{1} = \sum_n |n\rangle \langle n| = \sum_{i\alpha} |i\alpha\rangle \langle i\alpha|$$

(In practice only a finite set of orbitals is used and thus the condition of completeness is never really satisfied). The Hamiltonian can be expressed as the kinetic energy plus a superposition of potentials centered on different atoms ( $\mathbf{R}_i$  is the position vector of atom  $i$ )

$$(4.18) \quad \hat{H}' = -\frac{\hbar^2}{2m} \nabla^2 + \sum_i v_i(\mathbf{r} - \mathbf{R}_i)$$

After inserting (4.15) into (4.14) and making use of the orthonormality relation (4.16) we get the following matrix equation

$$(4.19) \quad \sum_{j\beta} \langle j\beta | \hat{H} | i\alpha \rangle C_{j\beta}^{(n)} = \epsilon_{i\alpha}^{(n)} C_{i\alpha}^{(n)}$$

After solving (4.19) for the eigenvectors  $C_{i\alpha}^{(n)}$  we get the expression for the band energy by multiplying equation (4.19) by  $C_{i\alpha}^{(n)}$ , summing over  $i$  and  $\alpha$  and using the

normalization relation  $\sum_{i\alpha} |C_{i\alpha}^{(n)}|^2 = 1$

$$(4.20) \quad E_{band} = 2 \sum_{n(occ)} \epsilon_{i\alpha}^{(n)} = 2 \sum_{n(occ)} \sum_{i\alpha, j\beta} C_{i\alpha}^{(n)} H_{i\alpha, j\beta} C_{j\beta}^{(n)}$$

where we have denoted the matrix elements  $H_{j\beta, i\alpha} = H_{i\alpha, j\beta} = \langle j\beta | \hat{H} | i\alpha \rangle$ . If the diagonal elements of the Hamiltonian matrix (also referred to as on-site energies),  $\epsilon_{i\alpha} = H_{i\alpha, i\alpha}$ , are separated in (4.20), the band energy can be partitioned as

$$(4.21) \quad E_{band} = 2 \sum_{n(occ)} \sum_{i\alpha \neq j\beta} C_{i\alpha}^{(n)} H_{i\alpha, j\beta} C_{j\beta}^{(n)} + 2 \sum_{n(occ)} \sum_{i\alpha} C_{i\alpha}^{(n)} C_{i\alpha}^{(n)} \epsilon_{i\alpha} = E_{bond} + E_{onsite}$$

where the first term, which excludes the diagonal elements of the Hamiltonian, is referred to as the bond energy (note the difference between the band and bond energies), while the second term is the onsite energy. Introducing the density matrix  $\rho_{i\alpha, j\beta}$  defined as

$$(4.22) \quad \rho_{i\alpha, j\beta} = \sum_{n(occ)} \langle i\alpha | n \rangle \langle n | j\beta \rangle = \sum_{n(occ)} C_{i\alpha}^{(n)} C_{j\beta}^{(n)}$$

we can write the band energy as

$$(4.23) \quad E_{band} = 2 \sum_{i\alpha \neq j\beta} \rho_{j\beta, i\alpha} H_{i\alpha, j\beta} + 2 \sum_{i\alpha} \rho_{i\alpha, i\alpha} \epsilon_{i\alpha}$$

Inserting (4.21) into equation for the total energy,

(4.13), we get

$$(4.24) \quad E_{tot} = E_{bond} + E_{onsite} - \frac{1}{2} \iint dr dr' \frac{n(r)n(r')}{|r-r'|} - \int dr n(r) \mu_{xc}(r) + E_{xc}[n(r)] + E_{ion-ion}$$

To obtain the cohesive energy we have to subtract the energy of free atoms  $\sum_{i\alpha} N_{i\alpha}^{atom} \epsilon_{i\alpha}^{atom}$  from the total energy; here  $N_{i\alpha}^{atom}$  is the occupancy of the orbital  $\alpha$  on the free atom  $i$  and  $\epsilon_{i\alpha}^{atom}$  is the corresponding energy. This yields

(4.25)

$$E_{coh} = E_{bond} + E_{onsite} - \frac{1}{2} \iint dr dr' \frac{n(r)n(r')}{|r-r'|} - \int dr n(r) \mu_{xc}(r) + E_{xc}[n(r)] + E_{ion-ion} - E_{atoms}$$

The onsite energy and the energy of the free atoms can be grouped together giving

$$(4.26) \quad E_{coh} = E_{bond} + \sum_{i\alpha} (2\rho_{i\alpha,i\alpha} \epsilon_{i\alpha} - N_{i\alpha}^{atom} \epsilon_{i\alpha}^{atom}) - \frac{1}{2} \iint dr dr' \frac{n(r)n(r')}{|r-r'|} - \int dr n(r) \mu_{xc}(r) + E_{xc}[n(r)] + E_{ion-ion}$$

Following Sutton *et al.* 1988, the last four terms can be approximated, to the first order, by a pair-potential provided the input electronic density  $n(r)$  is taken as a superposition of densities of free atoms, as in the Harris-Foulkes approximation. The equation for the cohesive energy then reduces to

$$(4.27) \quad E_{coh} = E_{bond} + \sum_{i\alpha} (2\rho_{i\alpha,i\alpha}\epsilon_{i\alpha} - N_{i\alpha}^{atom}\epsilon_{i\alpha}^{atom}) + \frac{1}{2} \sum_{i\neq j} \phi(r_{ij})$$

The term  $\frac{1}{2} \sum_{i\neq j} \phi(r_{ij})$  is a pair-potential that replaces the double-counting term, the ion-ion interaction and the terms associated with the exchange-correlation energies. To go one step further we rearrange (4.27) by adding and subtracting  $\sum_{i\alpha} N_{i\alpha}^{atom}\epsilon_{i\alpha}$  and obtain

$$(4.28) \quad E_{coh} = 2 \sum_{i\alpha \neq j\beta} \rho_{j\beta,i\alpha} H_{i\alpha,j\beta} + \sum_{i\alpha} [2\rho_{i\alpha,i\alpha} - N_{i\alpha}^{atom}] \epsilon_{i\alpha} + \sum_{i\alpha} N_{i\alpha}^{atom} (\epsilon_{i\alpha} - \epsilon_{i\alpha}^{atom}) + \frac{1}{2} \sum_{i\neq j} \phi(r_{ij})$$

The term  $\sum_{i\alpha} N_{i\alpha}^{atom} (\epsilon_{i\alpha} - \epsilon_{i\alpha}^{atom})$  represents the shift of the onsite energy upon forming the solid from free atoms. Following Sutton *et al.* 1988, this term can also be approximated by pair interaction and included in the pair-potential part of the cohesive energy. The formula for the cohesive energy thus simplifies to

$$(4.29) \quad E_{coh} = 2 \sum_{i\alpha \neq j\beta} \rho_{j\beta,i\alpha} H_{i\alpha,j\beta} + \sum_{i\alpha} [2\rho_{i\alpha,i\alpha} - N_{i\alpha}^{atom}] \epsilon_{i\alpha} + \frac{1}{2} \sum_{i\neq j} \phi(r_{ij})$$

The first term, the bond energy, consists of off-diagonal contributions only and describes the bonding in the solid. The second term, called the promotion energy, is associated with the change of occupancy of the atomic orbitals when atoms are brought together to form a solid. The pair potential accounts for the ion-ion interactions, short-range repulsion arising from Pauli principle and electron correlation effects.

In order to establish a better physical insight into the bond energy term we introduce the concepts of the total and local densities of states. The total density is defined as

$$(4.30) \quad n_{tot}(E) = \sum_n \delta(E - \varepsilon^{(n)})$$

It can be decomposed in the following way

$$\begin{aligned}
(4.31) \quad n_{tot}(E) &= \sum_n \langle n | \delta(E - \hat{H}) | n \rangle \\
&= \sum_{n,m,i\alpha} \langle n | i\alpha \rangle \langle i\alpha | m \rangle \langle m | \delta(E - \hat{H}) | n \rangle \\
&= \sum_{i\alpha} \left| \sum_n \langle n | i\alpha \rangle \right|^2 \delta(E - \hat{H}) \\
&= \sum_{i\alpha} \langle i\alpha | \delta(E - \hat{H}) | i\alpha \rangle \\
&= \sum_{i\alpha} n_{i\alpha}(E)
\end{aligned}$$

where we made use of equation (4.17) describing the completeness of orbital sets.

$n_{i\alpha}(E) = |C_{i\alpha}^{(n)}|^2 \delta(E - \varepsilon^{(n)})$  is defined as the local density state; it is just a projection of the total electron density onto the atomic orbital  $|i\alpha\rangle$ . The diagonal elements of the density matrix present in (4.29) can be written as

$$(4.32) \quad \rho_{i\alpha,i\alpha} = \frac{1}{2} \int_0^{E_F} n_{i\alpha}(E) dE$$

and thus relate to the total number of electrons associated with the orbital  $|i\alpha\rangle$  (the factor 1/2 is due to the spin degeneracy). The off-diagonal elements of the density matrix  $\rho_{i\alpha,j\beta}$  ( $i\alpha \neq j\beta$ ) can be associated with the difference between the number of electrons in the bonding state

$$(4.33) \quad |+\rangle = \frac{1}{\sqrt{2}}(|i\alpha\rangle + |j\beta\rangle)$$

and anti-bonding state

$$(4.34) \quad |-\rangle = \frac{1}{\sqrt{2}}(|i\alpha\rangle - |j\beta\rangle)$$

because using the density operator  $\rho$  we can write

$$(4.35) \quad \rho_{i\alpha,j\beta} = \langle i\alpha | \rho | j\beta \rangle = \frac{1}{2} [\langle + | \rho | + \rangle - \langle - | \rho | - \rangle] = \frac{1}{4} (N_+ - N_-)$$

where  $N_{\pm} = 2 \langle \pm | \rho | \pm \rangle$  is the number of electrons in the bonding/anti-bonding state.

One half of the difference between the number of electrons in the bonding and anti-bonding states is commonly referred to as the bond-order  $\Theta_{i\alpha,j\beta}$  which is defined as

$$(4.36) \quad \Theta_{i\alpha,j\beta} = 2\rho_{i\alpha,j\beta} = \frac{1}{2} (N_+ - N_-) \quad (i\alpha \neq j\beta)$$

Using the bond-order, the cohesive energy, given by (4.29) may be written as

$$(4.37) \quad E_{coh} = \sum_{i\alpha \neq j\beta} \Theta_{j\beta,i\alpha} H_{i\alpha,j\beta} + \sum_{i\alpha} [2\rho_{i\alpha,i\alpha} - N_{i\alpha}^{atom}] \epsilon_{i\alpha} + \frac{1}{2} \sum_{i \neq j} \phi(r_{ij})$$

The two-center orthogonal tight-binding model usually involves several approximations (Sutton *et al.* 1988, Pettifor 1977). The non-orthogonality of the atomic-like orbital basis-set is neglected because the leading correction terms are second order in the overlap matrix. For the same reason the three-center terms and Hamiltonian matrix elements between different orbitals centered on the same atom are neglected. Having introduced these approximations into (4.29), the bond part now has only two-center

matrix elements  $H_{i\alpha,j\beta}(\mathbf{R}_j)$ , while the diagonal promotion term matrix elements,  $\varepsilon_{i\alpha}$ ,

include the so-called crystal field terms  $H_{i\alpha,i\alpha}(\mathbf{R}_j)$

$$(4.38) \quad \varepsilon_{i\alpha} = \langle i\alpha | \hat{H} | i\alpha \rangle = \left\langle i\alpha \left| -\frac{\hbar^2}{2m} \nabla^2 + v_i(r - \mathbf{R}_i) \right| i\alpha \right\rangle + \sum_{j \neq i} H_{i\alpha,i\alpha}(\mathbf{R}_j)$$

where  $H_{i\alpha,i\alpha}(\mathbf{R}_j) = \langle i\alpha | v_j(r - \mathbf{R}_j) | i\alpha \rangle$  (note that omitting terms  $H_{i\alpha,i\beta}(\mathbf{R}_j)$  for  $\alpha \neq \beta$

results in neglecting the effects of crystal field splitting). To calculate the bond energy we need to know all these quantities.

First, for each atomic pair we need to determine the two-center matrix elements  $H_{i\alpha,j\beta}(\mathbf{R})$ , also known as hopping integrals or bond integrals. If the coordinates are transformed so that the z-axis lies along the line connecting the two atoms, the number of bond integrals can be reduced to a small set of fundamental elements, the so-called Slater-Koster bond integrals, multiplied by angular terms related solely to the symmetry of the corresponding orbitals. These angular functions had been tabulated for  $s, p, d$  and  $f$  type orbitals by Slater and Koster, 1954. For example for two atoms, each with  $p$ -orbitals, the 3x3 matrix is fully determined using only two fundamental integrals,  $pp\sigma$  and  $pp\pi$ , multiplied by angular factors. In the case of two atoms with  $d$ -orbitals (5x5 matrix) there are three such basic integrals,  $dd\sigma, dd\pi$  and  $dd\delta$ . In this representation the bond integrals possess a cylindrical symmetry along the axis joining the atomic pair. The actual tight-binding Hamiltonian, however, usually has a lower symmetry since the environment around the bond is not cylindrically symmetric. This leads to the environmental dependence of the bond integrals that will be discussed in more detail in

## Chapter 5.

Since the angular dependence of the hopping integrals is known and tabulated, it is only the radial part of the hopping integrals, also called the scaling function, that needs to be determined. One possible way of ascertaining the scaling function is based on the canonical band theory (Andersen,1975). However, in this work we instead used for this purpose results of ab-initio calculations, as will be described in detail later.

An important condition imposed in many tight-binding calculations, and employed in the present development, is the requirement of the local charge neutrality (LCN). This is an ersatz for the self-consistency of the effective potential,  $v_{eff}(r)$ , in Kohn-Sham equation (4.10). This condition requires that each atom remains charge neutral, i. e. the total charge associated with orbitals centered at a given atom is fixed. In metallic materials this is justified by the fact that any possible excess charge associated with an atom is immediately neutralized owing to the screening by the electron gas (Pettifor, 1995). Quantitatively the LCN condition can be formulated in the following way

$$(4.39) \quad \sum_{\alpha} [2\rho_{i\alpha,i\alpha} - N_{i\alpha}^{atom}] = 0$$

which simply expresses the constraint that there is no charge transfer between orbitals associated with different atoms. However, the electrons are allowed to move between different orbitals of the same atom. The local charge neutrality is achieved by varying the on-site energies in a self-consistent way. First the excess charge on each atoms is calculated. Then the on-site energies at every atom are shifted by an amount proportional

to the excess charge. On atoms with an excess charge the on-site energies are increased, while on atoms with a lack of charge the on-site energy levels are decreased. This causes the excess charge to move to atoms with lack of it. The charges and the Fermi energy are then recalculated and the on-site energies adjusted in a self-consistent manner until the same fixed charge is attained on every atom. This self-consistent part of the calculation is very important since serious errors can arise for non-self-consistent-solutions due to the violation of charge conservation and the neglect of variations in the potential caused by charge flow (Sutton *et al.* 1988). Moreover, the local charge neutrality condition greatly simplifies the calculation of forces as will be seen in the following paragraph.

Forces on individual atoms can be obtained by differentiating the cohesive energy (4.29) with respect to the atomic positions

$$(4.40) \quad -F_k = \frac{\partial E_{coh}}{\partial r_k} = 2 \sum_{i\alpha \neq j\beta} \rho_{j\beta, i\alpha} \frac{\partial H_{i\alpha, j\beta}}{\partial r_k} + \frac{1}{2} \sum_{i \neq j} \frac{\partial \phi(r_{ij})}{\partial r_k} + \sum_{i\alpha} [2\rho_{i\alpha, i\alpha} - N_{i\alpha}^{atom}] \frac{\partial \epsilon_{i\alpha}}{\partial r_k}$$

Note that (4.40) does not contain any derivatives of the density matrix  $\rho_{i\alpha, j\beta}$ . This follows from the Hellmann-Feynman theorem (Hellmann 1937; Feynman 1939) according to which the force on an atom k is generally given as

$$(4.41) \quad F_k = - \left\langle \Psi \left| \frac{\partial \hat{H}}{\partial r_k} \right| \Psi \right\rangle$$

where  $\hat{H}$  is the Hamiltonian of the system studied and  $\Psi$  is the exact eigenfunction of this Hamiltonian. This theorem implies that the derivatives of the density matrix do not enter the formula for forces just as derivatives of  $\Psi$  do not appear in (4.41). It is

important to emphasize, however, that this is strictly correct only if the density matrix is calculated exactly. The first two terms in (4.40) are easy to calculate as they involve only the differentiation of the pair potential and the intersite elements of the Hamiltonian matrix  $H_{i\alpha,j\beta}$  which have a well-defined dependence on positions of atoms. The third term is more problematic as it involves the derivatives of onsite energies. This term however becomes zero if the condition of the local charge neutrality is applied. In the process of achieving LCN, the on-site energies associated with different orbitals centered on any given atom all shift by the same amount  $\delta\epsilon_{i\alpha} = \delta\epsilon_i$ , so that  $\frac{\partial\epsilon_{i\alpha}}{\partial r_k} = \frac{\partial\epsilon_i}{\partial r_k}$ . Thus using the LCN condition (4.39) we get

$$(4.42) \quad \sum_{i\alpha} [2\rho_{i\alpha,i\alpha} - N_{i\alpha}^{atom}] \frac{\partial\epsilon_{i\alpha}}{\partial r_k} = \sum_i \frac{\partial\epsilon_i}{\partial r_k} \sum_{\alpha} [2\rho_{i\alpha,i\alpha} - N_{i\alpha}^{atom}] = 0$$

The force acting an atom  $k$  is then

$$(4.43) \quad F_k = -2 \sum_{i\alpha \neq j\beta} \rho_{j\beta,i\alpha} \frac{\partial H_{i\alpha,j\beta}}{\partial r_k} - \frac{1}{2} \sum_{i \neq j} \frac{\partial \phi(r_{ij})}{\partial r_k}$$

which is relatively simple to evaluate provided we know the intersite elements of the density matrix. Hence, determination of the intersite elements of the density matrix is the core of the problem.

The density matrix can be calculated directly by solving the secular equation (4.14), but this approach has certain drawbacks. First of all, if we are not dealing with a small finite cluster but an effectively infinite block of atoms, periodic boundary condition, and related Bloch's theorem, need to be employed. This may be very inconvenient when

studying extended defects. Secondly it is computationally very demanding as the number of steps needed to diagonalize the matrix, and consequently the time of the calculation, scale as a cube of the number of atoms involved. An alternative approach is to construct the density matrix from an exact many-body expansion using the recursion method and Green's function formalism. There are no periodicity constraints and the computational time scales linearly with the number of atoms as will be shown in the next section. Considering the above mentioned advantages the recursion method will be used in the following.

### 1.1. The Moment Theorem

The local density of states can be expanded in terms of its moments as

$$(4.44) \quad n_{i\alpha}(E) = \sum_{p=0}^{\infty} \frac{\mu_{i\alpha}^{(p)}}{E^{p+1}}$$

where the  $p$ th moment is defined as

$$(4.45) \quad \mu_{i\alpha}^{(p)} = \int E^p n_{i\alpha}(E) dE$$

Using this so-called moment theorem (Cyrot-Lackmann,1968) it can be shown that the number of steps needed to reconstruct the local density of states depends only on how many moments are needed for a given precision, but not on the size of the system. The time needed to evaluate the total density of states, which is a sum of the local densities, therefore scales linearly with the number of atoms so that this approach becomes an  $O(N)$  method. To show this we write the  $p$ th moment as

$$(4.46) \quad \mu_{i\alpha}^{(p)} = \int E^p n_{i\alpha}(E) dE = \langle i\alpha | \hat{H}^p | i\alpha \rangle$$

After inserting  $(p-1)$  times the unity operator from equation (4.17) describing the completeness of the atomic orbital set, we get

$$(4.47) \quad \mu_{i\alpha}^{(p)} = \sum_{j_1\beta_1 \dots j_{p-1}\beta_{p-1}} \langle i\alpha | \hat{H} | j_1\beta_1 \rangle \langle j_1\beta_1 | \hat{H} | j_2\beta_2 \rangle \dots \langle j_{p-1}\beta_{p-1} | \hat{H} | i\alpha \rangle$$

or

$$(4.48) \quad \mu_{i\alpha}^{(p)} = \sum_{j_1\beta_1 \dots j_{p-1}\beta_{p-1}} H_{i\alpha, j_1\beta_1} H_{j_1\beta_1, j_2\beta_2} \dots H_{j_{p-1}\beta_{p-1}, i\alpha}$$

Equation (4.48) provides a link between the electronic structure and the local atomic coordination as it shows the correspondence between the  $p$ th moment and the process of hopping around the lattice along closed paths of “length  $p$ ”.

The  $p$ th moment of the local density of states corresponding to a state  $|i\alpha\rangle$  is the sum of the products of  $p$  Hamiltonian elements obtained by considering all possible paths composed of  $p$  hops starting and ending on the same atom  $i$  and state  $|i\alpha\rangle$ . The first moment corresponds to a single hop on the same atom,  $\mu_{i\alpha}^{(1)} = H_{i\alpha, i\alpha}$ , the second moment involves hops to all neighboring atoms and back,  $\mu_{i\alpha}^{(2)} = \sum_{\substack{j\beta \\ j \neq i}} H_{i\alpha, j\beta} H_{j\beta, i\alpha}$ , the third moment hops via two neighboring atoms and back, etc. The time to reconstruct the local density of states from the moment expansion for one site thus depends only on the number of required moments, as we wanted to show.

## 1.2. The Recursion Method and the Green's Function Formalism

Let us start this section by introducing the Lanczos algorithm (Lanczos 1950) which is an elegant mathematical technique used for tridiagonalization of sparse matrices. Applied to the Hamiltonian it creates the framework for the recursion method of evaluating the density matrix. It gives a recipe for finding a vector basis  $|U_n\rangle$  in which the Hamiltonian matrix takes up a tridiagonal form defined as

$$(4.49) \quad \langle U_m | \hat{H} | U_n \rangle = \begin{cases} a_n & \text{if } m = n \\ b_n & \text{if } m = n - 1 \\ b_{n+1} & \text{if } m = n + 1 \\ 0 & \text{otherwise} \end{cases}$$

Most of the elements of the tridiagonal matrix  $\hat{H}$  are zero save those on the neighboring positions around the main diagonal so that in this representation

$$(4.50) \quad \hat{H} = \begin{pmatrix} a_0 & b_1 & 0 & 0 & \dots \\ b_1 & a_1 & b_2 & 0 & \dots \\ 0 & b_2 & a_2 & b_3 & \dots \\ 0 & 0 & b_3 & a_3 & \dots \\ \vdots & \vdots & \vdots & \vdots & \ddots \end{pmatrix}$$

The Lanczos algorithm of finding such basis for a given Hamiltonian is based on the following recursive relation:

$$(4.51) \quad \hat{H}|U_n\rangle = a_n|U_n\rangle + b_n|U_{n-1}\rangle + b_{n+1}|U_{n+1}\rangle$$

and the fact that the basis states  $|U_n\rangle$  are orthonormal:

$$(4.52) \quad \langle U_m | U_n \rangle = \delta_{m,n}$$

We can start from any chosen state  $|U_0\rangle$ . For  $n = 0$  equation (4.51) gives

$$(4.53) \quad H|U_0\rangle = a_0|U_0\rangle + b_1|U_1\rangle$$

Applying  $\langle U_0 |$  to (4.53) from left and using the orthonormality condition we obtain  $a_0$  as

$$(4.54) \quad a_0 = \langle U_0 | H | U_0 \rangle.$$

From equation (4.53) we find  $b_1|U_1\rangle$

$$(4.55) \quad b_1|U_1\rangle = H|U_0\rangle - \langle U_0 | H | U_0 \rangle |U_0\rangle$$

so that we can write  $|U_1\rangle = \lambda [H|U_0\rangle - \langle U_0 | H | U_0 \rangle |U_0\rangle]$  where  $\lambda$  is determined from the condition of orthonormality  $\langle U_1 | U_1 \rangle = 1$ .

Knowing  $|U_1\rangle$  we get  $b_1$  by applying  $\langle U_1 |$  to (4.55)

$$(4.56) \quad b_1 = \langle U_1 | H | U_0 \rangle$$

Now that we know  $b_1$  and  $|U_1\rangle$ , using (4.51) for  $n = 1$  we can calculate  $a_1 = \langle U_1 | H | U_1 \rangle$ , and then  $|U_2\rangle$  and  $b_2$ . Repeating this for  $n = 2$  we obtain,  $a_2$  and then  $|U_3\rangle$  and  $b_3$ , and so on. In this way we are able to recreate both the basis and the elements of the tridiagonal matrix. The matrix elements  $a_n$ ,  $b_n$  are commonly called the recursion coefficients.

The main advantage of the recursion method is that it leads to a simple expression

for matrix elements of the Green's function of the Schrodinger equation that is defined in the following way

$$(4.57) \quad G(Z) = \frac{1}{Z - H} = [Z - H]^{-1}$$

When inverting  $(Z - H)$ , which is tridiagonal if expressed in the basis  $|U_n\rangle$ , by the determinant expansion method the matrix element of the Green's function  $G_{00}(Z) = \left\{ [Z - H]^{-1} \right\}_{00}$  has the form of a continuous fraction

$$(4.58) \quad G_{00}(Z) = \cfrac{1}{Z - a_0 - \cfrac{b_1^2}{Z - a_1 - \cfrac{b_2^2}{Z - a_2 - \cfrac{b_3^2}{\ddots}}}}$$

To obtain the diagonal element of the Green's function for an arbitrary state  $|\psi\rangle$  is therefore very simple. We set the initial state in the Lanczos algorithm  $|U_0\rangle$  equal to  $|\psi\rangle$ , calculate coefficients  $a_n$  and  $b_n$  recursively from the Lanczos algorithm and insert them into equation (4.58). This is very important since the Green's function elements can be directly related to the density matrix and/or bond order. From equations (4.22) and (4.36) we get

$$(4.59) \quad \Theta_{i\alpha, j\beta} = 2\rho_{i\alpha, j\beta} = 2 \sum_{n(occ)} \langle i\alpha | n \rangle \langle n | j\beta \rangle = 2 \int^E dE \langle i\alpha | \delta(E - H) | j\beta \rangle$$

Using the following form of the  $\delta$ -function

$$(4.60) \quad \delta(x) = -\frac{1}{\pi} \lim_{\eta \rightarrow 0} \text{Im} \left\{ [x + i\eta]^{-1} \right\}$$

we can write

$$(4.61) \quad \Theta_{i\alpha, j\beta} = 2\rho_{i\alpha, j\beta} = -\frac{2}{\pi} \lim_{\eta \rightarrow 0} \text{Im} \left\{ \int_{-\infty}^E dE \langle i\alpha | [E - H' + i\eta]^{-1} | j\beta \rangle \right\}$$

$$= -\frac{2}{\pi} \lim_{\eta \rightarrow 0} \text{Im} \left\{ \int_{-\infty}^E G_{i\alpha, j\beta}(E + i\eta) dE \right\}$$

where we used the definition of the Green's function from (4.57). If we now rewrite

(4.61) in terms of the bonding state  $|+\rangle$  and anti-bonding state  $|-\rangle$  defined by equations

(4.33) and (4.34), and substitute for  $G_{i\alpha, j\beta}(Z) = \frac{1}{2} [G_{++}(Z) - G_{--}(Z)]$  we get

$$(4.62) \quad \Theta_{i\alpha, j\beta} = -\frac{1}{\pi} \lim_{\eta \rightarrow 0} \text{Im} \left\{ \int_{-\infty}^E dE [G_{++}(E + i\eta) - G_{--}(E + i\eta)] \right\}$$

Equations (4.62) directly links the bond order parameter/density matrix with diagonal elements of the Green's function matrix. These diagonal elements for the bonding and anti-bonding state can be obtained using the recursion method and inserted into the above equation to give the density matrix. Thus, at this point we could claim that the problem is solved. It turns out, however, that the convergence of the difference of the two matrix

elements of the Green's function in (4.62) is far too slow for practical purposes. At the same time, to use the Hellmann-Feynman theorem for evaluation of forces a very accurately calculated density matrix is required. More refined methods have to be used to achieve faster convergence. In the bond-order potential algorithm the actual density matrix is, therefore, calculated from non-diagonal elements of the Green's function using the so-called exact many-body expansion described in section 4.3.

Using the tridiagonalized Hamiltonian (4.50) we can also rewrite the local density of states in terms of the recursion coefficients in the following way. If we take  $|i\alpha\rangle$  as the starting state for the Lanczos algorithm, the moments of the local density of state can be easily calculated from equation (4.46). The first few moments are

$$(4.63) \quad \mu_{i\alpha}^{(0)} = 1$$

$$\mu_{i\alpha}^{(1)} = a_0$$

$$\mu_{i\alpha}^{(2)} = a_0^2 + b_1^2$$

$$\mu_{i\alpha}^{(3)} = a_0^3 + 2a_0b_1^2 + a_1b_1^2$$

$$\mu_{i\alpha}^{(4)} = a_0^4 + 3a_0^2b_1^2 + a_0a_1b_1^2 + a_1^2b_1^2 + b_1^2b_2^2 + b_1^4$$

Equations (4.63) imply that calculation of each new moment requires an additional recursion coefficient. Knowing all the coefficients up to the N-th level ( $a_0, a_1, a_2, \dots, a_N$  and  $b_1, b_2, \dots, b_N$ ) allows us to calculate  $2N+1$  moments. When calculating the continuous fraction the recursion coefficients are usually evaluated only up to a certain level, say N, and all the remaining higher order coefficients are set equal to a constant ( $a_n = a_\infty$ ,

$b_n = b_\infty$  for  $n > N$ ). The part of the fraction containing only constant terms can be summed up exactly by realizing that

$$(4.64) \quad t(Z) = \frac{1}{Z - a_\infty - \frac{b_\infty^2}{Z - a_\infty - \frac{b_\infty^2}{Z - a_\infty - \frac{b_\infty^2}{\ddots}}}} = \frac{1}{Z - a_\infty - b_\infty^2 t(Z)}$$

Hence

$$(4.65) \quad Zt(Z) - a_\infty t(Z) - b_\infty^2 t^2(Z) = 1$$

By solving the quadratic equation for  $t(Z)$  we get

$$(4.66) \quad t(Z) = \frac{1}{b_\infty} \left[ \left( \frac{Z - a_\infty}{2b_\infty} \right) - i \sqrt{1 - \left( \frac{Z - a_\infty}{2b_\infty} \right)^2} \right]$$

The above expression is used to terminate the continued fractions at a finite level and is referred to as the square root terminator (Beer and Pettifor 1984). It is important to note that the use of the square-root terminator is limited to metallic systems where the total electronic density of states can be represented by a single continuous band. Using the square-root terminator for a semiconducting material with a band-gap may result in a very poor convergence caused by the oscillatory behavior of the recursion coefficients. The solution in this case is the so-called Turchi's termination that takes into account the gap in semiconductors and the existence of two separate bands (Turchi and Ducastelle 1985).

### 4.3 Many-Body Expansion for the Bond-Order

The remaining part of the chapter closely follows the paper by Horsfield *et al.*, 1996. We start this section by introducing the concept of the auxiliary space (Aoki 1993). The auxiliary space is a vector space spanned by vectors  $|e_{i\alpha}\rangle$ . These vectors do not have to be orthonormal and their inner product does not have any particular meaning apart from bond labeling. The inner product in the auxiliary space is defined as

$$(4.67) \quad (e_{j\beta}|e_{i\alpha}) = \Lambda_{j\beta,i\alpha}$$

where  $\Lambda_{j\beta,i\alpha}$  is the so-called bond label matrix that satisfies the following condition

$$(4.68) \quad \sum_{i\alpha} \Lambda_{i\alpha,i\alpha} = 1$$

Each vector  $|e_{i\alpha}\rangle$  in the auxiliary space has a unique corresponding vector  $|i\alpha\rangle$  in the Hilbert vector space of atomic-like orbitals. By the direct product of the auxiliary space and the Hilbert space we can create another vector space called the augmented space. The basis of the augmented space consists of the vectors of the form  $|e_{i\alpha}\rangle|j\beta\rangle$ . In the following we will be using a special class of vectors in the augmented space denoted  $|W_0^\wedge\rangle$  defined as

$$(4.69) \quad |W_0^\wedge\rangle = \sum_{i\alpha} |e_{i\alpha}\rangle|i\alpha\rangle$$

The operators defined in the Hilbert space, such as the Hamiltonian, do not act on vectors in the auxiliary space  $|e_{i\alpha}\rangle$ . If we are to use the Hilbert space operators in the augmented space we have to provide a recipe for their action. We can do so by defining the

Hamiltonian matrix element for the composite vectors  $|W_0^\Lambda\rangle$ , since those are the only ones we will be using. That matrix element is given by

$$(4.70) \quad \frac{\{W_0^\Lambda | f(\hat{H}) | W_0^\Lambda\}}{\{W_0^\Lambda | W_0^\Lambda\}} = \frac{\sum_{i\alpha, j\beta} \Lambda_{i\alpha, j\beta} \langle i\alpha | f(\hat{H}) | j\beta \rangle}{\sum_{i\alpha, j\beta} \Lambda_{i\alpha, j\beta} \langle i\alpha | j\beta \rangle} = \sum_{i\alpha, j\beta} \Lambda_{i\alpha, j\beta} \langle i\alpha | f(\hat{H}) | j\beta \rangle$$

where we have used the fact that vectors in the augmented space are normalized because the atomic orbitals are normalized and auxiliary vectors satisfy the condition (4.68)

$$(4.71) \quad \{W_0^\Lambda | W_0^\Lambda\} = \sum_{i\alpha, j\beta} \Lambda_{i\alpha, j\beta} \langle i\alpha | j\beta \rangle = \sum_{i\alpha} \Lambda_{i\alpha, i\alpha} = 1$$

Even though using the augmented space may look complicated at the first sight, it facilitates greatly the derivation of the many-body expansion and provides a general framework for defining the bond-order formalism. It also allows us to formulate the important sum rules for the Green's function as will be shown later on in this chapter.

In order to derive the bond-order potential formalism, we apply the recursion method in the augmented space. The Lanczos algorithm can be used in the same way as in the Hilbert space only now with vectors from the augmented space. As mentioned in the previous section, the convergence of the recursion method for diagonal elements of the Green's function is too slow for practical purposes. A similar routine for off-diagonal elements of the Green's function has, therefore, been developed. We will show its derivation in the augmented space.

Rewriting equation (4.57) as

$$(4.72) \quad (Z - \hat{H}) \mathcal{G} = \mathcal{V}$$

we can write

$$(4.73) \quad \left\{ U_n \middle| \mathcal{V} \middle| U_m \right\} = \left\{ U_n \middle| (Z - \hat{H}) \mathcal{G}(Z) \middle| U_m \right\}$$

Inserting in the Lanczos formula (4.51) we obtain the following recursive relation

$$(4.74) \quad \delta_{n,m} = (Z - a_n) G_{nm}(Z) - b_n G_{n-1,m}(Z) - b_{n+1} G_{n+1,m}(Z)$$

which can be used to calculate all the elements  $G_{0n}(Z)$  from  $G_{00}(Z)$ .

Now let us take  $|W_0^\Lambda\rangle$  to be the starting vector for the Lanczos algorithm in the augmented space. The corresponding diagonal Green's function matrix element is

$$(4.75) \quad G_{00}^\Lambda(Z) = \langle W_0^\Lambda | \mathcal{G}(Z) | W_0^\Lambda \rangle = \sum_{i\alpha, j\beta} G_{i\alpha, j\beta}(Z) \Lambda_{i\alpha, j\beta}$$

From the above equation we can express any non-diagonal element of the Green's function as a derivative of the diagonal element with respect to  $\Lambda_{i\alpha, j\beta}$

$$(4.76) \quad G_{i\alpha, j\beta}(Z) = \frac{\partial G_{00}^\Lambda(Z)}{\partial \Lambda_{i\alpha, j\beta}}$$

To find the variation of  $G_{00}^\Lambda$  with  $\lambda$  we need to know the first order change in the Green's function due to a small variation of the Hamiltonian  $\delta\hat{H}$ . We can write the Green's function as

$$(4.77) \quad \mathcal{G}(Z)^{-1} = Z - \hat{H} = Z - \hat{H}_0 - \delta\hat{H}$$

and multiply it by the unperturbed Green's function  $\mathcal{G}_0^\Lambda(Z) = (Z - \hat{H}_0)_{\Lambda}^{-1}$  from the left and

by  $\mathcal{G}'(Z)$  from the right to get the Dyson's equation

$$(4.78) \quad \begin{aligned} \mathcal{G}'(Z) &= \mathcal{G}'_0(Z) + \mathcal{G}'_0(Z)\delta\mathcal{H}\mathcal{G}'(Z) \\ &= \mathcal{G}'_0(Z) + \mathcal{G}'_0(Z)\delta\mathcal{H}\mathcal{G}'_0(Z) + \dots \end{aligned}$$

Here we used  $\mathcal{G}'_0(Z)(Z - \mathcal{H}_0) = 1$ . The variation of the Green's function to the first-order

is thus

$$(4.79) \quad \delta\mathcal{G}'(Z) = \mathcal{G}'(Z) - \mathcal{G}'_0(Z) = \mathcal{G}'_0(Z)\delta\mathcal{H}\mathcal{G}'_0(Z)$$

Using the completeness property, and the fact that the Hamiltonian is tridiagonal, we obtain

$$\begin{aligned} (4.80) \quad \delta G_{00}^\Lambda(Z) &= \left\langle W_0^\Lambda \middle| \delta\mathcal{G}'(Z) \middle| W_0^\Lambda \right\rangle \\ &= \sum_n \sum_m \left\langle W_0^\Lambda \middle| \mathcal{G}'(Z) \middle| W_m^\Lambda \right\rangle \left\langle W_m^\Lambda \middle| \delta\mathcal{H} \middle| W_n^\Lambda \right\rangle \left\langle W_n^\Lambda \middle| \mathcal{G}'(Z) \middle| W_0^\Lambda \right\rangle \\ &= \sum_{n,m} G_{0n}^\Lambda(Z) \delta H_{nm}^\Lambda G_{m0}^\Lambda(Z) \\ &= \sum_n \left\{ G_{0n}^\Lambda(Z) \delta H_{nn}^\Lambda G_{n0}^\Lambda(Z) + G_{0n}^\Lambda(Z) \delta H_{n(n-1)}^\Lambda G_{(n-1)0}^\Lambda(Z) + G_{0(n-1)}^\Lambda(Z) \delta H_{(n-1)n}^\Lambda G_{n0}^\Lambda(Z) \right\} \\ &= \sum_{n=0}^{\infty} G_{0n}^\Lambda(Z) G_{n0}^\Lambda(Z) \delta a_n + \sum_{n=1}^{\infty} G_{0n}^\Lambda(Z) G_{(n-1)0}^\Lambda(Z) \delta b_n \end{aligned}$$

where

$$(4.81) \quad G_{mn}^\Lambda(Z) = \left\langle W_m^\Lambda \middle| \mathcal{G}'(Z) \middle| W_n^\Lambda \right\rangle$$

Substituting  $\delta G_{00}^\Lambda(Z)$  into equation (4.76), we finally get

$$(4.82) \quad G_{i\alpha, j\beta}(Z) = \sum_{n=0}^{\infty} G_{0n}^{\Lambda}(Z) G_{n0}^{\Lambda}(Z) \frac{\partial a_n^{\Lambda}}{\partial \Lambda_{i\alpha, j\beta}} + 2 \sum_{n=1}^{\infty} G_{0(n-1)}^{\Lambda}(Z) G_{n0}^{\Lambda}(Z) \frac{\partial b_n^{\Lambda}}{\partial \Lambda_{i\alpha, j\beta}}$$

The above equation is the so-called exact many-body expansion for the Green's function:

If we introduce the function  $\chi_{0m,n0}^{\Lambda}$ , also called the response function, as

$$(4.83) \quad \chi_{0m,n0}^{\Lambda} = \frac{1}{\pi} \lim_{\eta \rightarrow 0} \text{Im} \int_{-\infty}^E dE G_{0m}^{\Lambda}(E + i\eta) G_{n0}^{\Lambda}(E + i\eta)$$

and use equation (4.61), we can rewrite the many-body expansion of the Green's function in terms of the bond-order as

$$(4.84) \quad \Theta_{i\alpha, j\beta}(Z) = -2 \left[ \sum_{n=0}^{\infty} \chi_{0n,n0}^{\Lambda} \frac{\partial a_n^{\Lambda}}{\partial \Lambda_{i\alpha, j\beta}} + \chi_{0(n-1),n0}^{\Lambda} \frac{\partial b_n^{\Lambda}}{\partial \Lambda_{i\alpha, j\beta}} \right]$$

As mentioned before, the off-diagonal matrix elements of the Green's function  $G_{0k}^{\Lambda}(Z) = G_{k0}^{\Lambda}(Z)$  can be calculated from the diagonal elements using the recursive relation (4.73). Thus we are able to calculate the response functions  $\chi_{0m,n0}^{\Lambda}$  and the only quantities left to be determined are the derivatives of the recursive coefficients with respect to  $\Lambda_{i\alpha, j\beta}$ , used in the above equation. The mathematical formalism used for this purpose in the next paragraph may look a little awkward, but it produces a very simple result worth all the effort.

Let us first summarize the Lanczos algorithm for the compound vectors  $|W_n^{\Lambda}\rangle$  in the augmented space. The generalized recursive relation becomes

$$(4.85) \quad \langle W_n^\Lambda | H | W_n^\Lambda \rangle = a_n^\Lambda |W_n^\Lambda\rangle + b_n^\Lambda |W_{n-1}^\Lambda\rangle + b_{n+1}^\Lambda |W_{n+1}^\Lambda\rangle$$

with the vector set being orthonormal

$$(4.86) \quad \langle W_n^\Lambda | W_m^\Lambda \rangle = \delta_{n,m}$$

To simplify the notation we introduce a set of orthogonal polynomials  $P_n^\Lambda(x)$

$$(4.87) \quad x P_n^\Lambda(x) = a_n^\Lambda P_n^\Lambda(x) + b_n^\Lambda P_{n-1}^\Lambda(x) + b_{n+1}^\Lambda P_{n+1}^\Lambda(x)$$

with the first two  $P_{-1}^\Lambda(x) = 0$  and  $P_0^\Lambda(x) = 1$ . Using such polynomials we can reformulate the expressions for the  $n$ -th recursion vector  $|W_n^\Lambda\rangle$  and the generalized recursion coefficients  $a_n^\Lambda, b_n^\Lambda$  as follows

$$(4.88) \quad |W_n^\Lambda\rangle = P_n^\Lambda(H) |W_0^\Lambda\rangle = \sum_{i\alpha} P_n^\Lambda(H) |i\alpha\rangle |e_{i\alpha}^\Lambda\rangle$$

$$(4.89) \quad a_n^\Lambda = \langle W_n^\Lambda | H | W_n^\Lambda \rangle = \sum_{i\alpha, j\beta} \langle i\alpha | P_n^\Lambda(H) H P_n^\Lambda(H) | j\beta \rangle \Lambda_{i\alpha, j\beta}$$

$$(4.90) \quad b_n^\Lambda = \langle W_{n-1}^\Lambda | H | W_n^\Lambda \rangle = \sum_{i\alpha, j\beta} \langle i\alpha | P_{n-1}^\Lambda(H) H P_n^\Lambda(H) | j\beta \rangle \Lambda_{i\alpha, j\beta}$$

We can also rewrite the orthonormality relation as

$$(4.91) \quad \delta_{m,n} = \langle W_m^\Lambda | W_n^\Lambda \rangle = \sum_{i\alpha, j\beta} \langle i\alpha | P_m^\Lambda(H) P_n^\Lambda(H) | j\beta \rangle \Lambda_{i\alpha, j\beta},$$

By differentiating (4.89), (4.90) and (4.91) with respect to the bond label matrix element  $\Lambda_{i\alpha, j\beta}$ , we obtain

$$(4.92) \quad \frac{\partial a_n^\Lambda}{\partial \Lambda_{i\alpha, j\beta}} = \left\langle ia \left| P_n^\Lambda(\hat{H}) \hat{H} P_n^\Lambda(\hat{H}) \right| j\beta \right\rangle + 2 \left\{ W_0^\Lambda \left| \frac{\partial P_n^\Lambda(\hat{H})}{\partial \Lambda_{i\alpha, j\beta}} \hat{H} P_n^\Lambda(\hat{H}) \right| W_0^\Lambda \right\}$$

$$(4.93) \quad \frac{\partial b_n^\Lambda}{\partial \Lambda_{i\alpha, j\beta}} = \left\langle ia \left| P_{n-1}^\Lambda(\hat{H}) \hat{H} P_n^\Lambda(\hat{H}) \right| j\beta \right\rangle + \left\{ W_0^\Lambda \left| \frac{\partial P_{n-1}^\Lambda(\hat{H})}{\partial \Lambda_{i\alpha, j\beta}} \hat{H} P_n^\Lambda(\hat{H}) \right| W_0^\Lambda \right\} +$$

$$(4.94) \quad 0 = O_{i\alpha, j\beta}^{\Lambda, m, n} + \left\{ W_0^\Lambda \left| \frac{\partial P_m^\Lambda(\hat{H})}{\partial \Lambda_{i\alpha, j\beta}} P_n^\Lambda(\hat{H}) \right| W_0^\Lambda \right\} + \left\{ W_0^\Lambda \left| P_m^\Lambda(\hat{H}) \frac{\partial P_n^\Lambda(\hat{H})}{\partial \Lambda_{i\alpha, j\beta}} \right| W_0^\Lambda \right\}$$

where the matrix  $O$  is defined as

$$(4.95) \quad O_{i\alpha, j\beta}^{\Lambda, m, n} = \left\langle i\alpha \left| P_m^\Lambda(\hat{H}) P_n^\Lambda(\hat{H}) \right| j\beta \right\rangle$$

Differentiating the polynomial  $P_m^\Lambda(\hat{H})$  with respect to parameter  $\Lambda_{i\alpha, j\beta}$  does not change the order of the polynomial. Provided  $m < n$ , the polynomial  $P_n^\Lambda(\hat{H})$ , which is orthogonal to all polynomials of lower order, will also be orthogonal to the derivative of  $P_m^\Lambda(\hat{H})$ . Thus we can write

$$(4.96) \quad \left\{ W_0^\Lambda \left| \frac{\partial P_m^\Lambda(\hat{H})}{\partial \Lambda_{i\alpha, j\beta}} P_n^\Lambda(\hat{H}) \right| W_0^\Lambda \right\} = 0 \quad (m < n)$$

Inserting (4.87) into (4.93) and (4.94) we get

$$(4.97) \quad \frac{\partial a_n^\Lambda}{\partial \Lambda_{i\alpha, j\beta}} = \left\langle ia \left| P_n^\Lambda(\hat{H}) \right| \left[ b_n^\Lambda P_{n-1}^\Lambda(\hat{H}) + a_n^\Lambda P_n^\Lambda(\hat{H}) + b_{n+1}^\Lambda P_{n+1}^\Lambda(\hat{H}) \right] \right| j\beta \right\rangle +$$

$$+ 2 \left\{ W_0^\Lambda \left| \frac{\partial P_n^\Lambda(\hat{H})}{\partial \Lambda_{i\alpha, j\beta}} \left[ b_n^\Lambda P_{n-1}^\Lambda(\hat{H}) + a_n^\Lambda P_n^\Lambda(\hat{H}) + b_{n+1}^\Lambda P_{n+1}^\Lambda(\hat{H}) \right] \right| W_0^\Lambda \right\}$$

$$(4.98) \quad \frac{\partial b_n^\Lambda}{\partial \Lambda_{i\alpha, j\beta}} = \left\langle ia \left| P_{n-1}^\Lambda(\hat{H}) \right| \left[ b_n^\Lambda P_{n-1}^\Lambda(\hat{H}) + a_n^\Lambda P_n^\Lambda(\hat{H}) + b_{n+1}^\Lambda P_{n+1}^\Lambda(\hat{H}) \right] \right| j\beta \right\rangle +$$

$$+ \left\{ W_0^\Lambda \left| \frac{\partial P_{n-1}^\Lambda(\hat{H})}{\partial \Lambda_{i\alpha, j\beta}} \left[ b_n^\Lambda P_{n-1}^\Lambda(\hat{H}) + a_n^\Lambda P_n^\Lambda(\hat{H}) + b_{n+1}^\Lambda P_{n+1}^\Lambda(\hat{H}) \right] \right| W_0^\Lambda \right\} +$$

$$+ \left\{ W_0^\Lambda \left| \left[ b_n^\Lambda P_{n-1}^\Lambda(\hat{H}) + a_n^\Lambda P_n^\Lambda(\hat{H}) + b_{n+1}^\Lambda P_{n+1}^\Lambda(\hat{H}) \right] \frac{\partial P_n^\Lambda(\hat{H})}{\partial \Lambda_{i\alpha, j\beta}} \right| W_0^\Lambda \right\}$$

We can simplify the above expressions by considering the orthogonality condition (4.96)  
and the definition of the  $O$  matrix (4.95)

$$(4.99) \quad \frac{\partial a_n^\Lambda}{\partial \Lambda_{i\alpha, j\beta}} = b_n^\Lambda O_{i\alpha, j\beta}^{\Lambda, n, n-1} + a_n^\Lambda O_{i\alpha, j\beta}^{\Lambda, n, n} + b_{n+1}^\Lambda O_{i\alpha, j\beta}^{\Lambda, n+1, n} +$$

$$+ 2 \left\{ W_0^\Lambda \left| \frac{\partial P_n^\Lambda(\hat{H})}{\partial \Lambda_{i\alpha, j\beta}} \left[ b_n^\Lambda P_{n-1}^\Lambda(\hat{H}) + a_n^\Lambda P_n^\Lambda(\hat{H}) \right] \right| W_0^\Lambda \right\}$$

$$(4.100) \quad \frac{\partial b_n^\Lambda}{\partial \Lambda_{i\alpha, j\beta}} = b_n^\Lambda O_{i\alpha, j\beta}^{\Lambda, n-1, n-1} + a_n^\Lambda O_{i\alpha, j\beta}^{\Lambda, n-1, n} + b_{n+1}^\Lambda O_{i\alpha, j\beta}^{\Lambda, n-1, n+1} +$$

$$+ \left\{ W_0^\Lambda \left| \frac{\partial P_{n-1}^\Lambda(\hat{H})}{\partial \Lambda_{i\alpha,j\beta}} b_n^\Lambda P_{n-1}^\Lambda(\hat{H}) \right| W_0^\Lambda \right\} + \\ + \left\{ W_0^\Lambda \left[ \left[ b_n^\Lambda P_{n-1}^\Lambda(\hat{H}) + a_n^\Lambda P_n^\Lambda(\hat{H}) \right] \frac{\partial P_n^\Lambda(\hat{H})}{\partial \Lambda_{i\alpha,j\beta}} \right| W_0^\Lambda \right\}$$

From equation (4.94) we can rewrite all the remaining matrix elements in terms of the  $O$  matrix. Condition (4.96) eliminates some of the terms, and finally the expressions for derivatives of the recursion coefficients simplify to

$$(4.101) \quad \frac{\partial a_n^\Lambda}{\partial \Lambda_{i\alpha,j\beta}} = b_{n+1}^\Lambda O_{i\alpha,j\beta}^{\Lambda,n+1,n} - b_n^\Lambda O_{i\alpha,j\beta}^{\Lambda,n,n-1}$$

$$(4.102) \quad 2 \frac{\partial b_n^\Lambda}{\partial \Lambda_{i\alpha,j\beta}} = b_n^\Lambda (O_{i\alpha,j\beta}^{\Lambda,n,n} - O_{i\alpha,j\beta}^{\Lambda,n-1,n-1})$$

These simple expressions can be used in equation for the exact many-body expansion of the bond-order (4.84)

$$(4.103) \quad \Theta_{i\alpha,j\beta}(Z) = - \left[ \sum_{n=0}^{\infty} 2 \chi_{0n,n0}^\Lambda (b_{n+1}^\Lambda O_{i\alpha,j\beta}^{\Lambda,n+1,n} - b_n^\Lambda O_{i\alpha,j\beta}^{\Lambda,n,n-1}) + \chi_{0(n-1),n0}^\Lambda b_n^\Lambda (O_{i\alpha,j\beta}^{\Lambda,n,n} - O_{i\alpha,j\beta}^{\Lambda,n-1,n-1}) \right]$$

To finish our task we still need to find the  $O$  matrix. Its elements can be calculated using the recursive relation

$$(4.104) \quad b_m^\Lambda O_{i\alpha,j\beta}^{\Lambda,m,n} = (a_n^\Lambda - a_{m-1}^\Lambda) O_{i\alpha,j\beta}^{\Lambda,m-1,n} - b_{m-1}^\Lambda O_{i\alpha,j\beta}^{\Lambda,m-2,n} + b_n^\Lambda O_{i\alpha,j\beta}^{\Lambda,m-1,n-1} + b_{n+1}^\Lambda O_{i\alpha,j\beta}^{\Lambda,m-1,n+1}$$

which is obtained from the identity

$$(4.105) \quad \left\langle i\alpha \left| P_{m-1}^\Lambda(\hat{H}) (\hat{H} P_n^\Lambda(\hat{H})) \right| j\beta \right\rangle = \left\langle i\alpha \left| (\hat{H} P_{m-1}^\Lambda(\hat{H})) P_n^\Lambda(\hat{H}) \right| j\beta \right\rangle$$

by substituting for  $\hat{H} P_n^\Lambda(\hat{H})$  from equation (4.87).

#### 4.4 Truncating the Many-Body Expansion and Using the Sum Rules

Since the calculation must be done in a finite time we have to truncate the many-body expansion at some point. The local density of states on a given atom will always be affected by several neighboring atomic shells. This dictates how many recursion levels need to be accounted for in the many-body expansion (4.84). In most metals four neighbor shells are sufficient for accurate description of the electronic density enabling to distinguish between different kinds of close-packed structures (see Chapter 6). The rest of the crystal can be ignored without significant deviation from the full result. This limits significantly the computational effort and makes the time of the calculation scale linearly with the total number of atoms.

There are some constraints that have to be satisfied when terminating many-body expansion; otherwise the results may become dependent on the choice of the coordinate system. In particular, it is essential that complete equivalence between the onsite and intersite description of the bond energy be preserved when the recursion series is terminated. This can be assured by introducing the so-called sum rules that will be reproduced in the following.

We start by considering the matrix element of the identity  $G(Z)(Z - H) = 1$

$$(4.106) \quad \left\{ W_0^\Lambda \left| (Z - H) G(Z) \right| W_0^\Lambda \right\} = Z G_{00}^\Lambda(Z) - \sum_{i\alpha, j\beta} \Lambda_{i\alpha, j\beta} \left\langle i\alpha \left| H G(Z) \right| j\beta \right\rangle = 1$$

Inserting a complete set of states  $\sum_{k\gamma} |k\gamma\rangle\langle k\gamma|$  and expanding the Green's function's matrix

element using (4.82), the following relation between the on-site and intersite description is obtained:

(4.107)

$$\begin{aligned} ZG_{00}^{\Lambda}(Z) - \sum_{i\alpha, j\beta} \Lambda_{i\alpha, j\beta} \sum_{k\gamma} H_{i\alpha, k\gamma} G_{k\gamma, j\beta}(Z) &= \\ = ZG_{00}^{\Lambda}(Z) - \sum_{i\alpha, j\beta, k\gamma} \Lambda_{i\alpha, j\beta} H_{i\alpha, k\gamma} &\times \\ \times \left[ \sum_{n=0}^{\infty} G_{0n}^{\Lambda}(Z) G_{n0}^{\Lambda}(Z) \frac{\partial a_n^{\Lambda}}{\partial \Lambda_{k\gamma, j\beta}} + 2 \sum_{n=1}^{\infty} G_{0(n-1)}^{\Lambda}(Z) G_{n0}^{\Lambda}(Z) \frac{\partial b_n^{\Lambda}}{\partial \Lambda_{k\gamma, j\beta}} \right] &= 1 \end{aligned}$$

We can ensure that equation (4.107) is satisfied by imposing the sum rules on the derivatives of the recursion coefficients. For this purpose we multiply equations (4.101) and (4.102) by  $\Lambda_{i\alpha, j\beta}$  and sum over  $\sum_{i\alpha, j\beta}$  to get

$$(4.108) \quad \sum_{i\alpha, j\beta} \frac{\partial a_n^{\Lambda}}{\partial \Lambda_{i\alpha, j\beta}} \Lambda_{i\alpha, j\beta} = b_{n+1}^{\Lambda} \{ W_{n+1}^{\Lambda} | W_n^{\Lambda} \} - b_n^{\Lambda} \{ W_n^{\Lambda} | W_{n-1}^{\Lambda} \} = 0$$

$$(4.109) \quad \sum_{i\alpha, j\beta} \frac{\partial b_n^{\Lambda}}{\partial \Lambda_{i\alpha, j\beta}} \Lambda_{i\alpha, j\beta} = b_n^{\Lambda} \left[ \{ W_n^{\Lambda} | W_n^{\Lambda} \} - \{ W_{n-1}^{\Lambda} | W_{n-1}^{\Lambda} \} \right] = 0$$

In the above we used the following formula

$$(4.110) \quad \sum_{i\alpha, j\beta} \Lambda_{i\alpha, j\beta} O_{i\alpha, j\beta}^{\Lambda, m, n} = \sum_{i\alpha, j\gamma} \Lambda_{i\alpha, j\beta} \left\langle i\alpha \left| P_m^{\Lambda} \left( \hat{H} \right) P_n^{\Lambda} \left( \hat{H} \right) \right| j\beta \right\rangle = \{ W_m^{\Lambda} | W_n^{\Lambda} \} = \delta_{m,n}$$

Equations (4.108) and (4.109) represent the first sum rule. We can get the second sum rule by multiplying (4.101) and (4.102) by  $\Lambda_{i\alpha, j\beta} H_{k\gamma, j\beta}$  and summing over  $\sum_{i\alpha, j\beta, k\gamma}$

$$(4.111) \quad \sum_{i\alpha, j\beta, k\gamma} \frac{\partial a_n^\Lambda}{\partial \Lambda_{i\alpha, j\beta}} \Lambda_{i\alpha, j\beta} H_{k\gamma, j\beta} = b_{n+1}^\Lambda \left\{ W_{n+1}^\Lambda \left| \hat{H} \right| W_n^\Lambda \right\} - b_n^\Lambda \left\{ W_n^\Lambda \left| \hat{H} \right| W_{n-1}^\Lambda \right\} = b_{n+1}^2 - b_n^2$$

$$\sum_{i\alpha, j\beta, k\gamma} 2 \frac{\partial b_n^\Lambda}{\partial \Lambda_{i\alpha, j\beta}} \Lambda_{i\alpha, j\beta} H_{k\gamma, j\beta} = b_n^\Lambda \left[ \left\{ W_n^\Lambda \left| \hat{H} \right| W_n^\Lambda \right\} - \left\{ W_{n-1}^\Lambda \left| \hat{H} \right| W_{n-1}^\Lambda \right\} \right] = b_n (a_n - a_{n-1})$$

where we used the following form of the matrix element

$$(4.112) \quad \left\{ W_n^\Lambda \left| \hat{H} \right| W_m^\Lambda \right\} = \sum_{i\alpha, j\beta} \Lambda_{i\alpha, j\beta} \left\langle i\alpha \left| P_m^\Lambda (\hat{H}) \hat{H} P_n^\Lambda (\hat{H}) \right| j\beta \right\rangle =$$

$$= \sum_{i\alpha, j\beta, k\gamma} \Lambda_{i\alpha, j\beta} \left\langle i\alpha \left| P_n^\Lambda (\hat{H}) P_m^\Lambda (\hat{H}) \right| k\gamma \right\rangle \left\langle k\gamma \left| \hat{H} \right| j\beta \right\rangle =$$

$$= \sum_{i\alpha, j\beta, k\gamma} \Lambda_{i\alpha, j\beta} O_{i\alpha, k\gamma}^{\Lambda, n, m} H_{k\gamma, j\beta}$$

If we insert (4.111) into (4.107) and use the recursive relation (4.73) for the Green's function's elements we can prove that the identity (4.107) holds.

Now that we know the sum rules we must make sure that the many-body expansion (4.84) terminates in such a way that the sum rules are always satisfied. Let us consider that the recursion coefficients are calculated exactly up to the N-th level. If the square-root terminator (see equation (4.64)) is used, all remaining recursion coefficients are set equal to constants  $a_n = a_\infty$ ,  $b_n = b_\infty$  for  $n > N$ . In this way we automatically satisfy the first sum rule since all the derivatives of the approximated recursion coefficients are zero. In the second set of sum rules the left-hand sides are zero for the same reason, but the right-hand sides are guaranteed to be zero by  $a_n = a_{n-1} = a_\infty$  only for  $n > N$  in the first equation and by  $b_{n+1} = b_n = b_\infty$  only for  $n > (N+1)$  in the second equation. So we still have to check the validity of the second sum rule for  $\partial a_N / \partial \Lambda_{i\alpha, j\beta}$  and  $\partial b_{N+1} / \partial \Lambda_{i\alpha, j\beta}$ .

Since the first  $N$  recursion coefficients are calculated exactly the sum rules hold for  $n \leq (N-1)$ . If we take the first equation of the second sum rule for  $n=0$  and multiply it by  $\left[\left(b_{\infty}^{\Lambda}\right)^2 - \left(b_N^{\Lambda}\right)^2\right] / \left(b_1^{\Lambda}\right)^2$  we get

$$(4.113) \quad \sum_{i\alpha, j\beta, k\gamma} \frac{\partial a_0^{\Lambda}}{\partial \Lambda_{i\alpha, k\gamma}} \frac{\left(b_{\infty}^{\Lambda}\right)^2 - \left(b_N^{\Lambda}\right)^2}{\left(b_1^{\Lambda}\right)^2} \Lambda_{i\alpha, j\beta} H_{k\gamma, j\beta} = \left(b_1^{\Lambda}\right)^2 \frac{\left(b_{\infty}^{\Lambda}\right)^2 - \left(b_N^{\Lambda}\right)^2}{\left(b_1^{\Lambda}\right)^2}$$

Setting  $\frac{\partial a_N^{\Lambda}}{\partial \Lambda_{i\alpha, j\beta}}$  equal to

$$(4.114) \quad \frac{\partial a_N^{\Lambda}}{\partial \Lambda_{i\alpha, j\beta}} = \frac{\partial a_0^{\Lambda}}{\partial \Lambda_{i\alpha, j\beta}} \frac{\left(b_{\infty}^{\Lambda}\right)^2 - \left(b_N^{\Lambda}\right)^2}{\left(b_1^{\Lambda}\right)^2}$$

equation (4.111) is automatically satisfied for  $a_N^{\Lambda}$ . It is then easy to check that the first sum rule, (4.108), also holds for coefficients  $a_N^{\Lambda}$ . Taking the second sum rule for  $a_0^{\Lambda}$  and multiplying it by  $b_{\infty}^{\Lambda} \left(a_{\infty}^{\Lambda} - a_N^{\Lambda}\right) / \left(b_1^{\Lambda}\right)^2$ , we obtain:

$$(4.115) \quad \sum_{i\alpha, j\beta, k\gamma} 2 \frac{\partial a_0^{\Lambda}}{\partial \Lambda_{i\alpha, k\gamma}} \frac{b_{\infty}^{\Lambda} \left(a_{\infty}^{\Lambda} - a_N^{\Lambda}\right)}{2 \left(b_1^{\Lambda}\right)^2} \Lambda_{i\alpha, j\beta} H_{k\gamma, j\beta} = \left(b_1^{\Lambda}\right)^2 \frac{b_{\infty}^{\Lambda} \left(a_{\infty}^{\Lambda} - a_N^{\Lambda}\right)}{\left(b_1^{\Lambda}\right)^2}$$

Again by putting

$$(4.116) \quad \frac{\partial b_{N+1}^{\Lambda}}{\partial \Lambda_{i\alpha, j\beta}} = \frac{\partial a_0^{\Lambda}}{\partial \Lambda_{i\alpha, j\beta}} \frac{b_{\infty}^{\Lambda} \left(a_{\infty}^{\Lambda} - a_N^{\Lambda}\right)}{2 \left(b_1^{\Lambda}\right)^2}$$

we have satisfied both sum rules for the coefficient  $b_N^{\Lambda}$ .

The truncation of the many-body expansion for the bond-order is done according to the sum rules using expressions (4.114) and (4.116) for  $\partial a_N / \partial \Lambda_{i\alpha, j\beta}$  and  $\partial b_{N+1} / \partial \Lambda_{i\alpha, j\beta}$ . As already mentioned, the use of the sum rules serves the purpose of conserving the equivalence of the on-site and intersite formalism and in this way assure the proper convergence of the method.

## 4.5 Effective Electronic Temperature

In order to improve the convergence of the bond-order potential formalism further, the so-called effective electronic temperature,  $T_e$ , has been introduced into the method. This temperature has nothing to do with the real temperature of the material and it serves solely as a convenient computational trick enabling the use of a smaller number of recursion levels. It is used to dampen the range of the Friedel's oscillations which may be rather large, namely in metals, due to the weak singularity of the screening functions at the Fermi energy (Girshick, 1997).

Introducing the electronic temperature into the framework of the bond-order potential at this stage is straightforward. The only part that needs to be changed is the definition of the response functions. It is redefined as

$$(4.117) \quad \chi_{0m,n0}^\Lambda = \frac{1}{\pi} \lim_{\eta \rightarrow 0} \text{Im} \int_{-\infty}^{\infty} dE G_{0m}^\Lambda(E + i\eta) G_{n0}^\Lambda(E + i\eta) f(E)$$

The non-zero electronic temperature  $T_e$  enters to the above scheme via the Fermi-Dirac function  $f(E)$  given by

$$(4.118) \quad f(E) = \frac{1}{1 + \exp[(E - E_F)/k_B T_e]}$$

with  $E_F$  being the Fermi energy and  $k_B$  the Boltzmann constant. Smearing of the Fermi level by the Fermi-Dirac function using a non-zero electronic temperature results in reducing the range of the density matrix (Stechel, Williams and Feibelman, 1994) which in turn means that fewer moments are needed for accurate evaluation of the local density of states.

For this approach to be valid, the energy of the thermal activation of the electrons, which is of the order of  $k_B T_e$ , has to be at least an order of magnitude less than the width of the band  $W$ , (Horsfield *et al.*, 1996), i.e.

$$(4.119) \quad \frac{k_B T_e}{W} \ll 1$$

Using a finite electronic temperature also means that instead of the total energy  $E(T)$  we have to deal with the free energy  $F(T) = E(T) - TS(T)$  where the additional entropic term (  $-TS(T)$  ) accounts for the fact that electrons with energies near the Fermi energy can be in different states. The electronic entropy is given by

$$(4.120) \quad S = 2 \sum_{i\alpha} \int d\varepsilon n_{i\alpha}(\varepsilon) \sigma[(\varepsilon - E_F)/k_B T_e]$$

where  $\sigma$  is the entropic density function

$$(4.121) \quad \sigma(x) = -k_B \{ f(x) \log[f(x)] + (1-f(x)) \log[1-f(x)] \}$$

with  $f(x) = 1/[1+\exp(x)]$ . The calculation of forces is formally not effected by the fictitious temperature and equation (4.40), used when evaluating forces, remains unchanged. This has been demonstrated by Horsfield and Bratkovsky 1996, who showed that provided the forces are evaluated at constant number of electrons per atom, the expression (4.40) already accounts correctly for the electronic entropy contribution.

## 5. TRANSFERABILITY OF THE HAMILTONIAN MATRIX

### ELEMENTS AND THE CAUCHY PRESSURES PROBLEM

Before proceeding to the actual construction of the Bond Order Potentials described in detail in Chapter 6, in this chapter we address some important issues relevant to the fitting of the potentials. The first part of this chapter comprises a study of the transferability of bonding integrals between different structural and compositional environments. This transferability is very important if the potentials are to be applied to a range of different atomic configurations that may be encountered, for example, when dealing with extended defects, such as dislocations or interfaces. In the second part of this chapter we will address the problem associated with fitting of the Cauchy pressures and describe how we deal with it. The ab-initio studies, results of which we will be using in the following, were performed by our collaborators at the University of Oxford, Dr. Duc Nguyen-Manh and Professor D.G. Pettifor.

#### 5.1. The Hamiltonian Matrix Elements and their Transferability

The off-diagonal Hamiltonian matrix elements  $H_{i\alpha,j\beta}$  ( $i \neq j$ ) are in the following referred to as the bonding integrals. As mentioned in the previous chapter, in BOPs they are determined within the orthogonal two-center approximation. However, when a more general non-orthogonal basis set is introduced within the tight binding method, the overlap matrix,  $S_{i\alpha,j\beta}$ , and three-center integrals interject an environmental dependence

that is neglected in this approximation (Nguyen-Manh *et al.*, 2000). Hence, the transferability of the bonding integrals based on the orthogonal basis set to different environments may be limited and needs to be thoroughly investigated.

To include different kind of species present in Ti-Al alloys we will employ a new notation for labeling the Hamiltonian matrix elements  $H_{I,J}$  that uses vector indices  $I \equiv [i, L_i, s_i]$  and  $J \equiv [j, L_j, s_j]$ . The  $i$  and  $j$  number the atomic sites,  $L_i$  and  $L_j$  types of atomic orbitals, and indices  $s_i$  and  $s_j$  denote different kinds of species.

The first important approximation is that in BOPs we use a limited set of orbitals in the tight-binding scheme. Specifically, in the case of TiAl we have included only  $d$  orbitals centered on Ti and only p-orbitals centered on Al atoms. We can use only a small number of orbitals because all the important covalency effects in this material arise from the  $p$ - $d$  and  $d$ - $d$  bonding (see for example Pettifor, 1995). Including smaller number of orbitals also reduces the computational effort and thus the time of the calculation. The validity of this approximation was tested by comparing electronic densities of states (DOS) calculated in this tight-binding  $p$ - $d$  approximation with those evaluated using the ab-initio all electron tight-binding LMTO method (Andersen *et al.*, 1985). The results are shown in Figure 5.1. This test demonstrates that for TiAl with  $L1_0$  structure all the important features of the DOS are well reproduced within the  $p$ - $d$  approximation (Nguyen-Manh *et al.*, 2000).

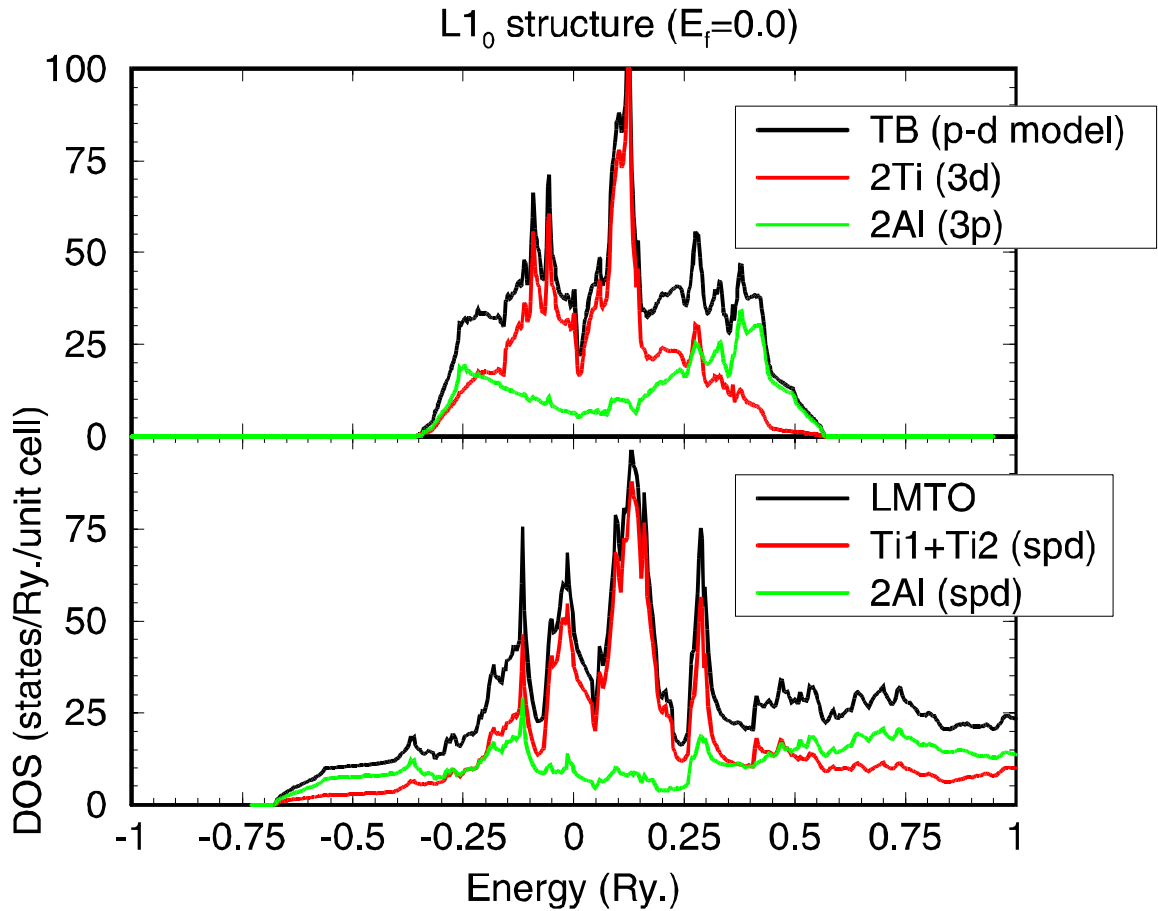


Figure 5.1 Electronic density of states of TiAl. Comparison of the full ab-initio (TB-LMTO) and the p-d TB model.

In order to investigate the transferability of the bond integrals and to determine their functional forms,  $H_{i,j}$  need to be evaluated as functions of the separation of atoms  $i$  and  $j$  for various structures using an ab-initio technique. Such technique must employ a small, single-electron basis of atom-centered, short-range orbitals and the Hamiltonian must have a simple analytical form that relates to a two-center, orthogonal tight-binding Hamiltonian so that a direct link with the tight-binding method can be established. The first-principles TB-LMTO (Andersen and Jepsen 1984 ; Andersen *et al.* 1985) is such

method. In this method the minimal basis of muffin-tin orbitals is transformed in the two-center approximation exactly into a localized basis with at most one *s*-type, three *p*-type and five *d*-type orbitals per atom. The TB-LMTO Hamiltonian may be expressed in the orthonormal representation as a power series in the two-center tight-binding Hamiltonian

$$(5.1) \quad H_{I,J}^\alpha \equiv (c_I^\alpha - E_{vl})\delta_{I,J} + \sqrt{d_I^\alpha} S_{I,J}^\alpha \sqrt{d_J^\alpha}$$

where the superscript  $\alpha$  denotes that the Hamiltonian is constructed using the screened structure constants  $S_{I,J}^\alpha$ . These are determined solely by the positions of the atoms in the system studied. They are given in terms of the conventional canonical structure constants  $S_{I,J}^0$  by the matrix equation (Andersen *et al.* 1985, Andersen *et al.* 1994)

$$(5.2) \quad S^\alpha = S^0 (1 - \alpha S^0)^{-1}$$

where  $\alpha$  is a diagonal matrix with elements  $\alpha_{I,J} = \alpha_i \delta_{i,j} \delta_{L_i, L_j}$  that characterizes the corresponding LMTO representation (Andersen and Jepsen 1984 ; Andersen *et al.* 1985).  $E_{vl}$  are the energy expansion parameters taken in the center of the occupied part of the  $L_i$  projected valence density of states (Skriver 1984). Coefficients  $(c_I^\alpha - E_{vl})$  and  $d_I^\alpha$  can be obtained from the self-consistent LMTO potential parameters  $c_I^\gamma$ ,  $d_I^\gamma$  and  $\gamma_I$  that are tabulated (Andersen *et al.* 1985) using the expression (Nowak *et al.* 1991)

$$(5.3) \quad \frac{c_I^\alpha - E_{vl}}{c_I^\gamma - E_{vl}} = \left( \frac{d_I^\alpha}{d_I^\gamma} \right)^{1/2} = 1 + \frac{\alpha_I - \gamma_I}{d_I^\gamma} (c_I^\gamma - E_{vl})$$

The optimum values of  $\alpha_s$  that yield most localized orbitals are  $\alpha_s = 0.3546$ ,  $\alpha_p = 0.0530$  and  $\alpha_s = 0.0170$  (Nowak *et al.* 1991).

Owing to the short-range character of the screened structure constants the second term in (5.1) gives for  $i \neq j$  the effective bond integrals. However, it should be noted that the reduction of  $S_{I,J}^\alpha$  to axially symmetric two-center integrals  $\sigma$ ,  $\pi$  and  $\delta$  states (for the direction  $(\mathbf{R}_i - \mathbf{R}_j)$  connecting the two atoms chosen as the z axis of the coordinate system) is no longer exact. The reason is that the screened structure matrix, unlike the canonical one, generally has lower than spherical symmetry ( $L=l,m$ ) because of its dependence on the local environment. Hence, the resulting bonding integrals  $H_{I,J}$  are, in general, environmentally dependent.

In order to investigate the bonding integrals employed in BOP for Ti-Al alloys, their dependence on the separation of atoms was calculated using equations (5.1), (5.2) and (5.3) for  $L1_0$  TiAl,  $DO_{19}$   $Ti_3Al$ , as well as for hcp Ti and fcc Al. This was achieved by evaluating the integrals in each case for several volumes per atom. The employment of different structures and compositions allows us to investigate possible environmental dependence of these integrals. The results of these calculations are presented in Figure 5.2. They show excellent transferability between different structures and compositions for all the bonding integrals used:  $dd\sigma$ ,  $dd\pi$  and  $dd\delta$  for Ti-Ti bonding (  $dd\delta$  is not included in Figure 5.2 but displays the same behavior),  $pp\sigma$  and  $pp\pi$  for Al-Al bonding, and  $dp\sigma$  and  $dp\pi$  for Ti-Al bonding. This finding affirms that the bonding integrals can be represented by functions of the separation of atoms and possible environmental

dependence is not significant. The corresponding analytical functions used for these integrals in the framework of BOP will be given in the following chapter.

A salient feature of the Ti-Al alloys, as well as pure Ti and pure Al, is that their structures are close packed and thus the second nearest neighbor spacing is much larger than that of the first nearest neighbors. Hence, owing to the short-range nature of the screened structure matrix, all the bonding integrals are almost negligible at second nearest neighbors.

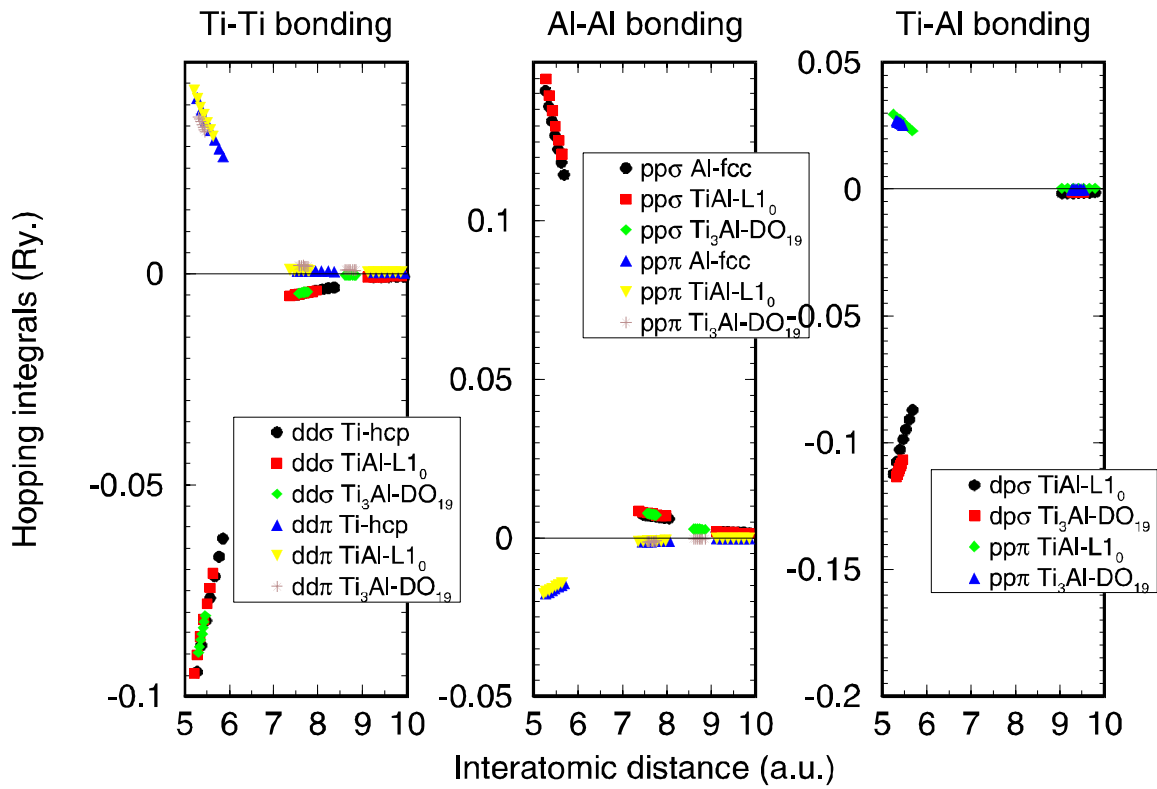


Figure 5.2 Bonding integrals in Ti-Al alloys calculated using TB-LMTO as a function of the separation of atoms.

## 5.2. The Problem of Negative Cauchy Pressures and the Environment-Dependent Term

For many intermetallic compounds elastic constants exhibit a peculiar property - negative Cauchy pressures. This is also the case for titanium-aluminum alloys. In the tetragonal structure the two Cauchy pressures are  $C_{13}-C_{44}$  and  $C_{12}-C_{66}$ , respectively. For comparison, in the simpler case of the cubic structure there is only one Cauchy pressure,  $C_{12}-C_{44}$ . The name pressure has its roots in the fact that if the total energy is a sum of a pair-potential and a density dependent term, i.e.  $E = 1/2 \sum_{i,j}^N \Phi(R_{ij}) + U(V)$ , the quantity  $C_{12}-C_{44}$  is in equilibrium related to the pressure  $P$  arising from  $U(V)$  (\_ob and Vitek, 1996, Girshick *et al.* 1997). In the cubic case

$$(5.4) \quad C_{12} - C_{44} = 2 \left( \frac{dU}{dV} \right) + V \left( \frac{d^2U}{dV^2} \right)$$

If  $\left( \frac{d^2U}{dV^2} \right)$  is small then  $\left( \frac{dU}{dV} \right) \equiv P$  arising from  $U(V)$ .

In the case of the tetragonal L1<sub>0</sub> TiAl the two Cauchy pressures are negative with values  $C_{13}-C_{44} = -34.2 \text{ GPa}$  and  $C_{12}-C_{66} = -6.4 \text{ GPa}$  (Tanaka *et al.* 1996). From the point of view of the modeling of the material this is a rather important circumstance since some of the widely used empirical schemes are unable to reproduce this result. It is well known that any purely pair-potential scheme gives a zero contribution to the Cauchy pressures for structures in equilibrium (\_ob and Vitek 1996, Girshick *et al.* 1998). More elaborate many-body central-force schemes, describing atoms as embedded in the electron gas of

the surrounding neighbors, on the other hand always give a positive value of the Cauchy pressures for the equilibrium state. The total energy in these schemes consists of a pair potential and an embedding term. The contribution of the pair potential is zero, thus the Cauchy pressures are determined by the embedding term. Due to the functional form of the embedding function (square root or similar form) the contribution of the embedding part is positive. This is the case of the embedded atom method (EAM) and the Finnis-Sinclair (FS) potential (Daw and Baskes 1984; Finnis and Sinclair 1984) that proved so valuable in describing materials with predominantly metallic character of bonding. All such potentials, as is the case of the EAM potentials of Simmons, Rao and Dimiduk (1993), the EAM potential used by Panova and Farkas (1995), and also the FS potential developed by Girshick *et al.* (1995), lead to positive Cauchy pressures for L1<sub>0</sub> TiAl.

Since the reason for the negative Cauchy pressures seemed to be the partially covalent character of bonding in TiAl, the shortcoming of these potentials was expected to be overcome simply by using a more sophisticated method that accounts for the directional bonding, such as tight-binding (TB). This assumption, however, proved false. The equilibrium contribution of the pair potential to the Cauchy pressures is zero, thus if no additional term is used in the TB, the Cauchy pressures are determined purely by the bond part (see (4.29) in Chapter 4). The contribution of the bond part however - as has been demonstrated by Nguyen-Manh *et al.* 1998 - fails to reproduce the negative Cauchy pressures and renders only positive contributions regardless of the choice of fitting parameters. To track down the real physical reason behind the negative Cauchy pressures Nguyen-Manh (1998) carried out a detailed ab-initio study analyzing contributions to the

Cauchy pressures arising from different terms of the Hamiltonian in the Harris-Foulkes approximation to the density functional theory (see equation (4.13) in Chapter 4). In his study he used the full potential linear muffin tin orbital (FP-LMTO) method (Methfessel 1988). He found that the inability of the TB method to reproduce the negative Cauchy pressures is caused by neglecting the environmental dependence in both the bond part and the short-term repulsion. In TiAl the environmental screening effects are most profound in the case of the *s* and *p* orbital overlap repulsion, since these orbitals are being squeezed in the core region under the strong influence of unsaturated covalent *d* bonds (Nguyen-Manh *et al.* 1998). A simple pair-potential is unsuitable for describing these screened repulsive interaction and should be supplemented by a term capable to capture these effects. Based on this analysis it was proposed that the short-range part of this repulsion by the orbitals on atoms *i* and *j* can be approximated by a screened Yukawa-type potential

$$(5.5) \quad \Phi(\lambda_{ij}, R_{ij}, R_c) = \frac{A}{R_{ij}} \exp[-(\lambda_i + \lambda_j)(R_{ij} - 2R_c)]$$

with the environmental dependence entering via the screening parameter  $\lambda_i$  given by

$$(5.6) \quad \lambda_i = \lambda_0^i + \left[ \sum_{k \neq i} C_k \exp(-v_k R_{ik}) \right]^{\nu_m}$$

This environment-dependent term has then been used to supplement the bond part and the pair potential in our computational scheme. If fitted, it can provide for the needed negative contribution to the total Cauchy pressures. The fitting procedure will be described in detail in the following Chapter.

## 6. CONSTRUCTION OF BOPs FOR Ti AND TiAl

This chapter gives a detailed account of the construction of Bond Order Potentials for pure Ti and TiAl. Since BOP is a semi-empirical method, the potentials contain parameters that are fitted to a variety of equilibrium properties. Still, it is important to note that the number of empirical data used is relatively small (eight in the case of Ti and nine for TiAl). The development of the BOP for hcp Ti was carried out analogously as in the previous study of Girshick (1997). The main difference, when compared with the older version, is the exact fitting of the Cauchy pressures. This is achieved by including the environment-dependent repulsive term, discussed in Chapter 5. The situation is more complex in the case of TiAl since two types of species are present. Three kinds of interactions need to be considered in the alloy - Ti-Ti, Al-Al and Ti-Al - and to simplify the fitting procedure we used the BOP for hcp Ti as the base for the Ti-Ti interaction in the alloy. Thus we were left with fitting only the Al-Al and Ti-Al parts of the potentials.

In the framework of the Bond Order Potentials the energy of a system of atoms can be divided into three parts and can be written as

$$(6.1) \quad E_{coh} = E_{bond} + E_{pair} + E_{env}$$

where  $E_{bond}$  and  $E_{pair}$  are the bond energy and the repulsive energy described by pair interactions, respectively (see equation (4.27)).  $E_{env}$  is the environment-dependent many-body repulsive contribution which allows us to fit the Cauchy pressures; its physical

justification has been discussed in the previous Chapter.  $E_{pair} = \frac{1}{2} \sum_{i \neq j} V^{s_i, s_j}(R_{i,j})$  represents

the electrostatic interaction between the atoms and overlap repulsion of  $d$  or  $p$  electrons.

It is principally repulsive and described by pair-potential the functional form of which is

a sum of cubic splines that extends up to the cut-off  $R_1^{s_i, s_j}$ :

$$(6.2) \quad V^{s_i, s_j}(R_{i,j}) = \sum_k A_k^{s_i, s_j} (R_k^{s_i, s_j} - R_{ij})^3 H(R_k^{s_i, s_j} - R_{ij})$$

where  $H(x)$  is the Heaviside step function,  $R_{i,j}$  is the separation of interacting atoms  $i$  and  $j$ . Indices  $s_i$  and  $s_j$ , mark the type of species at the sites  $i$  and  $j$ , respectively. The node points of the splines  $R_k^{s_i, s_j}$ , and the coefficients  $A_k^{s_i, s_j}$ , are used as fitting parameters as described in section 6.1.3. This functional form assures that  $V^{s_i, s_j}(R_{i,j})$  and its first and second derivatives are everywhere continuous and equal to zero at the cut-off; the same form was used in construction of many-body central force potentials of the Finnis-Sinclair type (Ackland *et al.* 1987).

As explained in the previous chapter, the environmentally dependent part of the energy,  $E_{env}$ , represents the overlap repulsion that arises from the valence  $s, p$  electrons. It is described by the repulsive central-force many-body potential

$$(6.3) \quad E_{env} = \frac{1}{2} \sum_{i \neq j} B^{s_i, s_j} \frac{\exp\left[-\frac{1}{2}(\lambda_i^{s_i} + \lambda_j^{s_j})(R_{ij} - 2R_c^{s_i, s_j})\right]}{R_{ij}}$$

with

$$\lambda_i^{s_i} = \lambda_0^{s_i} + \left[ \sum_{k \neq i} C^{s_i} \exp(-v^{s_i} R_{ik}) \right]^{1/m^{s_i}}$$

where  $B^{s_i, s_j}$ ,  $C^{s_i}$ ,  $v^{s_i}$ ,  $\lambda_0^{s_i}$ ,  $R_c^{s_i, s_j}$  and  $m^{s_i}$  are adjustable parameters, in general dependent

on the type of species,  $s_i$ .

$E_{bond}$  is the bond energy arising from the formation of the valence band that comprises terms dependent on bond angles. As discussed in chapter 5, in the present model this contribution originates from  $p$  electrons associated with Al and  $d$  electrons associated with Ti; their hybridization is also included. Within the BOP

$$(6.4) \quad E_{bond} = \sum_{\substack{I,J \\ i \neq j}} H_{I,J} \Theta_{J,I}$$

where  $H_{I,J}$  and  $\Theta_{J,I}$  are the Hamiltonian and the bond order matrix elements, respectively. The index  $I \equiv [i, L_i, s_i]$ , where  $i$  numbers the atomic sites in the system studied,  $L_i = (l, m)_i$  denotes the quantum orbital moment and quantum magnetic moment for spherical symmetry and  $s_i$  again marks the type of species at the site  $i$ . The most important quantities entering the bond energy are the bond integrals  $H_{I,J}$  ( $i \neq j$ ); the on site Hamiltonian elements are determined by the condition of charge neutrality (see section 4.1). The magnitudes and functional forms of the bond integrals were determined on the basis of ab-initio, calculations described in the previous chapter. Additional parameters that need to be chosen when evaluating the bond energy are the number of electrons in the band considered and the effective electronic temperature  $T_e$  (see section 4.6).

An important feature of the fitting is that it is sequential in that each part of the BOPs is fitted independently. First  $E_{bond}$  is built based on ab-initio data with no empirical input. Next  $E_{env}$  is constructed by fitting the Cauchy pressures and, finally the pair

potential is fitted so as to reproduce several equilibrium properties, namely lattice parameters, remaining elastic moduli and the cohesive energy.

### 6.1. Bond Order Potentials for hcp Ti

Our BOP for pure hcp Ti is a new version of the potentials originally developed by A.Girshick (Girshick *et al.* 1997, Girshick 1997) which were successful in studies of dislocations in pure Ti. The only notable shortcoming of these potentials was their inability to reproduce accurately the Cauchy pressures, in spite of the fact that they are both positive in Ti. Since the environmentally dependent repulsion was not part of the old scheme only the bond part contributed to the Cauchy pressures and by adjusting the bond part only, the two Cauchy pressures could not be fitted at the same time (Girshick 1997). Inclusion of the environmentally dependent repulsion,  $E_{env}$  into the BOP scheme solved this problem.

Another major difference between the two versions of potentials is that while in the old scheme ratios of bond integrals were taken as in the canonical band theory (Andersen 1975), the new potentials use values found from the ab-initio calculations described in the previous chapter. As already mentioned, each part of the potentials was fitted independently in a sequential manner. Details of the fitting are given in the following sections.

### 6.1.1. Construction of the Bond Part of BOPs for hcp Ti

The bond part, built first in the sequential fitting, is the most important component of the BOP since it captures the cohesion arising from the formation of bonds that may have a covalent character. Since Ti is a transition metal with unfilled *d*-band (the electronic structure of Ti atoms is  $3d^24s^2$ ) its bonding exhibits significant covalent character and it is the bonding part that provides description of this directional bonding. In both hcp Ti and TiAl only d-electrons associated with Ti are considered in the bond part. This approximation has been discussed in the previous Chapter. That leaves us with only three bond integrals to be fitted:  $dd\sigma$ ,  $dd\pi$  and  $dd\delta$ . The presence of *s*-electrons is not, of course, completely neglected but in this scheme they are included in the environmentally dependent repulsion and in the interaction described by the pair potential. Apart from the three bond integrals we also have to choose the number of valence *d*-electrons,  $N_d$ , and the electron temperature  $T_e$  when evaluating the bond energy.

In any tight-binding scheme bond integrals can be separated into a radial part and an angular part and the latter has been tabulated for s, p and d symmetries by Slater and Koster (1954). What then remains to be determined is the radial part and its scaling, i. e. the dependence on separation of atoms. In this thesis the radial part was determined by fitting the ab-initio calculations of D. Nguyen-Manh (see chapter 5, Figure 5.2). These provide guidelines for both the values and functional forms of bond integrals. We used the following simple power law to represent the distance dependence (i. e. scaling) of the radial part of the bond integrals

$$(6.5) \quad dd\alpha(R) = dd\alpha_0 \left( \frac{R_0}{R} \right)^n$$

where  $\alpha = \sigma, \pi$  or  $\delta$ ,  $dd\alpha_0 = dd\alpha(R_0)$ , and  $R_0$  is the nearest neighbor spacing in the close-packed basal plane (2.950 Å for hcp titanium). The ab-initio calculations provided us with  $dd\sigma_0$ ,  $dd\pi_0$  and  $dd\delta_0$ , i.e. the magnitudes of the hopping integrals at the distance equal to the nearest neighbor spacing,  $R_0$ . The numerical values are  $dd\sigma_0 = -1.1526$  eV,  $dd\pi_0 = 0.5284$  eV and  $dd\delta_0 = -0.0622$  eV. When developing the earlier version of BOP for pure Ti (Girshick *et al.* 1997, Girshick 1997) the ab-initio data had not been available and the prefactors  $dd\sigma_0$ ,  $dd\pi_0$ ,  $dd\delta_0$  had been fitted to reproduce the correct width of the d-band while keeping their ratios fixed in accordance with the canonical band theory (Andersen 1975).

The remaining parameters, the scaling exponent  $n$  from equation (6.5) and the number of electrons in the d-band (i.e. d-band filling),  $N_d$ , were adjusted so as to assure the correct difference between energies of two competing close-packed structures: hcp and fcc. It must be emphasized at this point that for the same atomic volume, separations of the first and second nearest neighbors are the same in fcc and hcp structures. Thus, up to the second nearest neighbors, the structures differ only by bond angles. Hence, the environmentally dependent term and the pair potential, which are both central-force terms, can differentiate between these two structures only by contributions arising from third and other more distant neighbors. These contributions cannot be large and may only provide sufficient energetic preference for one or the other close-packed structure in

materials in which the difference between hcp and fcc structures is small; these are materials with low stacking fault energy. However, in Ti in which the stacking fault energy is very high, the energy difference between the two close packed structures is large,  $\Delta E_{ref}^{fcc-hcp} = 58 \text{ meV / atom}$  according to the ab-initio (FP-LAPW) calculations of M. \_ob (private communication). This large difference certainly arises from angularly dependent contributions, i. e. from the covalent character of bonding. Since only the bond part is angularly dependent it is the bond energy that is the source of the preference for the hcp structure over the fcc structure.

For the bond part to differentiate correctly between the two closed-packed structures we must first ensure that sufficiently high number of recursion levels  $N_{rec}$  is used in the scheme (see chapter 4). This requires, as described for example in Pettifor 1995, that at least three recursion levels are included. In this case all recursion coefficients  $a_k, b_k$  in the bond order expansion (4.84) are calculated exactly up to  $k = 3$ . The number of exact recursion coefficients for a given recursion level is  $(2N_{rec}+1)$  and for the third level they are  $a_0, a_1, b_1, a_2, b_2, a_3$  and  $b_3$ . Guided by the previous version of the potentials, we decided to go one step above the minimal level needed and use  $N_{rec} = 4$ . This means that all moments of the density of states are exact up to the ninth.

The next step in ensuring the correct difference between energies of hcp and fcc structures is adjustment of the scaling parameter  $n$  and the number of electrons in the d-band,  $N_d$ . Since we are employing only the  $d$ -orbital model for the bond part, the correct energy difference is not attained automatically and fitting of these parameters is essential for the accuracy of the whole scheme. As suggested by the ab-initio data on Ti-Ti

hopping integrals (chapter 5, Figure 5.2), the scaling parameter  $n$  should lie in the range 3.6 to 3.9. By varying the scaling exponent  $n$  in this range and simultaneously changing the  $d$ -band occupancy parameter,  $N_d$ , we have adjusted the contribution of the bond part to yield the desired hcp-fcc energy difference. The final fitted values,  $n = 3.6$  and  $N_d = 2.2$ , yielded an adequate bond part contribution of  $\Delta E_{bond}^{fcc-hcp} = 52.5 \text{ meV / atom}$  which is sufficiently close to  $58 \text{ meV / atom}$ , found by ab-initio calculations (M.\_ob, private communication). The contribution arising from the central force parts of the potential turned out - as we expected - to be marginal; the pair potential and the environmentally dependent repulsive term contributed to this energy difference only  $2.7 \text{ meV / atom}$ .

The ab-initio study discussed in the previous chapter shows that the hopping integrals are relatively short-ranged (see Figure 5.2). They decrease rapidly with interatomic separation, and their values at the second nearest neighbors are much smaller than at the first nearest neighbors. Having this in mind, we cut off the bond integrals at  $R^{cut} = 4.8 \text{ \AA}$ , i.e. just beyond the third nearest neighbors. This is also important for the computational efficiency. A cut-off tail is then introduced by augmenting the power law function (6.5) with a polynomial of fifth order

(6.6)

$$P(R) = C_0 + (R - R^b) \left\{ C_1 + (R - R^b) \left[ C_2 + (R - R^b) \left( C_3 + (R - R^b) \left( C_4 + (R - R^b) \left( C_5 + (R - R^b) \right) \right) \right) \right] \right\}$$

starting at  $R^b = 3.1 \text{ \AA}$ . The coefficients of the polynomial are chosen so that the function, and its first and second derivatives are continuous at  $R^b = 3.1 \text{ \AA}$  (beyond the first neighbor distance) and zero for  $R^{cut} = 4.8 \text{ \AA}$  (beyond the third nearest neighbor distance). The

parameters of the cut-off tail are listed in Table 6.2. The resulting analytical forms of the radial part of bond integrals for  $dd\sigma$  and  $dd\pi$ , together with the corresponding ab-initio data (from Figure 5.2.), are shown in Figures 6.1 and Figure 6.2 respectively. The much weaker bond integral  $dd\delta$  displays similar behavior.

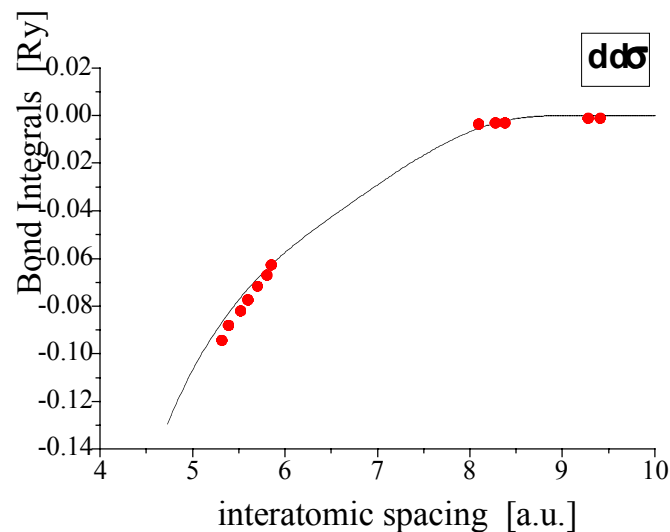


Figure 6.1 The radial part of the  $dd\sigma$  bond integral.

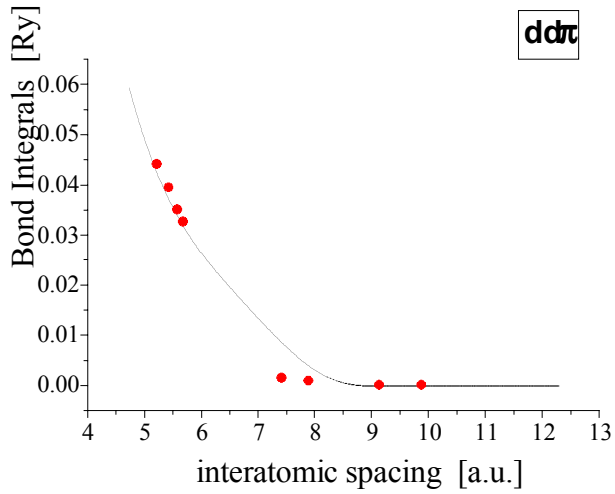


Figure 6.2 The radial part of the  $dd\pi$  bond integral

The fictitious effective electronic temperature  $T_e$ , introduced in order to dampen the long-range Friedel oscillations, as discussed in chapter 4, was chosen so as to ensure fast convergence of the real-space bond-order expansions. Precise calculation of bond-order parameter is a necessary precursor for the Hellmann-Feynman force expression (4.40) to apply. The effective temperature must be chosen sufficiently large to guarantee adequate precision of the calculated forces. But, at the same time, as follows from equation (4.119),  $k_B T_e$  must be much smaller than the width of the  $d$ -band  $W_d$ . In the previous version of BOPs for hcp Ti (Girshick 1997) these two constraints lead to  $k_B T_e = 0.3$  eV where  $k_B$  is the Boltzmann constant. This value of  $T_e$  was determined by requiring that analytically calculated forces, when compared to values obtained by numerical differentiation of the total energy, agreed to a precision better than

0.0004eV/Å. In our development of the potentials we kept  $k_B T_e = 0.3$  eV and the above mentioned testing showed that it yielded the same precision for calculation of forces.

Summary of all the parameters of the bond part is given in Table 6.1.

$R_0$	2.950 Å
$dd\sigma_0$	-1.1526 eV
$dd\pi_0$	0.5284 eV
$dd\delta_0$	-0.0622 eV
$N$	3.6
$N_d$	2.2
$N_{rec}$	4
$k_B T_e$	0.3 eV

Table 6.1 Parameters of the bond part for BOPs for hcp Ti

$R^b$	3.1 Å
-------	-------

$R^{cut}$	4.8 Å
$C_0$	0.8364830781555298
$C_1$	-0.9713997036644862
$C_2$	0.7207159091704253
$C_3$	-0.9576960587594398
$C_4$	0.6686722063916291
$C_5$	-0.1512567080872813

Table 6.2 The bond part cut-off polynomial tail parameters for BOPs for hcp Ti

### 6.1.2. Fitting of the Environmentally Dependent Repulsive Term

The purely repulsive environmentally dependent term given by equation (6.3) has been fitted while keeping all the parameters of the bond part fixed. As mentioned earlier, this term was not a part of the older version of BOPs for Ti but was introduced more recently to remedy the problem of fitting the Cauchy pressures. The experimental values of the two Cauchy pressures in hcp Ti are  $(C_{12}-C_{66})_{exp} = 0.261 \text{ eV}/\text{\AA}^3$  and  $(C_{13}-C_{44})_{exp} = 0.109 \text{ eV}/\text{\AA}^3$  (Simmons and Wang 1971). The environmentally dependent term is fitted in such a way as to compensate for the discrepancy between the desired values of the Cauchy pressures and the contribution from the bond part. First the equilibrium contribution of the bond part to Cauchy pressures is calculated. Then, by varying the parameters of the environmentally dependent term, we achieve a contribution that brings the total Cauchy pressures sufficiently close to experimental values. As discussed in chapter 5, the pair potential term does not contribute to Cauchy pressures and therefore

this fit is not affected by later inclusion of the pair potential.

Stresses  $\sigma_{\alpha\beta} = \sigma_{\alpha\beta}(E)$  and second-order elastic constants  $C_{\alpha\beta\gamma\delta} = C_{\alpha\beta\gamma\delta}(E)$  are complex functions of the total energy and the positions of atoms in the crystal

$$(6.7) \quad \sigma_{\alpha\beta}(E) = \frac{1}{\Omega} \sum_{\substack{i,k \\ k>i}} \frac{\partial E}{\partial R_{ik}^\alpha} R_{ik}^\beta$$

(6.8)

$$C_{\alpha\beta\gamma\delta}(E) = \frac{1}{4\Omega} \sum_{\substack{i,j,k,l \\ k>i, l>j}} \left( \frac{\partial^2 E}{\partial R_{ik}^\alpha \partial R_{jl}^\gamma} R_{ik}^\beta R_{jl}^\delta + \frac{\partial^2 E}{\partial R_{ik}^\beta \partial R_{jl}^\gamma} R_{ik}^\alpha R_{jl}^\delta + \frac{\partial^2 E}{\partial R_{ik}^\alpha \partial R_{jl}^\delta} R_{ik}^\beta R_{jl}^\gamma + \frac{\partial^2 E}{\partial R_{ik}^\beta \partial R_{jl}^\delta} R_{ik}^\alpha R_{jl}^\gamma \right)$$

where  $\Omega$  is the volume of the system. In the following we will be using contributions of different parts of the total energy  $E$  (i.e.  $E_{bond}$ ,  $E_{env}$  - see equation (6.1)) to the stresses and elastic constants. These quantities are defined in the following way:

$$(6.9) \quad (\sigma_{\alpha\beta})_{bond/env} \equiv \sigma_{\alpha\beta}(E_{bond/env})$$

and

$$(6.10) \quad (C_{\alpha\beta\gamma\delta})_{bond/env} \equiv C_{\alpha\beta\gamma\delta}(E_{bond/env})$$

In the present case the contributions arising from the bond part were  $(C_{12}-C_{66})_{bond} = 0.628 \text{ eV}/\text{\AA}^3$  and  $(C_{13}-C_{44})_{bond} = 0.538 \text{ eV}/\text{\AA}^3$ . These values were obtained by numerical differentiation of the bond energy in our simulation code. There are six adjustable parameters in the environmentally dependent term,  $B$ ,  $C$ ,  $v$ ,  $\lambda_0$ ,  $R_c$  and  $m$  (indices  $s_i$  and  $s_j$  denoting different kinds of species are omitted here because only one element is treated at this stage). Since we are fitting only two quantities there is a

substantial freedom of choice. To simplify the fitting we kept the exponent  $m$  and the core radius  $R_c$  fixed, putting  $m = 2$  and  $R_c = 1.1\text{\AA}$ . The dependence of the Cauchy pressures on the parameters  $C$ ,  $v$  and  $\lambda_0$  is complex and highly non-linear, but numerical evaluation of the contribution of the environmentally dependent term to the Cauchy pressures for a given set of parameters is straightforward and fast. This allowed us to use a simple approach of simultaneous variation of the three parameters  $C$ ,  $v$  and  $\lambda_0$  within given ranges while adjusting the prefactor  $B$  that controls the magnitude of the contribution. In this way we achieved to fit the Cauchy pressures to experimental values within about 10%:  $(C_{12}-C_{66})= 0.271 \text{ eV}/\text{\AA}^3$  and  $(C_{13}-C_{44})= 0.100 \text{ eV}/\text{\AA}^3$ . Since the experimental error may exceed 10 % this fit is sufficiently precise. The final values of the fitted parameters of the environmental term are listed in Table 6.3

B	183.0 eV
C	$175.0 \text{ \AA}^{-2}$
v	$1.90 \text{ \AA}^{-1}$
$\lambda_0$	$3.90 \text{ \AA}^{-1}$
$R_c$	$1.0 \text{ \AA}$
$m$	2.0

Table 6.3 Parameters of the environmentally dependent term for BOPs for hcp Ti

As in the case of the bond integrals, a smooth polynomial cut-off tail was introduced in the environmentally dependent term, namely in the expression for evaluating  $\lambda^{s_i}$  ( see

equation (6.3)). The exponential term  $[C^{s_i} \exp(-\nu^{s_i} R_{ik})]$  is augmented by a polynomial of fifth order

$$(6.11) \quad P(R) = C_5(R - R^{cut})^5 + C_4(R - R^{cut})^4 + C_3(R - R^{cut})^3$$

starting at  $R^b = 4.8 \text{ \AA}$  (beyond fourth nearest neighbors) and ending at  $R^{cut} = 5.4 \text{ \AA}$  (beyond fifth nearest neighbors). The coefficients of the polynomial  $C_5$ ,  $C_4$  and  $C_3$  are chosen so that the function, and its first and second derivatives are continuous at  $R = R^b$  and zero at  $R = R^{cut}$ . The parameters of the cut-off tail are listed in Table 6.4.

$R^b$	4.8 \AA
$R^{cut}$	5.4 \AA
$C_5$	-0.795594463095655
$C_4$	-1.229616885597365
$C_3$	-0.540034682670622

Table 6.4 Cut-off tail parameters used in the environmentally dependent term for BOPs for hcp Ti

### 6.1.3. Fitting of the Pair Potential of BOPs for hcp Ti

The pair potential is the last term to be determined in the sequential fitting scheme while the parameters of both the bond part and the environmentally dependent term are kept unchanged. The functional form of the pair potential is given by equation (6.2). In the older version of BOPs (Girshick 1997) this form was supplemented by a repulsive term for separations of atoms below the equilibrium nearest neighbor spacing (2.896 \AA).

This was needed to avoid collapse of the lattice driven by the bond part of the energy that converges to minus infinity as  $R$  approaches zero (see equation (6.5)). In the present case, however, the environmentally dependent term, which varies exponentially, provides sufficient repulsion to compensate the power law dependent attraction from the bond part.

The pair potential in equation (6.2) is written as a sum of cubic splines that extend up to the cut-off  $R_1$ , which lies between the fourth and fifth neighbors of the ideal hcp lattice.  $R_k$  are the node points of the splines and  $A_k$  numerical coefficients. We have again dropped the index  $s_i$  denoting different species when dealing with the element Ti. The functional form assures that  $V(R)$  and its first and second derivatives are everywhere continuous and equal to zero at the cut-off. The form of the pair potential is very flexible using  $R_k$  and  $A_k$  as fitting parameters. As will be seen in the next paragraph its linear dependence on coefficient  $A_k$  is very convenient and facilitates greatly the fitting procedure which was carried out in the following way.

Having fitted the two Cauchy pressures ( $C_{12}$  -  $C_{66}$ ,  $C_{13}$  -  $C_{44}$ ) we are still left with three independent elastic constants that need to be reproduced using the pair potential (there are five independent elastic constants in the hcp structure:  $C_{11}$ ,  $C_{12}$ ,  $C_{13}$ ,  $C_{33}$  and  $C_{44}$ ). At the same time we want to fit the experimental value of the cohesive energy,  $E_{coh}$ , and the equilibrium hcp lattice parameters ( $a$  and  $c$ ). Altogether we have six quantities to fit. For these we write the following six equations that have been used in the fitting procedure:

(6.12)

$$E_{coh}^{pair} = \frac{1}{2\Omega_0} \sum_i \sum_j V(R_{ij}) = E_{coh} - E_{coh}^{bond} - E_{coh}^{env}$$

$$(6.13) \quad \sigma_{11}^{pair} = \frac{1}{2\Omega_0} \sum_i \sum_j V'(R_{ij}) \frac{X_{ij}^2}{R_{ij}^2} = -\sigma_{11}^{bond} - \sigma_{11}^{env}$$

$$(6.14) \quad \sigma_{33}^{pair} = \frac{1}{2\Omega_0} \sum_i \sum_j V'(R_{ij}) \frac{Z_{ij}^2}{R_{ij}^2} = -\sigma_{33}^{bond} - \sigma_{33}^{env}$$

$$(6.15) \quad \frac{1}{2\Omega_0} \sum_i \sum_j \frac{\Psi(R_{ij}) X_{ij}^4}{R_{ij}^2} = C_{11} - C_{11}^{bond} - C_{11}^{env} + \sigma_{11}^{bond} + \sigma_{11}^{env}$$

$$(6.16) \quad \frac{1}{2\Omega_0} \sum_i \sum_j \frac{\Psi(R_{ij}) Z_{ij}^4}{R_{ij}^2} = C_{33} - C_{33}^{bond} - C_{33}^{env} + \sigma_{33}^{bond} + \sigma_{33}^{env}$$

$$(6.17) \quad \frac{1}{2\Omega_0} \sum_i \sum_j \frac{\Psi(R_{ij}) X_{ij}^2 Z_{ij}^2}{R_{ij}^2} = C_{44} - C_{44}^{bond} - C_{44}^{env} + \frac{1}{4} (\sigma_{11}^{bond} + \sigma_{33}^{bond} + \sigma_{11}^{env} + \sigma_{33}^{env})$$

where separations  $R_{ij}$  correspond to those in the ideal hcp lattice with equilibrium lattice parameters  $a, c$ . The values of  $\sigma_{ij}^{bond/env}$  and  $C_{ij}^{bond/env}$  are obtained by numerical differentiation of the corresponding energy terms in the code (remember that the bond part and the environmentally dependent term are already determined). Quantities without superscripts are experimental values that are to be reproduced. The summation over  $i$  extends over the atoms in the unit cell; summation over  $j$  includes all the atoms interacting with the atom  $i$ .  $\Omega_0$  is the equilibrium volume of the unit cell.  $R_{ij}$  is the

distance between atoms  $i$  and  $j$ ,  $X_{ij}$  and  $Z_{ij}$  are the  $x$  and  $z$  components of the vector  $\mathbf{R}_{ij}$ , respectively. The function  $\Psi(R)$  is defined as

$$(6.18) \quad \Psi(R) = V''(R) - V'(R)/R$$

The first equation in this set, (6.12), serves for fitting the cohesive energy  $E_{coh}$ . The next two equations, (6.13) and (6.14), are used for fitting the lattice parameters. They restate the condition that for the equilibrium lattice parameters,  $a$  and  $c$ , the diagonal stress components in the  $x$  and  $z$  directions, i.e.  $\sigma_{11}$  and  $\sigma_{33}$ , are zero. The last three equations (6.15), (6.16) and (6.17) determine the elastic moduli  $C_{11}$ ,  $C_{33}$  and  $C_{44}$  (Girshick 1997).

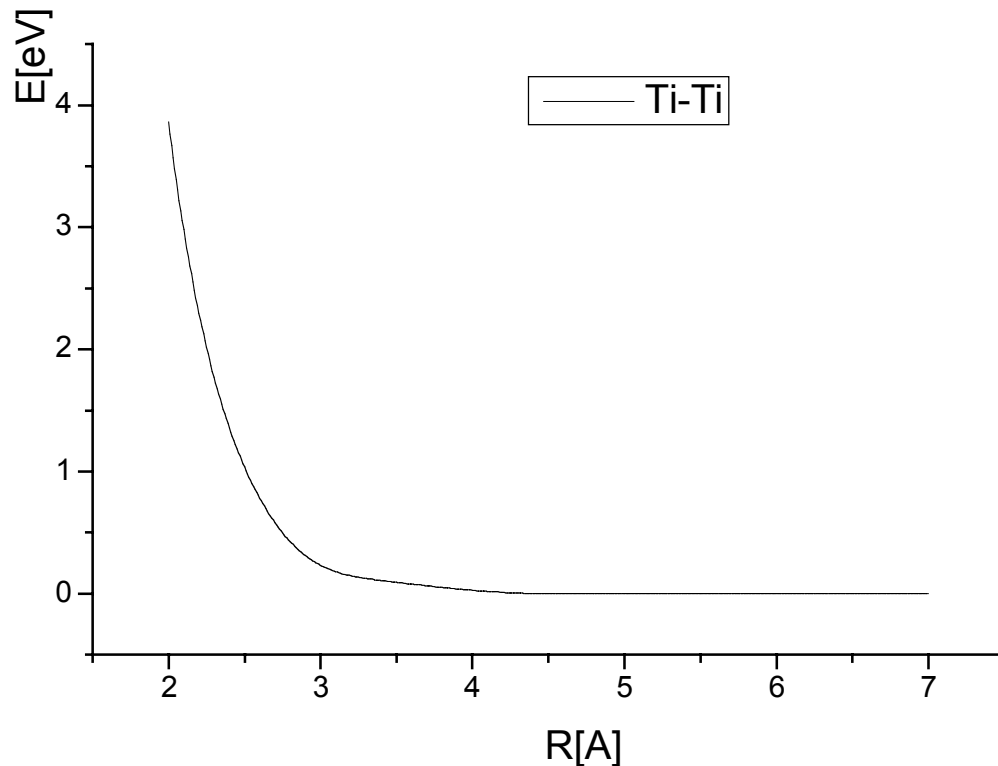


Figure 6.3 The Ti-Ti pair potential.

It is important to note that in the above equations the contribution of the pair potential (entering via  $V(R)$  or  $\Psi(R)$ ) to all the fitted properties is linear with respect to the spline coefficients  $A_k$ . This enables us to determine these coefficients by solving a set of linear equations. Since the pair potential is fitted last, the parameters of the other terms have already been fixed, and the contributions from the bond part and the environmentally dependent term, entering equations (6.12)-(6.17), are known. Equations (6.12) - (6.17) thus become a set of six linear equations for the spline coefficients  $A_k$  for the chosen node points  $R_k$ . The fitting procedure then proceeds by adjusting the positions of the node points  $R_k$  and subsequent evaluation of the coefficients  $A_k$ . The node points  $R_k$  are varied until a smooth and physically meaningful shape of the pair potential, i.e. repulsive at small separations and approaching zero at large separations, is obtained. The values of the node points  $R_k$  and coefficients  $A_k$  are summarized in Table 6.5. The resulting pair potential is shown in Figure 6.3.

A comparison of experimental values of the cohesive energy, lattice parameters and elastic moduli with those corresponding to the present potential is shown in Table 6.6. As can be seen, the quantities which the pair potential was fitted to are reproduced exactly. The elastic constants which were not fitted by the pair potential ( $C_{12}$ ,  $C_{13}$  and  $C_{66} = (C_{11} - C_{12})/2$ ) are also reproduced very well; the small disparity is related to the fact that the Cauchy pressures were not fitted exactly by the environmentally dependent term.

$i$	$A_i$	$R_i$
1	-17.54485126799736	4.80
2	30.61566487747791	4.75
3	-10.99281312350478	4.70
4	-19.40798869407337	4.25
5	17.56880739523064	4.20
6	1.06358595447043	3.30

Table 6.5. Parameters of the pair potential in the bond-order potential scheme for Ti. Parameters

$a_i$  - in units of eV/ $\text{\AA}^3$ ,  $r_i$  - in units of  $\text{\AA}$

	Current work	Experiment
$E_{coh}$	-4.850	-4.850
$a$	2.950	2.950
$c$	4.683	4.683
$c/a$	1.587	1.587
$C_{11}$	1.100	1.099
$C_{33}$	1.189	1.189
$C_{12}$	0.544	0.542
$C_{13}$	0.416	0.426
$C_{44}$	0.317	0.317
$C_{66}$	0.273	0.281

Table 6.6 Fitted equilibrium properties of hcp Ti calculated using the bond-order potentials

compared with the corresponding experimental values.  $E_{coh}$  (in eV) has been taken from Kittel 1986, lattice parameters  $a$  and  $c$  (in Å) - from Pearson 1967, elastic moduli (in eV/Å<sup>3</sup>) - from Simmons and Wang 1971.

## 6.2. Bond Order Potentials for TiAl

Having constructed BOP for hcp Ti we now proceed to the more complex task of development of BOP for TiAl which is the main goal of this work. The presence of the two species brings about not only an increased number of parameters but complicates the fitting as a whole due to the necessity to deal with three kinds of interactions, i.e. between Ti-Ti, Al-Al and Ti-Al atoms. To simplify the fitting procedure, we based the Ti-Ti interaction on the potential for pure hcp Ti **though some adjustments were necessary as will be explained later**. Thus we are left with fitting the Al-Al interaction and Ti-Al interaction. We further simplified the fitting of the Ti-Al cross-term by using geometric or arithmetic means of elemental parameters where applicable.

### 6.2.1. Construction of the Bond Part of BOPs for TiAl

As in the case of BOP for Ti the bond part is fitted first. In the framework of the *p-d* model, introduced in chapter 5, only *d* orbitals are considered for Ti atoms and *p* orbitals for Al atoms. That leaves us with 7 bond integrals to be fitted, namely  $dd\sigma$ ,  $dd\pi$ ,  $dd\delta$ ,  $pp\sigma$ ,  $pp\pi$ ,  $pd\sigma$  and  $pd\pi$ . As in the case of BOP for hcp Ti, the angular part of

the bond integrals is given by Slater-Koster formulas and we only need to fit the radial part. The three bond integrals,  $dd\sigma(R)$ ,  $dd\pi(R)$  and  $dd\delta(R)$ , involved in the Ti-Ti interaction were taken to be the same as in the potentials for hcp Ti. The radial parts,  $pp\sigma(R)$ ,  $pp\pi(R)$ ,  $pd\sigma(R)$  and  $pd\pi(R)$ , were again fitted to ab-initio data (chapter 5, Figure 5.2) using the same power law dependence as in the case of Ti

$$(6.19) \quad pp\alpha(R) = pp\alpha_0 \left( \frac{R_0^{Al-Al}}{R} \right)^{n_{pp}} \quad \text{and} \quad pd\alpha(R) = pd\alpha_0 \left( \frac{R_0^{Al-Ti}}{R} \right)^{n_{pd}}$$

where  $\alpha$  denotes the type of bonding,  $\sigma$ ,  $\pi$  or  $\delta$ ,  $R_0^{Al-Al}$  and  $R_0^{Al-Ti}$  are the nearest aluminum - aluminum and aluminum-titanium spacings in TiAl, taken as 2.8320 Å and 2.8547 Å, respectively. Values of coefficients  $pp\alpha_0$  and  $pd\alpha_0$  were determined from the results of ab-initio calculation and they are:  $pp\sigma_0 = 1.8986$  eV,  $pp\pi_0 = -0.2255$  eV,  $pd\sigma_0 = -1.3970$  eV,  $pd\pi_0 = 0.3748$  eV. The number of recursion levels  $N_{rec}$ , the electronic temperature  $T_e$ , and the  $d$ -band occupancy  $N_d$  were kept the same as in the potentials for Ti, namely  $N_{rec} = 4$ ,  $k_B T_e = 0.3$  and  $N_d = 2.0$ . Thus the only parameters fitted in the bond part of the energy are the two scaling exponents,  $n_{pp}$  and  $n_{pd}$  in equation (6.19), and the  $p$ -band occupancy (Al atoms)  $N_p$ . Similarly as in the case of hcp Ti, these parameters were adjusted to assure correct ordering of the two competing close-packed type structures, the equilibrium fcc-based tetragonal L1<sub>0</sub> and the hexagonal B19 structure (see Chapter 2). Since we use for the bonding part only  $p$  and  $d$ -orbitals, the correct preference may not result automatically and fitting of these parameters is essential for the accuracy of the whole scheme. The ab-initio calculations suggest values of  $n_{pp} \approx 2.8$  and

$n_{pd} \approx 3.2$  (see chapter 5, Figure 5.2). However, it turns out that for these values the bond part prefers incorrectly the B19 structure over the L<sub>1</sub><sub>0</sub> structure. Moreover, the unit cell of the B19 structure, unlike the L<sub>1</sub><sub>0</sub>, is not centrosymmetric which means that internal relaxation leading to further enhancement of this wrong preference may occur. As in the case of the potentials for hcp Ti we want the bond part to be the decisive factor when differentiating between competing close-packed structures. Therefore, we seek values of  $n_{pp}$ ,  $n_{pd}$  and  $N_p$  such that the correct equilibrium structure is favored and yet they remain physically reasonable. By testing a broad variety of combinations of these parameters we found that for  $n_{pp} \approx 3.4$ ,  $n_{pd} \approx 2.7$  and  $N_p = 2.9$  the L<sub>1</sub><sub>0</sub> is preferred over unrelaxed B19 (at this point we could not relax this structures) by  $\Delta E_{unrel}^{B19-L1_0} = 83 \text{ meV / atom}$ . This difference is then sufficient because when adding the other parts of the potentials, and finally fully relaxing the B19 structure, the preference for L<sub>1</sub><sub>0</sub> is  $\Delta E_{rel}^{B19-L1_0} = 35.9 \text{ meV / atom}$ . This is very close to the value found for the fully relaxed B19 structure in ab-initio CASTEP calculations, 32meV/atom (N. D. Manh, private communication).

As in the case of potentials for Ti, we also used a polynomial cut-off tail to limit the range of the bond integrals by augmenting them with polynomials of fifth order (6.6). The coefficients of these polynomials are again chosen so as to ensure that the functions and their first and second derivatives are continuous at the start of the cut-off  $R^b$  (beyond the first neighbor distance) and zero for  $R^{cut}$  (beyond the second nearest neighbor distance). The parameters of the cut-off are listed in Table 6.8. The final shapes of the radial part of the hopping integrals are shown in Figure 6.4 – 6.7. Summary of

the parameters of the bond part can be found in Table 6.7.

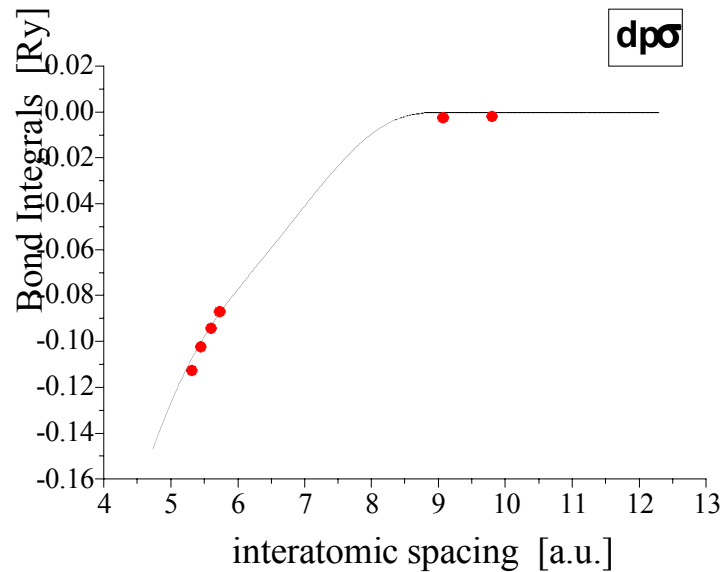


Figure 6.4 The radial part of the  $dp\sigma$  bond integral.

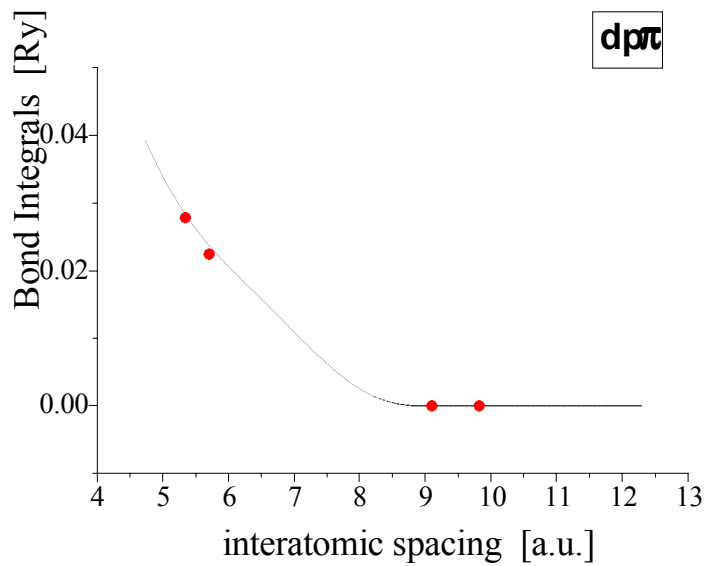


Figure 6.5 The radial part of the  $d\pi$  bond integral.

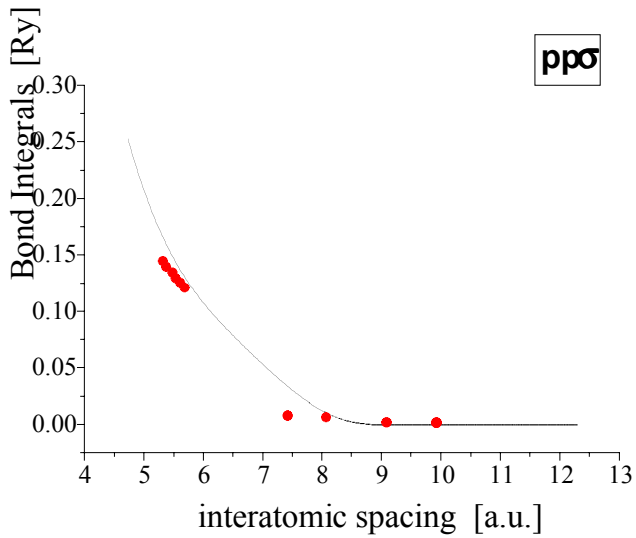


Figure 6.6 The radial part of the  $pp\sigma$  bond integral.

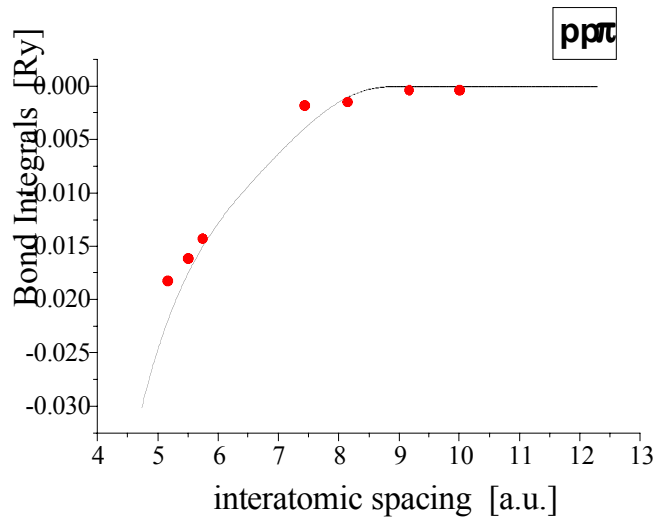


Figure 6.7 The radial part of the  $pp\pi$  bond integral.

	<b>Al-Al</b>	<b>Ti-Al</b>	<b>Ti-Ti</b>
$R_0$	2.8320 Å	2.8547 Å	2.950 Å
$n$	3.4	2.7	3.6
$k_B T_e$	0.3 eV	0.3 eV	0.3 eV
$N_{rec}$	4	4	4
	$N_p = 2.9$	-	$N_d = 2.2$
	$pp\sigma_0 = 1.8986$ eV	$pd\sigma_0 = -1.3970$ eV,	$dd\sigma_0 = -1.1526$ eV
	$pp\pi_0 = -0.2255$ eV	$pd\pi_0 = 0.3748$ eV	$dd\pi_0 = 0.5284$ eV
	-	-	$dd\delta_0 = -0.0622$ eV

Table 6.7 Parameters of the bond part for BOPs for TiAl.

	Al-Al	Ti-Al	Ti-Ti
$R^b$	3.1 Å	3.0 Å	3.1 Å
$R^{cut}$	4.8 Å	4.8 Å	4.8 Å
$C_0$	0.735338470826783	0.874552518642003	0.836483078155529
$C_1$	-0.80650025832614	-0.78709726677780	-0.97139970366448
$C_2$	0.572355022037912	0.485376647846312	0.720715909170425
$C_3$	-0.83236314154484	-0.85094919792282	-0.95769605875943
$C_4$	0.601524357974021	0.619374728994802	0.668672206391629
$C_5$	-0.13754804330203	-0.1359892954513	-0.15125670808728

Table 6.8 The bond part cut-off polynomial tail parameters for BOPs for TiAl

### 6.2.2. Fitting of the Environmentally Dependent Term of BOPs for TiAl

In the second step, the parameters of the environmentally dependent term used in equation (6.3) were fitted to reproduce the two Cauchy pressures, while keeping the bond part fixed. Both Cauchy pressures in L1<sub>0</sub> TiAl are negative:  $C_{12} - C_{66} = -0.040 \text{ eV}/\text{\AA}^3$  and  $C_{13} - C_{44} = -0.213 \text{ eV}/\text{\AA}^3$  (Tanaka *et al.* 1996). The parameters for Ti-Ti interaction ( $s_i = s_j = \text{Ti}$ ) were taken from the potential for hcp titanium - as discussed below, only a minor modification of  $R_c^{TiTi}$  was needed. To simplify the fitting scheme, the two

cross-term parameters ( $s_i = Ti$  and  $s_j = Al$ ), namely  $B^{TiAl}$  and  $R_c^{TiAl}$ , were set equal to the geometric and arithmetic averages of the corresponding parameters for the elements:  $B^{TiAl} = \sqrt{B^{TiTi} B^{AlAl}}$  and  $R_c^{TiAl} = \frac{1}{2}(R_c^{TiTi} + R_c^{AlAl})$ . Thus only parameters for Al-Al interaction  $B^{Al,Al}$ ,  $C^{Al}$ ,  $v^{Al}$ ,  $\lambda_0^{Al}$ ,  $R_c^{Al,Al}$  and  $m^{Al}$  needed to be determined.

The environmentally dependent term is again fitted in such a way as to compensate for the difference between the desired values of the Cauchy pressures and the contribution arising from the bond part. The contributions of the bond part were  $(C_{12}-C_{66})_{\text{bond}} = 0.197 \text{ eV}/\text{\AA}^3$  and  $(C_{13}-C_{44})_{\text{bond}} = 0.062 \text{ eV}/\text{\AA}^3$  (again they were determined by numerically differentiating the bond energy in the code). Hence, the environmentally dependent term has to contribute negatively to both Cauchy pressures in order to be able to reproduce the experimental values. However, it was found that if for Ti-Ti interaction we use the same parameters as for pure Ti this contribution of the environmentally dependent term already gives too negative values of the Cauchy pressures. Specifically, the Ti-Ti contribution was  $(C_{12}-C_{66})_{\text{Ti-Ti}} = -0.607 \text{ eV}/\text{\AA}^3$  and when added to the bond part contribution, it gives  $(C_{12}-C_{66})_{\text{Ti-Ti+bond}} = -0.410$  which is already lower than the experimental value. Adding contributions from the Al-Al and Ti-Al interactions can only make this value more negative. This suggests that the Ti-Ti interaction of the environmentally dependent repulsion is too strong. This is not surprising because the Yukawa-type exponential dependence (see equation (6.3)) can become very large for small separations and the nearest neighbor Ti-Ti separation in TiAl (2.832 Å) is significantly smaller than the Ti-Ti separation in hep titanium (2.950 Å). This is the reason why the weight of this term is increased. To compensate for the shorter

equilibrium separation of Ti-Ti atoms we decreased the value of the parameter  $R_c^{Ti-Ti}$  from 1.0 to 0.9. The Ti-Ti interaction is thus weakened. The resulting contribution  $(C_{12}-C_{66})_{Ti-Ti} = -0.247 \text{ eV}/\text{\AA}^3$ . When the bond part contribution is added, we obtain  $(C_{12}-C_{66})_{Ti-Ti+bond} = -0.050$  which already does not prohibit achieving the fit to the experimental value.

Having solved this problem we proceeded to fitting the parameters for the Al-Al interaction. The parameter  $m^{Al}$  was set equal to 2 while the remaining five parameters  $B^{Al,Al}$ ,  $C^{Al}$ ,  $v^{Al}$ ,  $\lambda_0^{Al}$  and  $R_c^{Al,Al}$  were varied until an adequate fit to the experimental Cauchy pressures was attained. The final parameters of the environmental term are listed in Table 6.9.

	Al-Al	Ti-Ti
B	$10^5 \text{ eV}$	$183.0 \text{ eV}$
C	$210.0 \text{ \AA}^{-2}$	$175.0 \text{ \AA}^{-2}$
v	$2.790 \text{ \AA}^{-1}$	$1.90 \text{ \AA}^{-1}$
$\lambda_0$	$3.308 \text{ \AA}^{-1}$	$3.90 \text{ \AA}^{-1}$
$R_c$	$0.25 \text{ \AA}$	$0.9 \text{ \AA}$
$m$	2.0	2.0

Table 6.9 Parameters of the environmentally dependent term for BOPs for TiAl. Values of the two parameters for the cross-interaction between Ti and Al are calculated as  $B^{TiAl} = \sqrt{B^{TiTi} B^{AlAl}}$  and  $R_c^{TiAl} = \frac{1}{2}(R_c^{TiTi} + R_c^{AlAl})$ .

The Cauchy pressures calculated using the present BOP,  $(C_{12}-C_{66}) = -0.045 \text{ eV}/\text{\AA}^3$

and  $(C_{13}-C_{44}) = -0.206 \text{ eV}/\text{\AA}^3$ , match the experimental values closely. Again, similarly as in the case of the potentials for hcp titanium, a smooth polynomial cut-off tail was introduced starting at 4.8 Å (beyond the second nearest neighbor shell) and ending at 5.4 Å (beyond the third nearest neighbor shell). The parameters of the cut-off are listed in Table 6.10.

	<b>Al</b>	<b>Ti</b>
$R^b$	4.8 Å	4.8 Å
$R^{cut}$	5.4 Å	5.4 Å
$C_5$	-0.009813207336257	-0.795594463095655
$C_4$	-0.015057452374519	-1.229616885597365
$C_3$	-0.006986605277329	-0.540034682670622

Table 6.10 Cut-off tail parameters used in the environmentally dependent term of BOPs for TiAl

### 6.2.3. Fitting of the Pair Potential of BOPs for TiAl

Having determined the parameters of the bond part and the environmentally dependent term, we can now proceed to the fitting of the pair-potential, the functional form of which is given by equation (6.2) as

$$V^{s_i, s_j}(R_{i,j}) = \sum_k A_k^{s_i, s_j} (R_k^{s_i, s_j} - R_{ij})^3 H(R_k^{s_i, s_j} - R_{ij})$$

The species-dependent parameters  $A_k^{s_i, s_j}$ ,  $R_k^{s_i, s_j}$  have to be determined for each type of interactions, Ti-Ti, Al-Al and Ti-Al. The fitted quantities are equilibrium properties of

the L1<sub>0</sub> structure, namely the cohesive energy  $E_{coh}$ , lattice parameters  $a$  and  $c$ , and the remaining elastic moduli. By fitting the two Cauchy pressures through the environmentally dependent term, we have already fixed two out of six independent elastic constants of the L1<sub>0</sub> structure ( $C_{11}$ ,  $C_{12}$ ,  $C_{13}$ ,  $C_{33}$ ,  $C_{44}$  and  $C_{66}$ ) and thus there are four remaining elastic constants (say,  $C_{11}$ ,  $C_{33}$ ,  $C_{44}$ ,  $C_{66}$ ) to be fitted. The total number of fitted quantities is thus seven. To simplify the fitting we again made use of the potential for pure hcp Ti to model the Ti-Ti interaction. The fitting of the parameters for Al-Al and Ti-Al interactions was done similarly as in the case of the potential for pure Ti, by solving a set of linear equations for coefficients  $A_k^{Al-Al}$  and  $A_\ell^{Ti-Al}$ . Since we are fitting seven quantities, we can use seven spline coefficients; we decided to use four for Al-Al interaction and three for Ti-Al interaction. The Al-Al pair-potential thus consists of four spline segments, while the Ti-Al pair-potential of three segments. The following seven equations determine the spline coefficients:

$$(6.20) \quad E_{coh}^{pair} = \frac{1}{2\Omega_0} \sum_{\substack{i,j \\ (s_i, s_j \neq Ti, Ti)}} V^{s_i, s_j}(R_{ij}) = E_{coh} - E_{coh}^{bond} - E_{coh}^{end} - E_{coh}^{Ti-Ti}$$

$$(6.21) \quad \sigma_{11}^{pair} = \frac{1}{2\Omega_0} \sum_{\substack{i,j \\ (s_i, s_j \neq Ti, Ti)}} V'^{s_i, s_j}(R_{ij}) \frac{X_{ij}^2}{R_{ij}^2} = -\sigma_{11}^{bond} - \sigma_{11}^{env} - \sigma_{11}^{Ti-Ti}$$

$$(6.22) \quad \sigma_{33}^{pair} = \frac{1}{2\Omega_0} \sum_{\substack{i,j \\ (s_i, s_j \neq Ti, Ti)}} V'^{s_i, s_j}(R_{ij}) \frac{Z_{ij}^2}{R_{ij}^2} = -\sigma_{33}^{bond} - \sigma_{33}^{env} - \sigma_{33}^{Ti-Ti}$$

(6.23)

$$\frac{1}{2\Omega_0} \sum_{\substack{i,j \\ (s_i, s_j \neq Ti, Ti)}} \frac{\Psi^{s_i, s_j}(R_{ij}) X_{ij}^4}{R_{ij}^2} = C_{11} - C_{11}^{bond} - C_{11}^{env} - C_{11}^{Ti-Ti} + \sigma_{11}^{bond} + \sigma_{11}^{env} + \sigma_{11}^{Ti-Ti}$$

$$(6.24) \quad \frac{1}{2\Omega_0} \sum_{\substack{i,j \\ (s_i, s_j \neq Ti, Ti)}} \frac{\Psi^{s_i, s_j}(R_{ij}) Z_{ij}^4}{R_{ij}^2} = C_{33} - C_{33}^{bond} - C_{33}^{env} - C_{33}^{Ti-Ti} + \sigma_{33}^{bond} + \sigma_{33}^{env} + \sigma_{33}^{Ti-Ti}$$

$$(6.25) \quad \frac{1}{2\Omega_0} \sum_{\substack{i,j \\ (s_i, s_j \neq Ti, Ti)}} \frac{\Psi^{s_i, s_j}(R_{ij}) X_{ij}^2 Z_{ij}^2}{R_{ij}^2} =$$

$$= C_{44} - C_{44}^{bond} - C_{44}^{env} - C_{44}^{Ti-Ti} + \frac{1}{4} \sigma_{11}^{bond} + \sigma_{11}^{env} + \sigma_{11}^{Ti-Ti} + \sigma_{33}^{bond} + \sigma_{33}^{env} + \sigma_{11}^{Ti-Ti}$$

$$(6.26) \quad \frac{1}{2\Omega_0} \sum_{\substack{i,j \\ (s_i, s_j \neq Ti, Ti)}} \frac{\Psi^{s_i, s_j}(R_{ij}) X_{ij}^2 Y_{ij}^2}{R_{ij}^2} = C_{66} - C_{66}^{bond} - C_{66}^{env} - C_{66}^{Ti-Ti} + \frac{1}{2} \sigma_{11}^{bond} + \sigma_{11}^{env} + \sigma_{11}^{Ti-Ti}$$

where separations  $R_{ij}$  correspond to those in the ideal L1<sub>0</sub> lattice with equilibrium lattice parameters  $a, c$ . The values of  $\sigma_{ij}^{bond/env}$  and  $C_{ij}^{bond/env}$  are again obtained by numerical differentiation of the corresponding energy terms in the code. The summation over  $i$  extends over all the atoms in the unit cell and summation over  $j$  is over all the atoms interacting with the atom  $i$ . The summations exclude all the terms corresponding to Ti-Ti interaction since Ti-Ti pair-potential is fixed.  $\Omega_0$  is the equilibrium volume of the unit cell.  $R_{ij}$  is the distance between atoms  $i$  and  $j$ ,  $X_{ij}$  and  $Z_{ij}$  are the  $x$  and  $z$  components of the vector  $\mathbf{R}_{ij}$ , respectively.  $\Psi$  is defined by equation (6.18). Quantities without any superscripts are values that are to be reproduced and the values with superscript

*bond*, *env* and *Ti-Ti* represent contributions of the bond part, the environmentally dependent term and the Ti-Ti pair-potential, respectively. Equation (6.20) is the fitting condition for the cohesion energy  $E_{coh}$ . Equations (6.21) and (6.22) are conditions for fitting the lattice parameters  $a$  and  $c$  by requiring that the stress components  $\sigma_{11}$  and  $\sigma_{33}$  be zero. Equations (6.23) - (6.26) serve for fitting the elastic moduli  $C_{11}$ ,  $C_{33}$ ,  $C_{44}$ , and  $C_{66}$ .

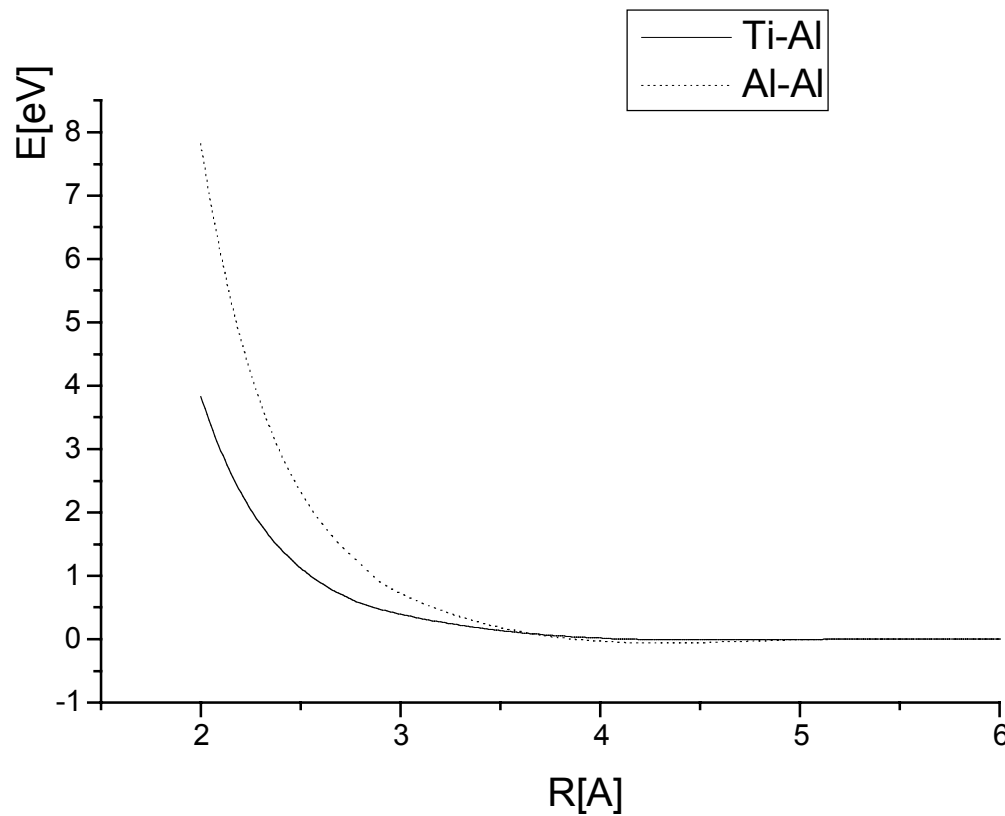


Figure 6.8 The Ti-Al and Al-Al pair potentials.

As in the case of potentials for hcp titanium, (6.20) - (6.26) form a set of linear equations for the spline coefficients  $A_k^{Al-Al}$  ( $k=1,2,3,4$ ) and  $A_\ell^{Ti-Al}$  ( $\ell=1,2,3$ ). These coefficients can be determined for given spline nodes  $R_k^{Al-Al}$  and  $R_\ell^{Ti-Al}$ . In the process of fitting, the positions of the spline nodes were varied and for each set the coefficients  $A_k^{Al-Al}$  and  $A_\ell^{Ti-Al}$  were recalculated. In this way we searched for physically meaningful shapes (i.e. repulsive at small separations and approaching zero at large separations) of both the Al-Al and Ti-Al interactions. However, this could not be achieved if all the experimental elastic constants were to be fitted exactly. Acceptable shapes for both potentials, i. e. without bumps or deep attractive valleys, were obtained for  $C_{11}=1.135 \text{ eV}/\text{\AA}^3$  and  $C_{66}=0.473 \text{ eV}/\text{\AA}^3$  which are very close to the experimental values  $1.167 \text{ eV}/\text{\AA}^3$  and  $0.507 \text{ eV}/\text{\AA}^3$ , respectively. The final fitted pair-potentials for Al-Al and Ti-Al interactions are shown in Fig. 6.8. The coefficients and node points for the Al-Al interactions are listed in Table 6.11, while those for the Ti-Al interaction are presented in Table 6.12. A comparison of experimental values of the cohesive energy, lattice parameters and elastic moduli with those calculated using the constructed BOPs are shown in Table 6.13. While the cohesive energy and the lattice parameters are fitted exactly, only two elastic constants,  $C_{33}$  and  $C_{44}$ , out of six match the experimental values precisely. The approximate fitting of  $C_{11}$  and  $C_{66}$  effects the value of  $C_{12}$ , connected to  $C_{66}$  via the fixed Cauchy pressure  $(C_{12}-C_{66})=-0.045 \text{ eV}/\text{\AA}^3$ . On the other hand, the small deviation of  $C_{13}$  is related to the other Cauchy pressure  $(C_{13}-C_{44})=-0.206 \text{ eV}/\text{\AA}^3$  that deviates by  $0.007 \text{ eV}/\text{\AA}^3$  from the experimental value. None of the calculated values, however, differs from the experiment by more than 10 %, which is certainly a very adequate agreement for our

purposes.

$i$	$A_i^{Al-Al}$	$R_i^{Al-Al}$
1	-0.30049982219861	5.30
2	0.47293603817434	5.10
3	21.70352401338154	3.00
4	47.49189347419121	2.90

Table 6.11 Parameters for the Al-Al pair-potential interaction of the Bond order potentials for TiAl Parameters  $A_i$  - in units of eV/ $\text{\AA}^3$ ,  $R_i$  - in units of  $\text{\AA}$ .

$i$	$A_i^{Ti-Al}$	$R_i^{Ti-Al}$
1	-0.20738373989069	5.30
2	0.27410330332275	5.20
3	2.71679815114202	3.00

Table 6.12.Parameters for the Ti-Al pair-potential interaction of the Bond order potentials for TiAl. Parameters  $a_i$  - in units of eV/ $\text{\AA}^3$ ,  $r_i$  - in units of  $\text{\AA}$ .

	Current work	Experiment
$E_{coh}$	-4.520	-4.520
$a$	4.005	4.005
$c$	4.06908	4.06908
$c/a$	1.016	1.016
$C_{11}$	1.135	1.167
$C_{12}$	0.427	0.467
$C_{13}$	0.474	0.467
$C_{33}$	1.136	1.136
$C_{44}$	0.680	0.680
$C_{66}$	0.473	0.507

Table 6.13 Properties of L1<sub>0</sub> TiAl calculated using the bond-order potential. The experimental lattice parameters  $a$  and  $c$  (in  $\text{\AA}^\circ$ ) were taken from Pearson 1967, the elastic moduli (in  $\text{eV}/\text{\AA}^3$ ) - from Tanaka 1996.

#### 6.2.4. BOPs for TiAl with c/a =1.

In order to be able to deal with cases, such as some of the lamellar interfaces, without resorting to excessively large blocks of atoms, it is convenient to assume the ideal  $c/a$  ratio equal 1 (see Chapter 2). For this purpose we constructed another set of BOPs for TiAl with a modified pair-potential part for which  $c/a = 1$ . This set of potentials

uses the bond-part and environment-dependent term. The pair-potential, however, is fitted to reproduce slightly different lattice parameters, namely  $a=c=4.005$  Å. All the other fitted properties remain the same as those listed in Table 6.13. The fitting of the pair-potential was done the same way as described in the previous section. The resulting parameters are listed in Table 6.14 and Table 6.15.

$i$	$A_i^{Al-Al}$	$R_i^{Al-Al}$
1	-0.19801917905365	5.30
2	0.34709429667575	5.10
3	25.41432898759122	3.00
4	-61.73913669578597	2.90

Table 6.14 Parameters of the Al-Al pair-potential for BOPs predicting ideal c/a=1. Parameters  $A_i$  -

in units of eV/Å<sup>3</sup>,  $R_i$  - in units of Å.

$i$	$A_i^{Ti-Al}$	$R_i^{Ti-Al}$
1	-0.20600926735481	5.30
2	0.26921072547404	5.20
3	2.39759314049279	3.00

Table 6.15 Parameters of the Ti-Al pair-potential for BOPs predicting ideal c/a=1. Parameters  $A_i$  – in units of eV/ $\text{\AA}^3$ ,  $r_i$  - in units of  $\text{\AA}$ .

## 7. TESTING AND SOME APPLICATIONS OF THE BOND ORDER POTENTIALS FOR TiAl

### 7.1. Testing of the Potentials

When fitting Bond Order potentials for TiAl we only reproduced certain properties of the equilibrium L<sub>1</sub><sub>0</sub> structure (see previous chapter). Hence, prior to the employment of these potentials in studies of extended defects it is essential to test their applicability to atomic configurations very different from those encountered in the ideal L<sub>1</sub><sub>0</sub> lattice. As the first test, we calculated the energies of three structures with 1:1 stoichiometry (TiAl) that compete with the tetragonal L<sub>1</sub><sub>0</sub> structure: cubic B2, hexagonal B19 and bcc-based cubic B1 (CsCl ) structure. Energies of these structures, measured with respect to the energy of the L<sub>1</sub><sub>0</sub>, are summarized in Table 7.1; where available ab-initio calculated

	BOP	FP-LMTO
<b>B19 –L1<sub>0</sub></b>	46	42
<b>B2 – L1<sub>0</sub></b>	236	142
<b>B1 – L1<sub>0</sub></b>	987	667

Table 7.1 Energy differences (in eV/atom) between alternate crystal structures with 1:1 composition and the L<sub>1</sub><sub>0</sub> structure calculated ab-initio (Sob *et al.* 1997) using the FP-LMTO method and using the constructed BOP.

energies (Sob *et al.* 1997) are also presented. As discussed in chapter 6, when constructing the potentials the cohesive energy of the L<sub>1</sub><sub>0</sub> structure was fitted. Additional fine-tuning of the bond part of the potentials assured the preference for the tetragonal L<sub>1</sub><sub>0</sub> structure over another close-packed structure - the hexagonal B19. However, except for these adjustments, no other input concerning the energies of alternate structures was used in the fitting. It is seen that while the BOP predicts somewhat higher values of energies than the ab-initio calculations, the order of the increase of the energies of competing structures is the same in both cases. This demonstrates that BOP is capable to predict correctly the relative preference of different structures.

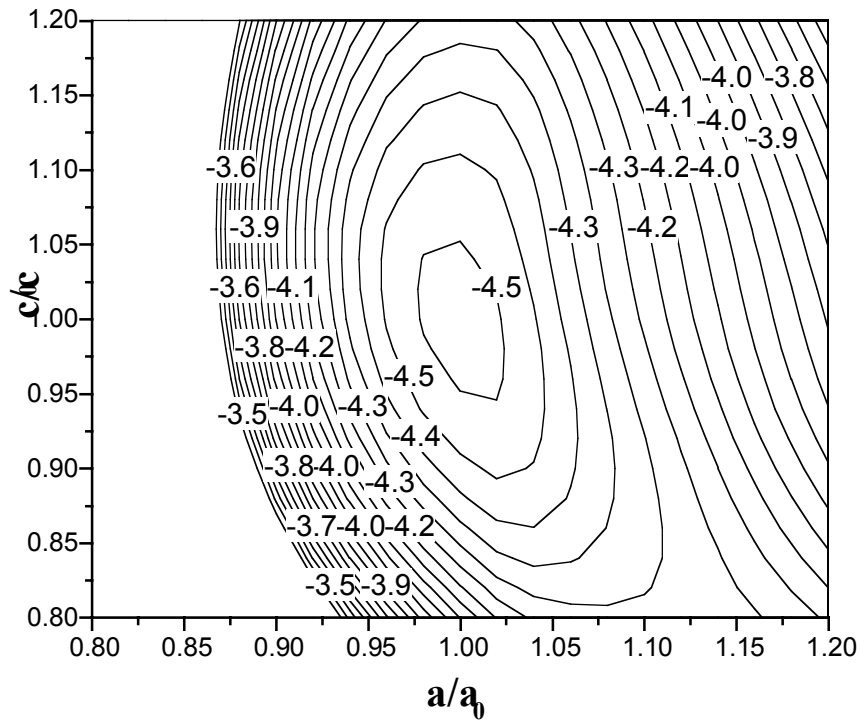


Figure 7.1 Energy surface (in *meV/atom*) for large homogeneous deformation of TiAl unit cell.

The next calculation tests the stability of the L<sub>1</sub><sub>0</sub> structure with respect to large homogenous strains. This has been done by calculating the energy of this structure as a function of homogeneous expansions and contractions (by  $\pm 20\%$ ) of the two lattice parameters  $a$  and  $c$ . The resulting energy surface, shown in terms of the contour maps in Figure 7.1, possesses only one minimum, at the fitted equilibrium values  $a_0$  and  $c_0$ . Hence, within the tested deformation range, the potential does not lead to any instabilities or unphysical metastable configurations.

Considering that no properties of Ti<sub>3</sub>Al were used when fitting the potentials, another pertinent test we performed was to verify that the experimentally observed DO<sub>19</sub> structure is predicted as the most stable structure for the 3:1 composition. For this purpose we calculated the energies of two competing close packed structures, hexagonal DO<sub>19</sub> and cubic L<sub>1</sub><sub>2</sub>; both structures have been fully relaxed with respect to their lattice parameters. We found that the potential correctly predicts that the equilibrium structure is the close packed hexagonal DO<sub>19</sub>. The energy of the cubic L<sub>1</sub><sub>2</sub> structure is higher by 17.3 meV/atom. The ab-initio FP-LMTO calculations show the preference of DO<sub>19</sub> over L<sub>1</sub><sub>2</sub> by 9.5meV/atom (Duc Nguyen-Manh, private communication). This is a very good agreement. Furthermore, Table 7.2 shows comparison between experimental and BOP calculated values of lattice parameter and cohesive energy. The agreement is remarkable, considering that the fitting of the BOPs has been made for the 1:1 alloy in L<sub>1</sub><sub>0</sub> structure.

	<b>Experiment</b>	<b>Calculations</b>
<b><math>a</math></b>	5.780 Å	5.568 Å
<b><math>c</math></b>	4.647 Å	4.634 Å
<b><math>c/a</math></b>	0.804	0.832
<b>Cohesive energy</b>	4.744 eV/atom	4.657 eV/atom

Table 7.2 Equilibrium properties of  $\text{DO}_{19}$   $\text{Ti}_3\text{Al}$ . Comparison of the experimental values with those calculated using BOPs for TiAl.

Since the potentials are intended for atomistic modeling of extended crystal defects which generally involve atomic configurations deviating severely from ideal lattice configurations, they have to be applicable to such atomic environments. While this can never be fully tested because the variety of environments encountered in such defects is very rich, an assessment of the applicability of potentials to such environments can be made by investigating the highly distorted structures encountered along certain transformation paths (Milstein *et al.* 1994; Nguyen-Manh *et al.* 1996; Sob *et al.* 1997; Paidar *et al.* 1999). Three distinct transformation paths have been investigated in this study, tetragonal, trigonal and hexagonal, that connect highly symmetric structures each of which may be, in principle, an equilibrium crystal structure. Each of these three paths can be characterized by a single parameter,  $p$ , and the variation of the total energy of the corresponding structures with the parameter  $p$  has been calculated using both BOP and ab- initio. The latter calculations, made recently in the context of another study (Paidar *et al.* 1999), were performed using the full-potential linearized augmented plane waves (FP-LAPW) code developed by Blaha *et al.* 1990. A detailed description of the three

deformation paths can be found in the paper by Paidar et al. (1999) and here we only summarize the main features of these paths.

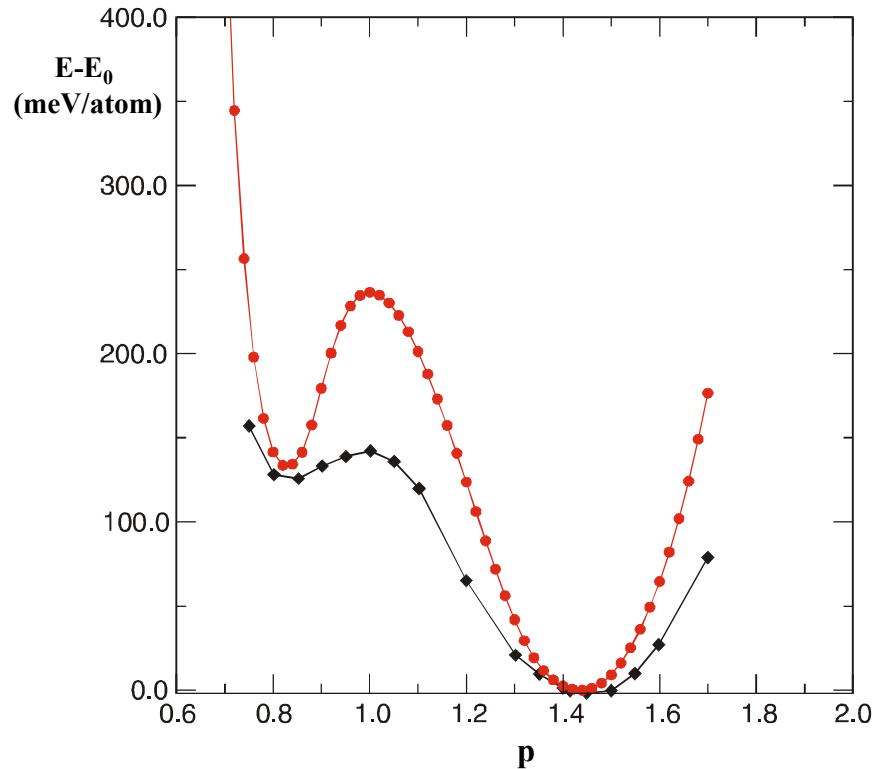


Figure 7.2 Tetragonal transformation. Comparison of BOPs (circles) with FP-LAPW ab-initio data (diamonds) from Paidar *et al.* (1999). A unit cell consisting of 2 atoms was used in the BOP calculation.

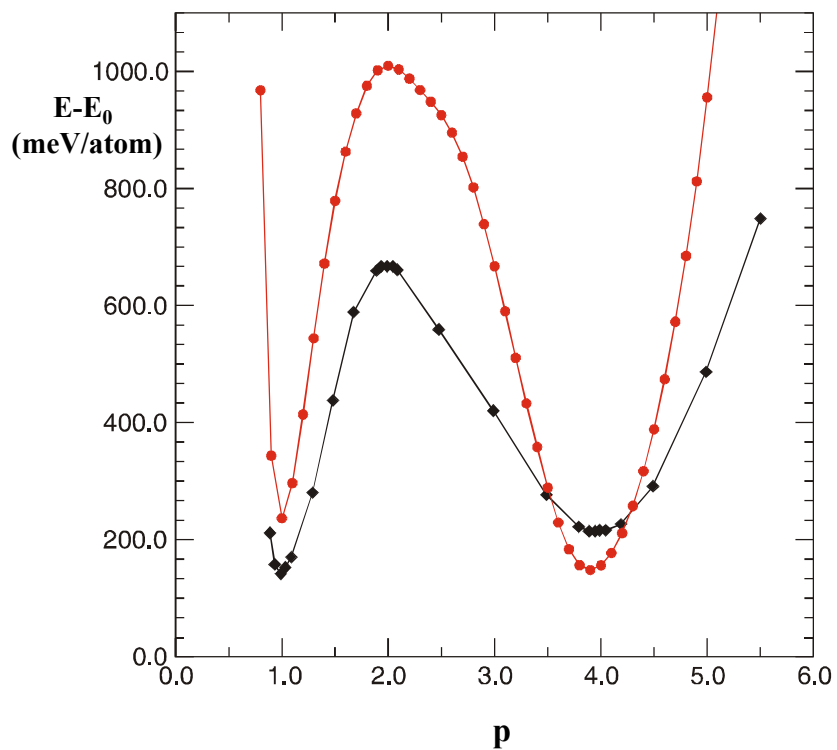


Figure 7.3 Trigonal transformation. Comparison of BOPs (circles) with FP-LAPW ab-initio data (diamonds) from Paidar *et al.* (1999). A unit cell consisting of 12 atoms was used in the BOP calculation.

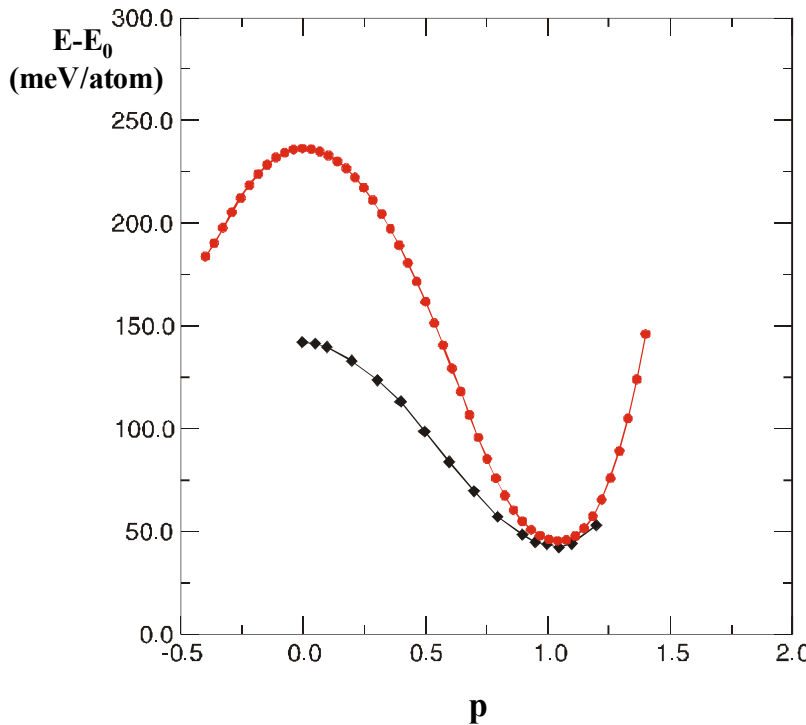


Figure 7.4 Hexagonal transformation. Comparison of BOPs (circles) with FP-LAPW ab-initio data (diamonds) from Paidar *et al.* (1999). A unit cell consisting of 4 atoms was used in the BOP calculation.

The tetragonal path, also called the Bain's path, is the simplest continuous transformation path between the bcc and fcc lattices in elemental solids. It corresponds to homogeneous straining and the parameter  $p$  is the  $c/a$  ratio of the tetragonal structures encountered along that path. In the case of elemental solids  $p=1$  for the bcc lattice and  $p=\sqrt{2}$  for the fcc lattice. In the case of an ordered binary alloy with 50-50 composition,  $p=1$  corresponds to the B2 (CsCl) structure while  $p=\sqrt{2}$  to the L1<sub>0</sub> structure. It should be emphasized that for this path  $p=c/a$  characterizes distortion with respect to the B2 structure.

The trigonal path also corresponds to a homogeneous deformation but in the case of an elemental solid it connects three cubic structures, bcc, simple cubic (sc) and fcc, and the transformation parameter  $p$  varies from 1 for bcc, through 2 for sc to 4 for fcc lattices. The corresponding ordered binary stoichiometric structures are B2, B1 and L1<sub>1</sub>. All other structures encountered along this path also possess the L1<sub>1</sub> symmetry. Finally, the hexagonal transformation path connects in the case of elemental solid the bcc and hcp lattices. However, it does not correspond to a homogeneous deformation. It is a combination of a homogeneous deformation that preserves the atomic volume with shuffling of alternate close packed atomic planes in opposite directions; the shuffling is linearly coupled to the magnitude of straining. In elemental solids  $p=0$  corresponds to the bcc lattice and  $p=1$  to the hcp lattice. All other structures along this path are orthorhombic. In the case of an ordered binary AB alloy,  $p=0$  corresponds to the B2 superlattice and  $p=1$  to the B19 superlattice.

The dependence of the energy per atom on the parameter  $p$  is shown for the three transformation paths considered in Figure 7.2, Figure 7.3 and Figure 7.4. The circles represent the BOP and the diamonds the ab-initio calculations; the energy is always measured relative to the energy of the equilibrium, lowest energy, L1<sub>0</sub> structure. The agreement between BOP and ab-initio calculations is satisfactory. Apart from differences caused by different energy levels of corresponding structures, the general shape of the calculated dependencies is well reproduced. The BOP predicts no additional extrema than those found by the ab-initio calculations and reproduces exactly the position of existing

minima along the deformation paths. This result enhances the credibility of the constructed BOPs for simulation of defects that involve highly distorted configurations.

## 7.2. The (111) $\gamma$ -surface, Energies of Stacking-fault Type Defects and Interfaces

As the first application of the potential we calculated the  $\gamma$ -surface for the (111) plane (see the definition in Chapter 3). This is at the same time another test of the potential since the results can be compared with previous ab-initio calculations. The calculated  $\gamma$ -surface is shown in Figure 7.5 as a surface plot and in Figure 7.6 as a contour plot. The first important point is that the  $\gamma$ -surface is everywhere positive and thus shearing along the {111} plane does not lead to any instabilities with respect to the ideal lattice. As discussed in Chapter 2, close-packed {111} planes play a key role in the plastic deformation of TiAl since they are the slip planes. The metastable stacking-fault-type defects on this plane are therefore very important as they determine possible dislocation splittings and their energies control the extent of these dissociations.

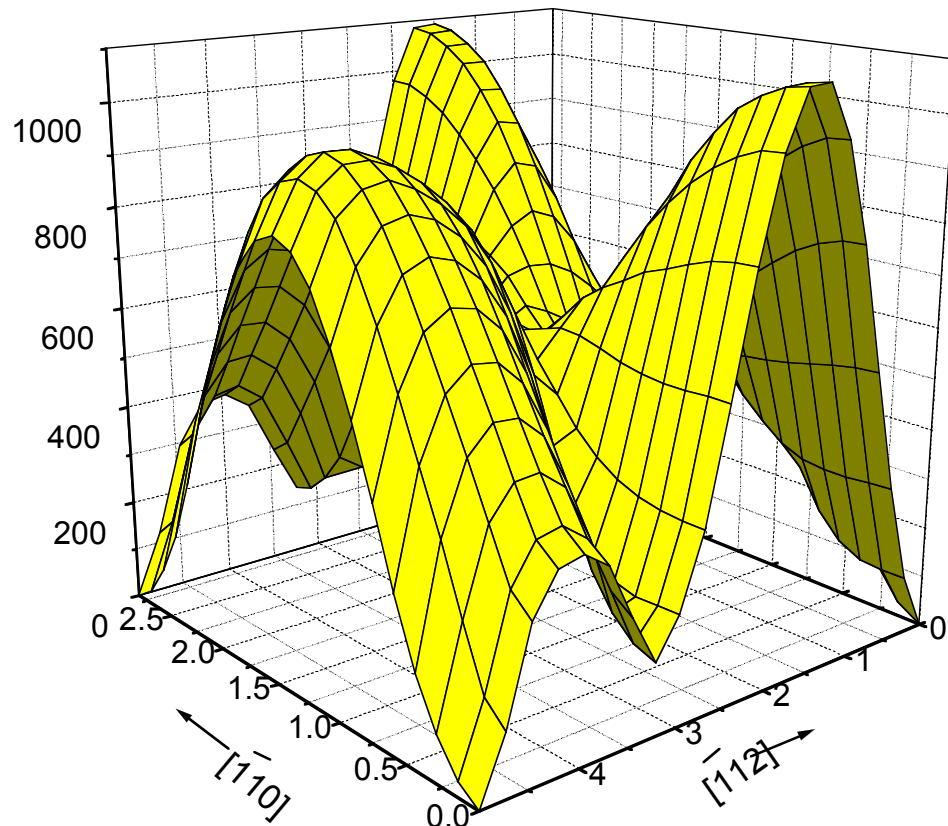


Figure 7.5  $\gamma$ -surface for (111) plane in  $mJ/m^2$  – surface plot. A simulation block consisting of 60 atoms was used in the calculation.

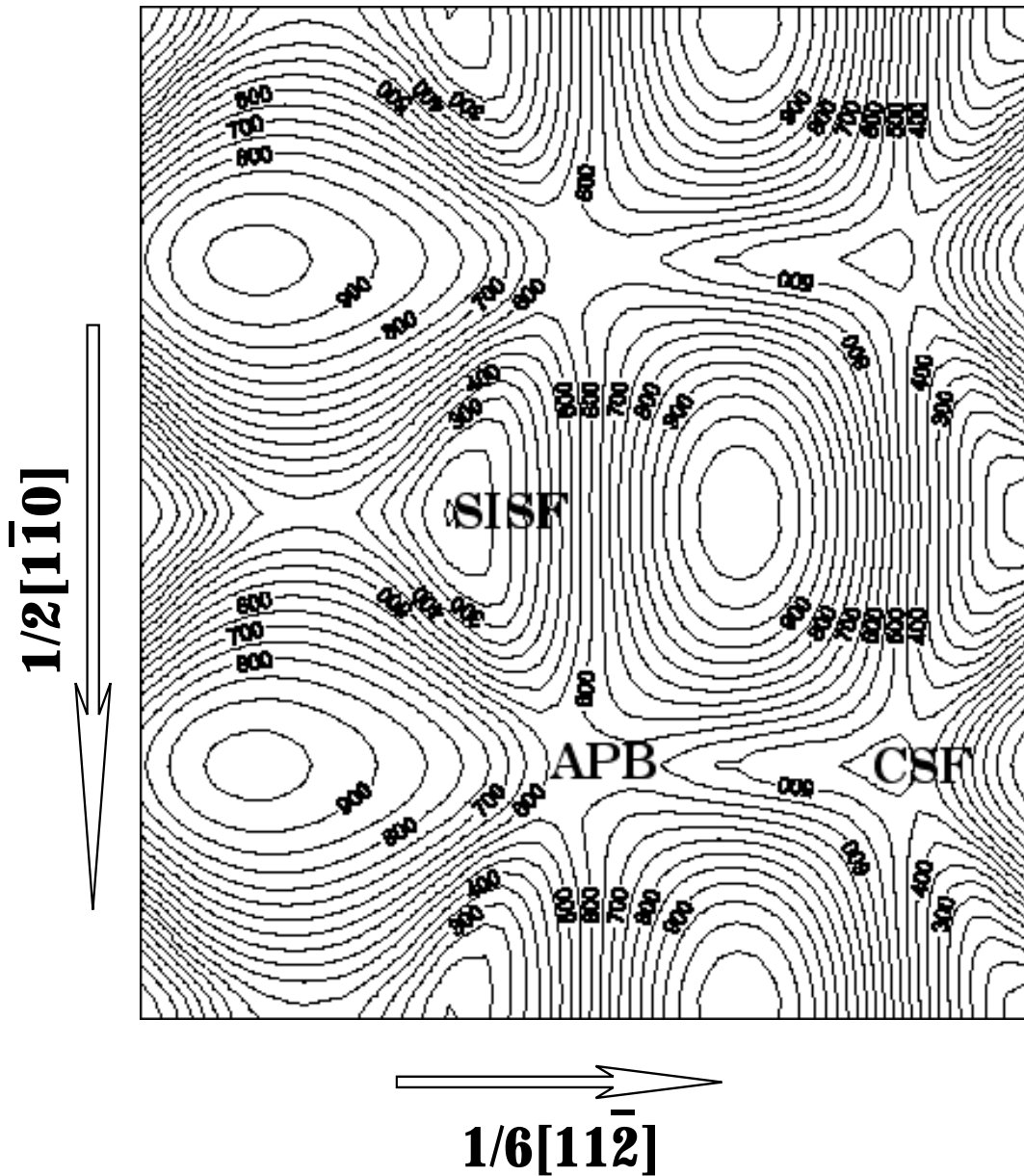


Figure 7.6  $\gamma$ -surface for (111) plane in  $mJ/m^2$  – contour plot. A simulation block consisting of 60 atoms was used in the calculation.

	<b>APB</b>	<b>CSF</b>	<b>SISF</b>
<b>BOP</b>	545	412	140
<b>FP-LAPW</b>	667	362	172
<b>FP-LMTO</b>	710	314	134
<b>FS POTENTIALS</b>	275	275	2.9

Table 7.3 Energies of stacking fault-type defects (in  $mJ/m^2$ ) calculated using four different descriptions of atomic interactions

	<b>APB</b>	<b>CSF</b>	<b>SISF</b>
<b>Experiment (a)</b>	250	---	140
<b>Experiment (b)</b>	190	---	105
<b>Experiment (c)</b>	198	---	116
<b>Experiment (d)</b>	>250	---	140

Table 7.4 Energies of the APB, CSF and SISF on the (111) plane, in  $mJ/m^2$ . (a) Hug, Loiseau and Veyssiére 1988; (b) Hug, Phan-Courson and Blanche 1995; (c) Stucke, Vasudevan and Dimiduk 1995; (d) Wiezorek and Humphreys 1995. Experiments were performed on  $Ti_{46}Al_{54}$  (a,b and d) and  $Ti_{44}Al_{56}$  (c) at room temperature.

The three metastable stacking fault-type defects on the (111) plane, seen in the calculated  $\gamma$ -surface, are the anti-phase boundary (APB) with the displacement  $\frac{1}{2}[\bar{1}01]$ ,

complex stacking fault (CSF) with the displacement  $\frac{1}{6}[\bar{2}11]$  and super lattice intrinsic stacking fault (SISF) with the displacement  $\frac{1}{6}[11\bar{2}]$  (see also chapter 2, Figure 2.18). The energies of these faults, calculated using our potentials, are shown in Table 7.3 where they are also compared with those evaluated ab-initio using FP-LAPW (Ehmann and Fahnle 1998) and FP-LMTO (Vitek *et al.* 1997a) methods, and when employing the Finnis-Sinclair (FS) type potentials (Vitek *et al.* 1997a). Available experimental values are listed in Table 7.4. The agreement between BOP and ab-initio calculations is very good. Importantly, the relatively high energy of the SISF is correctly reproduced. In the case of the Finnis-Sinclair type potential this energy is very low because the separations of the first and second nearest neighbors are practically the same as in the ideal L<sub>1</sub><sub>0</sub> lattice when this fault is formed, and in the framework of central forces the only contributions to the fault energy arise from more distant neighbors. This suggests that the relatively large energy of the SISF results mainly from changes in bond angles. It is very encouraging to see that owing to the fact that directional bonding is included in the BOP scheme, the potential captures the fault energies accurately.

The BOPs predict that all three planar faults suggested crystallographically are metastable and may thus participate in the dislocation dissociation. Interestingly, the two ab-initio calculations; both the FP-LAPW of Ehmann and Fahnle (1998), and our calculations using the FP-LMTO method (Vitek *et al.* 1997a), find that the APB is mechanically unstable with respect to the displacement along the <112> direction towards the position of the complex stacking fault. In order to verify the stability of the APB in the BOP scheme we calculated in detail the cross section of the  $\gamma$ -surface along

the line parallel to the  $<112>$  direction, passing through the point corresponding to the  $\frac{1}{2}[\bar{1}01]$  displacement of the APB. Results are shown in Figure 7.7 for both the BOPs (circles) and the FP LAPW (diamonds). While the FP-LAPW data show an inflection point at the APB, BOPs predict a shallow local minimum for this configuration. This means that for BOPs the APB is indeed metastable with respect to the displacement along the  $<112>$  direction. However, the minimum corresponding to this fault is very shallow and its energy very high and thus the differences between ab initio and BOP results are not crucial. Different dislocation dissociations involving the stacking fault-type defects analyzed in this section will be discussed in the following Chapter.

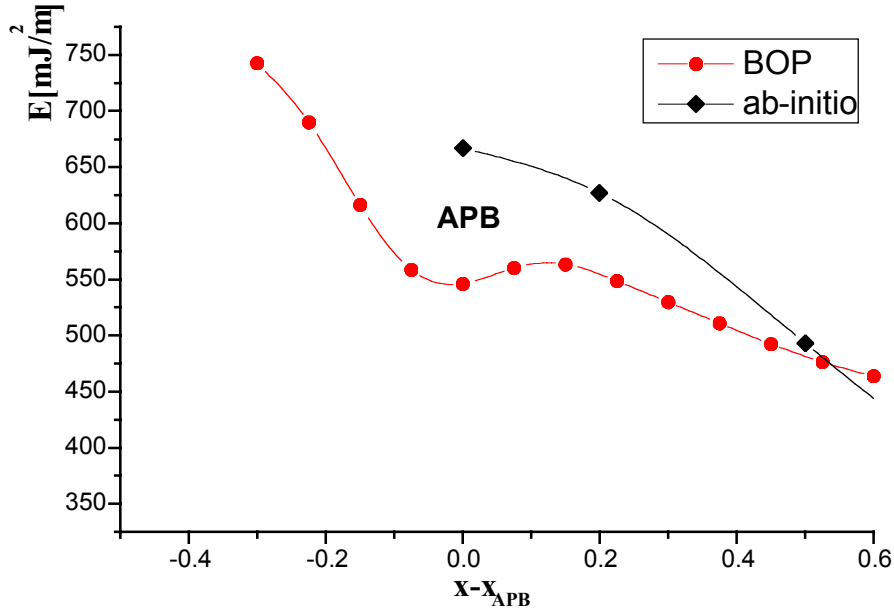


Figure 7.7 The energy profile in the vicinity of the APB along the  $[11\bar{2}]$  direction. The x-axis measures the displacement from the APB in fractions of the  $\frac{1}{6}[11\bar{2}]$  vector.

Another application, the results of which can be compared with ab-initio studies, is calculation of energies of  $\gamma/\gamma$  interfaces that are present in PST crystals (see chapter 2): the  $120^\circ$  rotational fault (Figure 2.15), the twin (Figure 2.16) and the pseudotwin (Figure 2.17). For the twin boundary we also considered the configuration with additional APB shift. Since the directions  $[1\bar{1}0]$  and  $[\bar{1}01]$  are not equivalent when the  $c/a$  ratio differs from 1 a misfit arises in the  $120^\circ$  rotational fault and the pseudotwin. In order to avoid this misfit these interfaces were modeled assuming the  $c/a$  ratio equal 1 using the potential II, which was fitted so as to produce such ideal  $c/a$  (see section 6.2.4). Potential

II was employed in the other calculations the results of which we list below for comparison. The results of our calculations are compared in Table 7.5 to two different ab-initio studies as well as calculations employing Finnis-Sinclair potentials. The agreement of our results with ab-initio calculations is certainly very satisfactory. The case of the ordered twin again emphasizes the importance of directional bonding that is appropriately accounted for in the BOP. The low value of the energy of this interface predicted by the Finnis-Sinclair potentials has its roots, similarly as in the case of the SISF, in the fact that the separations of the first and second neighbors are practically the same as in the ideal lattice. Thus the energy of the ordered twin is principally determined by different bond angles when compared with the ideal lattice.

In the experimental study of Lu *et al.* (1995) relative energies of  $\gamma/\gamma$  interfaces in the PST crystal were determined using the Atomic Force Microscope (AFM) by measuring angles of surface grooves. According to this work the ratios of energies of the twin, the  $120^\circ$  rotational fault and the pseudotwin are 1: 5.8 : 6.7. Our calculations predict the ratios 1: 4.1 : 4.2 , while the two ab-initio calculations predict values 1: 2.2 : 2.0 (FP-LMTO) and 1: 4.5 : 4.2 (FP-LAPW). The ratios predicted by the Finnis Sinclair potential are 1:103:104. Even though the agreement between the experiment and our BOP calculations is not exact, when compared to the results predicted by the Finnis-Sinclair, we can conclude that using the Bond Order Potentials results in an enormous improvement.

	<b>BOP</b>	<b>FP-LMTO</b>	<b>FP-LAPW</b>	<b>FS</b>
<b>Ordered Twin</b>	74.2	109	60	1.4
<b>120° rotational fault</b>	306	235	270	144
<b>Pseudotwin</b>	310	213	250	145
<b>Ordered twin with APB</b>	456	501	550	288

Table 7.5 The energies of  $\gamma/\gamma$  interfaces calculated using the BOPs for TiAl compared to FP-LMTO (Vitek, *et al.* 1997a), FP-LAPW (C.L. Fu, unpublished results) and Finnis-Sinclair (FS) data (Vitek *et al.*, 1997a). A simulation block of 60 atoms was used in the BOP calculations for the ordered twin and twin with APB, while in the calculations of the other two interfaces blocks consisting of 240 atoms were used.

### 7.3. Point Defects

Finally, we calculated the energies associated with formation of point defects in TiAl, such as vacancies and anti-sites at both Ti and Al sites. Due to the presence of two (or more) types of species in alloys there is no unique way of assigning an energy per atom of a given kind even in the stoichiometric case. Hence, it is not immediately obvious how to calculate quantities such as formation energies of vacancies. When dealing with point defects we followed the statistical approach recently proposed by Mishin and Herzig (2000) that employs the concept of the “raw” energies of point

defects. The “raw” energy associated with a point defect is defined as the difference between the energy of the block with the defect (vacancy, antisite) and the same block of the ideal lattice. This quantity is obtained directly from the corresponding computer simulation. In our calculations of raw energies we used unit cells consisting of 107 and 108 atoms for vacancies and anti-sites respectively.

The effective formation energies,  $\epsilon^{eff}$ , that appear in the expression  $\exp(-\epsilon^{eff} / k_B T)$  determining the equilibrium concentration of the corresponding point defects, can be evaluated from “raw” energies of defects involved in the formation of the point defect studied (for details see Mishin and Herzig 2000). For example, effective formation energies of vacancies at Al and Ti sites,  $\epsilon_{V_{Al}}^{eff}$  and  $\epsilon_{V_{Ti}}^{eff}$ , respectively, are calculated as follows:

$$(7.1) \quad \epsilon_{V_{Al}}^{eff} = \epsilon_0 + \epsilon_{V_{Al}}^{raw} + \frac{1}{4}(\epsilon_{Al \rightarrow Ti}^{raw} - \epsilon_{Ti \rightarrow Al}^{raw})$$

$$(7.2) \quad \epsilon_{V_{Ti}}^{eff} = \epsilon_0 + \epsilon_{V_{Ti}}^{raw} + \frac{1}{4}(\epsilon_{Ti \rightarrow Al}^{raw} - \epsilon_{Al \rightarrow Ti}^{raw})$$

$\epsilon_0$  is the cohesive energy per atom,  $\epsilon_{V_{Al}}^{raw}$ ,  $\epsilon_{V_{Ti}}^{raw}$  are the corresponding “raw” vacancy energies,  $\epsilon_{Al \rightarrow Ti}^{raw}$  is the “raw” energy of an anti-site formed by replacing a Ti atom by an Al atom, and  $\epsilon_{Ti \rightarrow Al}^{raw}$  is the “raw” energy of an anti-site formed by replacing an Al atom by a Ti atom.

Similarly, the effective anti-site defect energies can be calculated as

$$(7.3) \quad \epsilon_{Ti \rightarrow Al}^{eff} = \frac{1}{2}(\epsilon_{Ti \rightarrow Al}^{raw} + \epsilon_{Al \rightarrow Ti}^{raw})$$

$$(7.4) \quad \epsilon_{Al \rightarrow Ti}^{eff} = \frac{1}{2} (\epsilon_{Al \rightarrow Ti}^{raw} + \epsilon_{Ti \rightarrow Al}^{raw})$$

Obviously, for the stoichiometric case  $\epsilon_{Ti \rightarrow Al}^{eff} = \epsilon_{Al \rightarrow Ti}^{eff}$ .

The raw energies are quantities directly evaluated in atomistic studies but not easily comparable between different calculations and not at all with experiment. Comparable quantities are the effective formation energies, but the best is to compare energies of defects that do not change stoichiometry. The following are a few examples:

**Exchange defect:**  $(Al \rightarrow Ti) + (Ti \rightarrow Al)$

Formation energy:  $\epsilon_{Al \rightarrow Ti}^{eff} + \epsilon_{Ti \rightarrow Al}^{eff} = 2\epsilon_{Ti \rightarrow Al}^{eff}$

**Double vacancy:**  $V_{Ti} + V_{Al}$

Formation energy:  $\epsilon_{V_{Ti}}^{eff} + \epsilon_{V_{Al}}^{eff}$

**Two Ti vacancies and anti-site:**  $2V_{Ti} + (Ti \rightarrow Al)$

Formation energy:  $2\epsilon_{V_{Ti}}^{eff} + \epsilon_{Ti \rightarrow Al}^{eff}$

**Two Al vacancies and anti-site:**  $2V_{Al} + (Al \rightarrow Ti)$

Formation energy:  $2\epsilon_{V_{Al}}^{eff} + \epsilon_{Al \rightarrow Ti}^{eff}$

	$\epsilon_{V_{Al}}^{raw}$	$\epsilon_{V_{Ti}}^{raw}$	$\epsilon_{Al \rightarrow Ti}^{raw}$	$\epsilon_{Ti \rightarrow Al}^{raw}$	$\epsilon_0$
<b>Unrelaxed BOP</b>	5.237	6.667	2.815	-0.598	-4.520
<b>Relaxed BOP</b>	5.036	6.327	2.342	-0.694	-4.520
<b>FS</b>	5.342	6.779	2.061	-1.189	-4.520
<b>EAM</b>	5.092	6.257	1.859	-0.975	-4.3960

Table 7.6 Raw energies of point defects in TiAl (in eV). Comparison of results calculated by Bond order potentials for TiAl with Finnis-Sinclair (FS) data (Nomura and Vitek, to be published) and Embedded Atom Method (EAM) data (Mishin and Herzig, 2000).

	$\epsilon_{V_{Ti}}^{eff}$	$\epsilon_{V_{Al}}^{eff}$	$\epsilon_{Al \rightarrow Ti}^{eff} = \epsilon_{Ti \rightarrow Al}^{eff}$
<b>Unrelaxed BOP</b>	1.29	1.57	1.11
<b>Relaxed BOP</b>	1.05	1.28	0.82
<b>Woodward et. al</b>	1.59	1.99	0.60
<b>Fu and Yoo</b>	1.95	2.46	0.72
<b>FS</b>	1.40	1.63	0.44
<b>EAM</b>	1.15	1.41	0.44

Table 7.7 Effective energies of point defects in TiAl (in eV). Comparison of results calculated by Bond order potentials for TiAl with Finnis-Sinclair (FS) data (Nomura and Vitek, to be published), Embedded Atom Method (EAM) data (Mishin and Herzig, 2000) and two ab-initio calculations (Woodward *et al.* 1998, Fu and Yoo 1990).

	<b>Exchange defect</b>	<b>Double vacancy</b>	<b>Two Ti vacancies and anti-site</b>	<b>Two Al vacancies and anti-site</b>
<b>Unrelaxed BOP</b>	2.22	2.86	3.69	4.25
<b>Relaxed BOP</b>	1.65	2.33	2.92	3.38
<b>Woodward et. al</b>	1.20	3.58	3.78	4.59
<b>Fu and Yoo</b>	1.44	4.41	4.62	5.64
<b>FS</b>	0.87	3.03	3.24	3.69
<b>EAM</b>	0.88	2.56	2.74	3.25

Table 7.8 Effective formation energies of point defects preserving stoichiometry. Comparison of results calculated by Bond order potentials for TiAl with Finnis-Sinclair (FS) data (Nomura and Vitek, to be published), Embedded Atom Method (EAM) data (Mishin and Herzig, 2000) and two ab-initio calculations (Woodward *et al.* 1998, Fu and Yoo 1990).

Tables 7.6-7.8 list the results of our point defect calculations in comparison with results of two recent calculations performed using an embedded atom potential constructed by Farkas, 1994 (Mishin and Herzig 2000) and the Finnis-Sinclair type potential (Nomura and Vitek, to be published) together with results of two ab-initio calculations of Woodward *et al.* (1998) and Fu and Yoo (1990). As can be seen from the tables, predictions of BOPs follow the general trends and agree with the other calculations in predicting the correct ordering of energies for different point defects.

## **8. STUDIES OF DISLOCATIONS IN L<sub>1</sub><sub>0</sub> TiAl**

As discussed in chapter 2, core structure and related mobility of dislocations are the key factors for understanding the deformation behavior of  $\gamma$ -TiAl. This chapter describes our studies of dislocations in L<sub>1</sub><sub>0</sub> TiAl made using the newly developed Bond order potentials for this compound.

### **8.1. Review of Experimental Observations of Dislocations in L<sub>1</sub><sub>0</sub> TiAl**

Dislocations with three different Burgers vectors have been observed in L<sub>1</sub><sub>0</sub> TiAl.  
- two ordinary dislocations with Burgers vectors  $1/2\langle 110 \rangle$  (Shechtman, Blackburn and Lipsitt 1974) and  $1/2\langle 112 \rangle$  (Lipsitt, Shechtman and Schafrik 1975), and the superlattice dislocations with the Burgers vector  $\langle 101 \rangle$  (Hug, Loiseau and Lasalmonie 1986). These dislocations are all gliding in the close-packed {111} planes. The plastic deformation of  $\gamma$ -TiAl proceeds by glide of either ordinary dislocations or superdislocations and/or by twinning (Court, Vasudevan and Fraser 1990; Sriram, Vasudevan and Dimiduk, 1995). The  $1/2\langle 112 \rangle$  dislocations have not been observed to glide but may play a role in the twinning process (Inkson and Humphreys 1995; Girshick, 1997). In this thesis we present results of the computer modeling of the core structures of ordinary  $1/2\langle 110 \rangle$  dislocations and  $\langle 101 \rangle$  superdislocations and discuss possible implications of these structures for their glide. Investigation of  $1/2\langle 112 \rangle$  dislocations and their relation to twinning has not been made since it represents another extensive independent study (see

e.g. Min-Chul Kim, M. Nomura, V. Vitek and D. P. Pope, 1999) and it is proposed as one of the future investigations.

Ordinary  $1/2\langle 110 \rangle$  dislocations may, in principle, dissociate into Shockley partials separated by the complex stacking fault (CSF), just like dislocations in fcc crystals. However, the energy of the CSF is rather high (see Table 7.2) which renders such splitting energetically unfavorable as will be shown in more detail in Section 8.3 of this chapter. The weak-beam electron microscope observations (see e.g. Hemker, Viguier and Mills, 1993), indeed, do not reveal such splitting and suggest a compact core structure.

In contrast with the ordinary dislocation, the  $\langle 101 \rangle$  superdislocation may dissociate in both planar and non-planar manner. All the planar dissociations discussed in the literature (see e.g. Wiezorek and Humphreys, 1995) can be derived from the following four-fold splitting into Shockley type partials on the (111) plane which involves all three stacking-fault like defects, APB, SISF and CSF (see Figure 2.18).

$$(8.1) \quad [10\bar{1}] = 1/6[11\bar{2}] + SISF + 1/6[2\bar{1}\bar{1}] + APB + 1/6[11\bar{2}] + CSF + 1/6[2\bar{1}\bar{1}]$$

However, only two-fold and three-fold dissociations were observed experimentally. The possible three-fold schemes are

$$(8.2) \quad [10\bar{1}] = 1/6[11\bar{2}] + SISF + 1/6[2\bar{1}\bar{1}] + APB + 1/2[10\bar{1}]$$

and

$$(8.3) \quad [10\bar{1}] = 1/6[11\bar{2}] + SISF + 1/2[10\bar{1}] + CSF + 1/6[2\bar{1}\bar{1}]$$

Both these splitting schemes are demonstrated in Figure 2.18. Configuration (8.2) was reported by Hug, Loiseau and Veyssiére (1988), Li and Whang (1992), Morris, Gunter and Leboeuf (1994). The possible twofold splittings that can be deduced from the general scheme (8.1) are

$$(8.4) \quad [10\bar{1}] = 1/6[11\bar{2}] + SISF + 1/6[5\bar{1}\bar{4}]$$

$$(8.5) \quad [10\bar{1}] = 1/2[10\bar{1}] + APB + 1/2[10\bar{1}]$$

Which of the dissociations is favored depends principally on the energies of the stacking-fault like defects. The dissociation according to the reaction (8.2) can be expected if the energy of the CSF is very high and thus dissociation into Shockley partials is not favored, while the APB is metastable and its energy is sufficiently low. In contrast, the reaction (8.3) may be anticipated if the APB is either unstable or its energy is so high that it does not participate in the dissociation while the energy of the CSF is low enough to favor the splitting into Shockley partials. However, if the energy of the CSF is so high that further splitting into Shockley partials is not favored then the splitting according to (8.4) may be expected. Such configuration was observed by Stucke, Vasudevan and Dimiduk (1995) in Al-rich TiAl and by Sriram, Vasudevan and Dimiduk (1995) in nearly stoichiometric TiAl alloys. For lower energies of APB but high energy of the CSF the splitting according to (8.5) is, in principle, possible but this was never observed.

Furthermore, the  $[10\bar{1}]$  superdislocation can dissociate into two ordinary dislocations (Hug, Loiseau and Lasalmonie 1986; Hug, Loiseau and Veyssiére 1988; Sriram, Vasudevan and Dimiduk 1995) according to the reaction

$$(8.6) \quad [10\bar{1}] = 1/2[1\bar{1}0] + 1/2[11\bar{2}]$$

This dissociation involves  $1/2[11\bar{2}]$  dislocation that may play role in the twinning process. However, as mentioned above, we have not investigated this dislocation in this thesis.

The  $[10\bar{1}]$  superdislocation may also dissociate in a non-planar manner into  $(111)$  and  $(1\bar{1}1)$  planes forming ribbons of the SISF on these planes. The corresponding reaction is:

$$(8.7) \quad [10\bar{1}] = 1/6[11\bar{2}] + SISF_{(111)} + 1/3[20\bar{1}] + SISF_{(1\bar{1}1)} + 1/6[1\bar{1}\bar{2}]$$

The  $1/3[20\bar{1}]$  dislocation can further split into two partials separated by an APB on the cube plane leading to

$$(8.8) \quad [10\bar{1}] = 1/6[11\bar{2}] + SISF_{(111)} + 1/6[21\bar{1}] + APB_{(010)} + 1/6[2\bar{1}\bar{1}] + SISF_{(1\bar{1}1)} + 1/6[1\bar{1}\bar{2}]$$

This type of splitting was reported in the high-resolution transmission electron microscopy (HREM) study of Hemker, Viguier and Mills, 1993.

## **8.2. Atomistic Studies of $\langle 110 \rangle$ Type Ordinary and Super Dislocations in L1<sub>0</sub>**

### **TiAl**

In this section we present the results of atomistic studies of the structure of the  $1/2\langle 110 \rangle$  ordinary dislocation and the  $\langle 101 \rangle$  superdislocation performed using our bond order potentials for TiAl. These two dislocations had been studied in the past using semi-empirical many-body potentials such as Embedded atom method (EAM) (Daw and

Baskes, 1984) and Finnis-Sinclair (FS) potentials (Finnis and Sinclair, 1984). Simmons, Rao and Dimiduk (1993) developed three sets of EAM potentials for TiAl that were used in dislocation studies; the three potentials (labeled NTA01, NTA02 and NTA03) differed principally by the predicted values of the energy of the CSF. Panova and Farkas (1995) used yet another EAM potentials for TiAl in their studies of dislocation cores. Finally, a Finnis-Sinclair type potential, developed by Girshick, 1997, was employed to study the core structures of several dislocations in  $L1_0$  TiAl. The results of our calculations will be compared with these previous studies and similarities and differences of the results discussed.

In the following the core structures of the dislocations are depicted using the method of differential displacements (Vitek, Perrin and Bowen 1970; Vitek 1992). The atomic block is always shown in the projection onto the plane perpendicular to the dislocation line. The arrows indicate the relative displacement of the atoms either parallel or perpendicular to the Burgers vector. In the case of screw dislocations these two components are the screw and edge components of the displacement, respectively. The length of the arrows is proportional to the magnitude of the displacement and is normalized such that the length of the largest arrow is equal to the separation of the neighboring atoms in the given projection.

### **8.2.1. Ordinary $1/2\langle 110 \rangle$ Dislocation**

Simmons, Rao and Dimiduk, 1997, calculated the core structures of the  $1/2\langle 110 \rangle$  ordinary dislocation using the EAM potentials NTA01, NTA02 and NTA03.

They considered several orientations of the dislocation line - screw,  $30^\circ$  mixed,  $60^\circ$  mixed and edge. According to their calculations the cores of all these dislocations may be planar, confined to the  $(111)$  plane. Notwithstanding, for the NTA02 potential two distinct configurations of the screw dislocation were found. One planar and the other non-planar; the non-planar core spreads into two intersecting  $\{111\}$  planes. However, the non-planar core was found to be unstable since it transformed into the planar configuration under the effect of an applied stress. Furthermore, for both the NTA02 and NTA03 potentials the  $60^\circ$  mixed dislocations was found to exhibit the core in which the screw and edge components spread into two different intersecting  $\{111\}$  type planes. Girshick (1997) also found two configurations for the screw orientation of the  $1/2\langle 110 \rangle$  ordinary dislocation. However, in this case the non-planar core was found to be favored over the planar configuration and the planar core transformed under the applied stress into the non-planar configuration. This result is just opposite to that of Simmons et al. 1997. Panova and Farkas (1995), using different EAM potentials, found only the non-planar configuration, spreading into two  $\{111\}$  planes for the screw orientation of the ordinary  $1/2\langle 110 \rangle$  dislocation; the edge dislocation was found to posses a planar core.

The most interesting orientation of the ordinary  $1/2\langle 110 \rangle$  dislocation is the screw orientation since screw dislocations do not have a well-defined glide plane and thus there is no a priori preference for planar spreading of their cores (Vitek 1992). Furthermore, the dislocation line direction is common to two non-parallel  $\{111\}$  planes, for example  $(111)$  and  $(1\bar{1}\bar{1})$  in the case of the  $[1\bar{1}0]$  direction, and thus spreading into equivalent crystallographic planes can occur. This ambiguity is clearly reflected in the results of

previous atomistic calculations summarized above. Hence, our first atomistic calculation of dislocations employing the BOP has been simulation of the core of the  $1/2[1\bar{1}0]$  screw dislocation. Unlike in the study of Girshick (1997) and Simmons, Rao and Dimiduk (1997), we found only one configuration for the dislocation core. It is shown in Figure 8.1 where the screw component of the displacement is plotted; the edge component is not shown since it was found to be practically negligible. As can be seen from this figure, the core is non-planar, spread into  $(111)$  and  $(1\bar{1}\bar{1})$  planes.

The next interesting dislocation orientation is the  $60^\circ$  mixed  $1/2[1\bar{1}0]$  dislocation reported to display non-planar behavior by Simmons, Rao and Dimiduk (1997). This dislocation lies parallel to the  $[10\bar{1}]$  direction that is common to the  $(111)$  and  $(1\bar{1}\bar{1})$  planes and thus spreading of the core into these two non-parallel, crystallographically equivalent planes, is feasible. Our calculations, indeed, predict a non-planar core for this orientation of the dislocation line. This can be seen in Figure 8.2 which shows the displacement map in which the arrows represent displacements along the  $[10\bar{1}]$  direction, i. e. the screw component parallel to the dislocation line. The core spreads, similarly as in the case of the screw dislocation, into two non-parallel  $\{111\}$  planes,  $(111)$  and  $(1\bar{1}1)$ . The edge displacement along the  $[\bar{1}2\bar{1}]$  direction, perpendicular to the dislocation line, displayed in Figure 8.3, also shows evidence of non-planar core spreading.

Since both the screw and  $60^\circ$  mixed ordinary  $1/2\langle 110 \rangle$  dislocations have non-planar cores, it is very likely that very high stresses will be needed for their motion at 0K, i. e. both these dislocations are likely to be sessile. At finite temperatures their movement

can be assisted by thermal activations and a strong temperature dependence of the related glide stress can be expected.

In the calculation for the screw orientation a simulation block consisting of 200 active and 340 inert atoms was used (see Section 3.2), while for the 60° mixed orientation we used a block consisting of 181 active and 518 inert atoms.

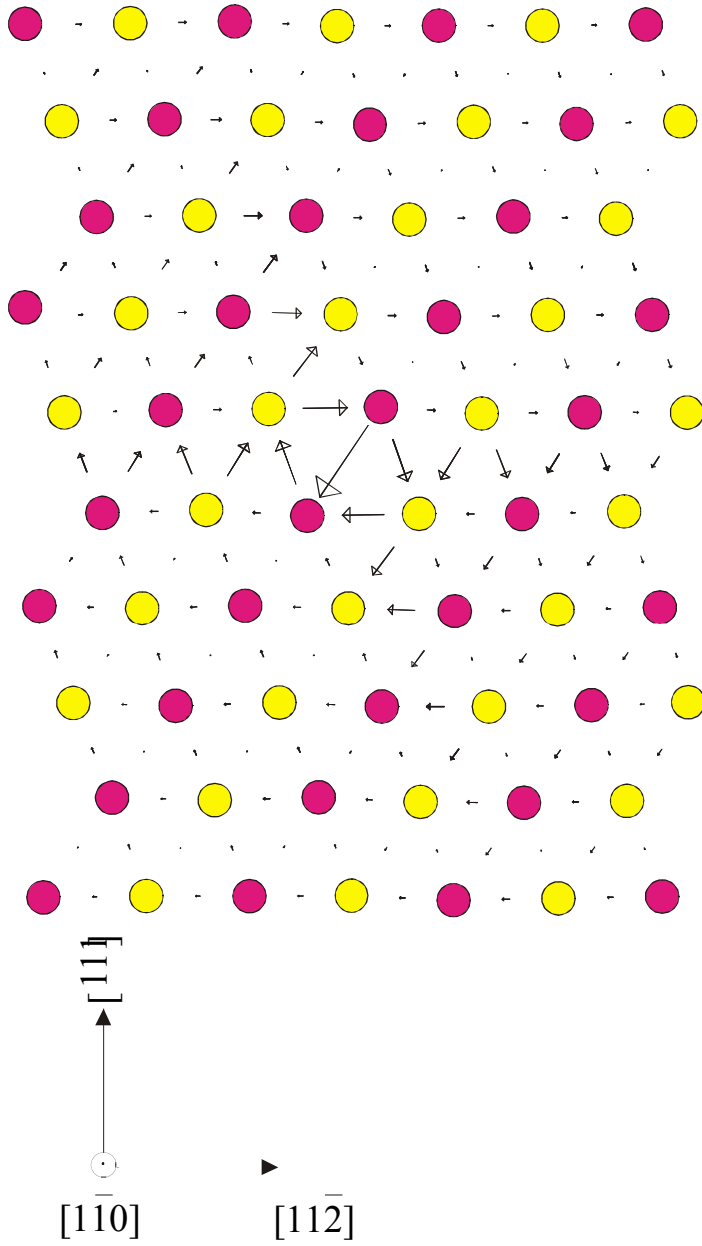


Figure 8.1 The non-planar core of the  $1/2[1\bar{1}0]$  ordinary screw dislocation in TiAl depicted by the plot of the screw component parallel to  $[1\bar{1}0]$ .

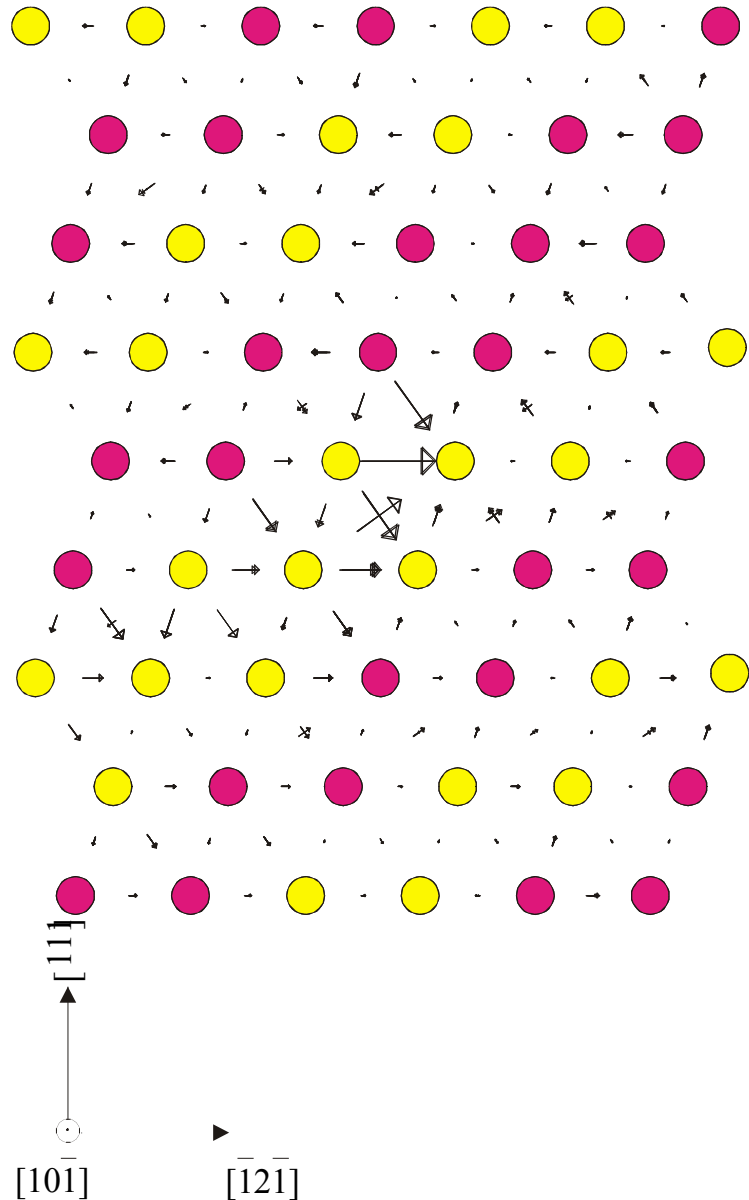


Figure 8.2 The core structure of the  $1/2[1\bar{1}0]$  ordinary  $60^\circ$  mixed dislocation in TiAl depicted by the component of the displacement along the  $[10\bar{1}]$  direction (screw component).

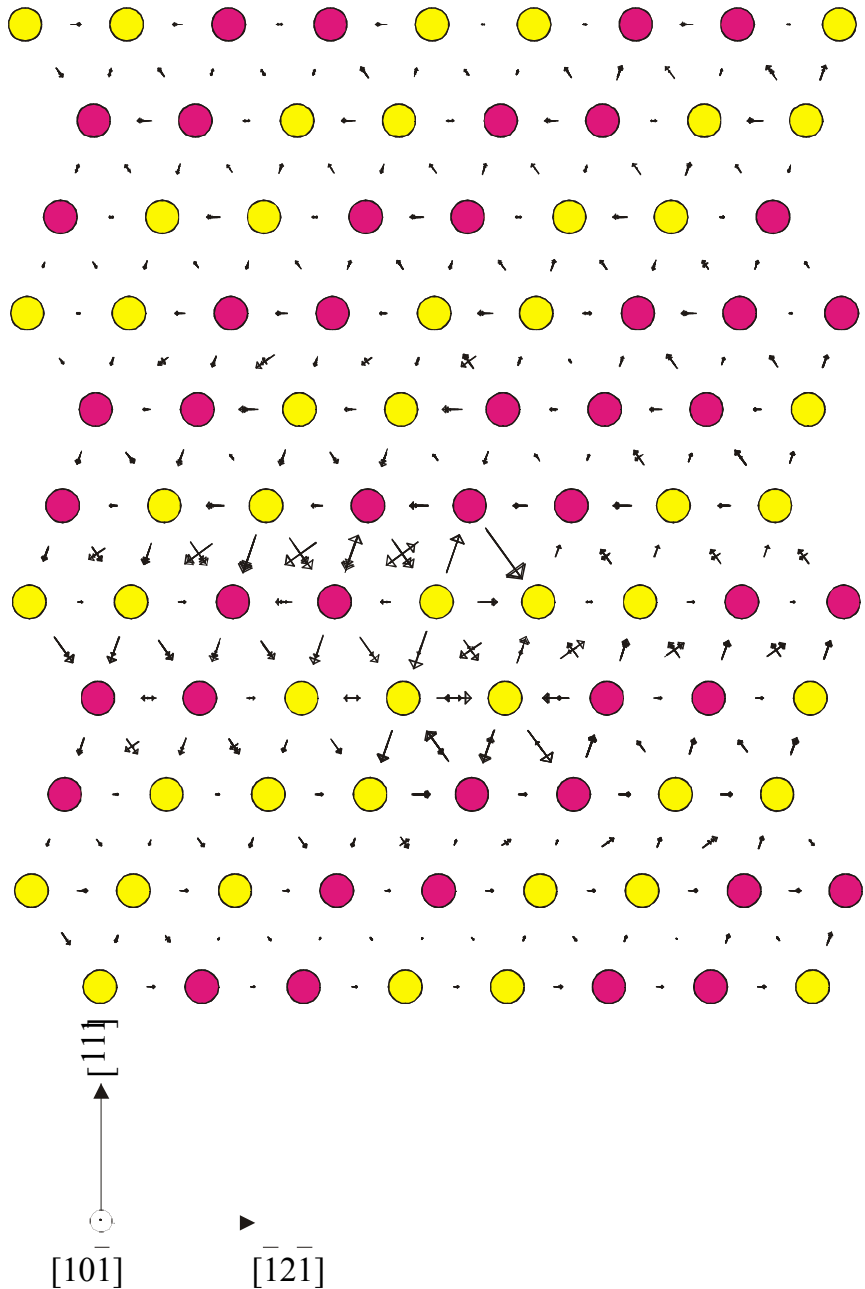


Figure 8.3 The core structure of the  $1/2[1\bar{1}0]$  ordinary  $60^\circ$  mixed dislocation in TiAl depicted by the component of the displacement along the  $[1\bar{2}\bar{1}]$  direction (edge component).

### 8.2.2. $\langle 101 \rangle$ Superlattice Dislocation

Similarly as in the case of ordinary dislocations, the screw orientation of the superdislocation is the most interesting since it gives rise to possible non-planar dissociations and/or core spreading. Previous calculations of Girshick (1997), made using Finnis-Sinclair type central force potentials, indeed predicted that the screw  $[10\bar{1}]$  superdislocation can have two possible core configurations. The first is planar and corresponds to splitting in the  $(111)$  plane according to equation (8.2). The alternative configuration is the non-planar splitting according to the reaction (8.7) into the  $(111)$  and  $(1\bar{1}1)$  planes, forming ribbons of the SISF on these planes.

Panova and Farkas (1995) found in their calculations of the  $\langle 101 \rangle$  superdislocation a non-planar dislocation dissociation into two  $\{111\}$  planes, similarly as in Girshick (1997). However, two different configurations were detected. One with an additional ribbon of the APB on the  $(111)$  plane and another with the APB ribbon on the  $(010)$  plane.

Rao, Woodward, Simmons and Dimiduk (1995) studied the  $\langle 101 \rangle$  superdislocation using the EAM type potential NTA02. Six different line orientations (screw,  $30^\circ$  mixed,  $60^\circ$  mixed, edge,  $120^\circ$  mixed and  $150^\circ$  mixed) were examined for the splitting given by equation (8.1) and three orientations (screw,  $60^\circ$  mixed and  $120^\circ$  mixed) for the splitting given by equation (8.4). The splitting according equation (8.1) was found to be stable for all six dislocation line orientations considered. The dislocation core is in this case planar without any significant out of the  $(111)$  plane component. The

configuration given by equation (8.4) was not found to be stable for any line orientation studied. During relaxation the screw dislocation dissociated further into the configuration described by equation (8.1), while the  $60^\circ$  and  $120^\circ$  mixed dislocations decomposed into two ordinary dislocations  $1/2[1\bar{1}0]$  and  $1/2[11\bar{2}]$  according to the reaction (8.6). The reason behind this behavior is that for this potential SISF, APB and CSF all have rather low energies.

Using our BOP for TiAl we studied the core structure of the screw  $[10\bar{1}]$  superdislocation. We examined the core starting with two initial configurations. In the first case the starting, unrelaxed configuration corresponded to the undissociated  $[10\bar{1}]$  dislocation. In the second case the starting configuration corresponded to dislocation split according to the reaction (8.2) (this configuration was found to be metastable in the study of Girshick 1997). We did not use (8.1) as a starting configuration since no fourfold splitting has been experimentally observed.

In the first case the relaxation resulted in a non-planar configuration shown in Figure 8.4 (screw component) and Figure 8.5 (edge component). This configuration corresponds to splitting according to the reaction (8.7) with two SISFs on the intersecting  $(111)$  and  $(1\bar{1}1)$  planes. Considering the symmetry of the configuration, the width of the two SISF faults should be the same. The reason this is not true in our calculations is that the SISF fault spreading on the  $(1\bar{1}1)$  plane reached the boundary of the simulation block. Configuration (8.7) is obviously sessile with the partial dislocation  $1/3[20\bar{1}]$  locked at the intersection of the two  $\{111\}$  planes. The spread of the core of the

$1/3[20\bar{1}]$  dislocation at the intersection of the  $\{111\}$  planes, seen in Figure 8.4 and Figure 8.5, may indicate that further splitting according to reaction (8.8) takes place resulting in a small ribbon of  $\text{ABP}_{(010)}$  on the  $(010)$  cube plane.

In the second case, where splitting according to the reaction (8.2) was used as the initial configuration, the dislocation core, while retaining its planar character, transformed into a different configuration corresponding to splitting according to (8.3). The resulting relaxed core structures are shown in Figure 8.6 (screw component) and Figure 8.7 (edge component in the  $[\bar{1}2\bar{1}]$  direction). This configuration contains a narrow ribbon of the CSF on the right-hand side (only about 2-3 lattice spacings wide) and a much wider ribbon of the SISF on the left hand side. The APB present in the starting configuration (8.2) disappeared since otherwise it would be identified in Figure 8.7 as a region with zero edge displacement. The planar core confined to the  $(111)$  plane suggests that this configuration is glissile in the  $(111)$  plane. However, the atomic structure of the pair  $1/6[2\bar{1}\bar{1}]+\text{CSF}+1/2[10\bar{1}]$  is rather complex owing to the high energy of CSF. As seen in Figure 8.6 and 8.7, this configuration spreads out of the single  $(111)$  plane. Thus the corresponding Peierls stress may still be high. This has not been investigated in this thesis, but it is proposed as a follow up investigation.

In the calculation for the undissociated dislocation a simulation block consisting of 182 active and 518 inert atoms was used (see Section 3.2), while for the configuration according to (8.2) we used a block consisting of 1075 active and 2822 inert atoms.

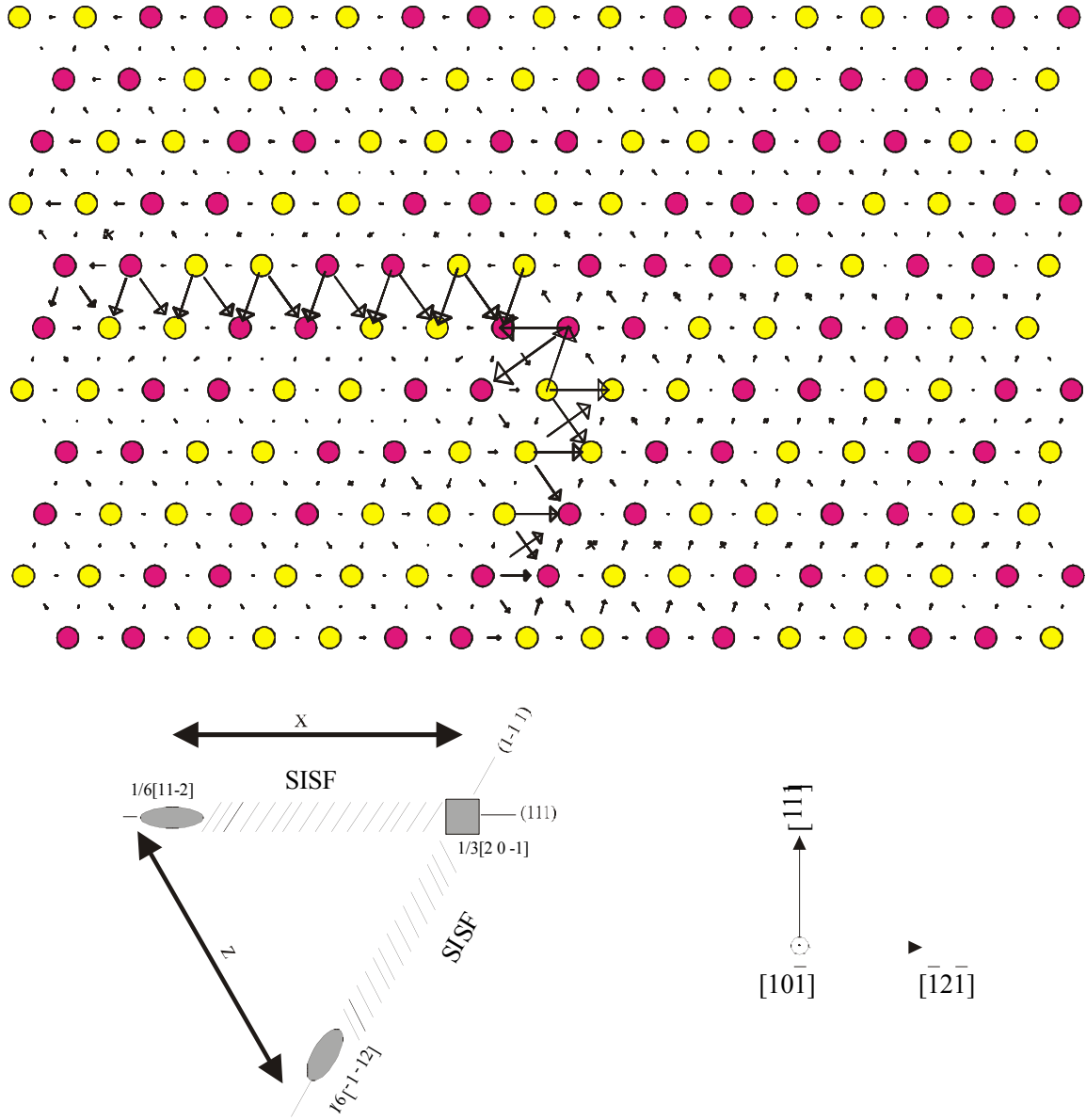


Figure 8.4 The non-planar core of the screw  $[10\bar{1}]$  superdislocation split into two  $\{111\}$  planes, forming a pair of SISFs, depicted by the screw component of the displacement.

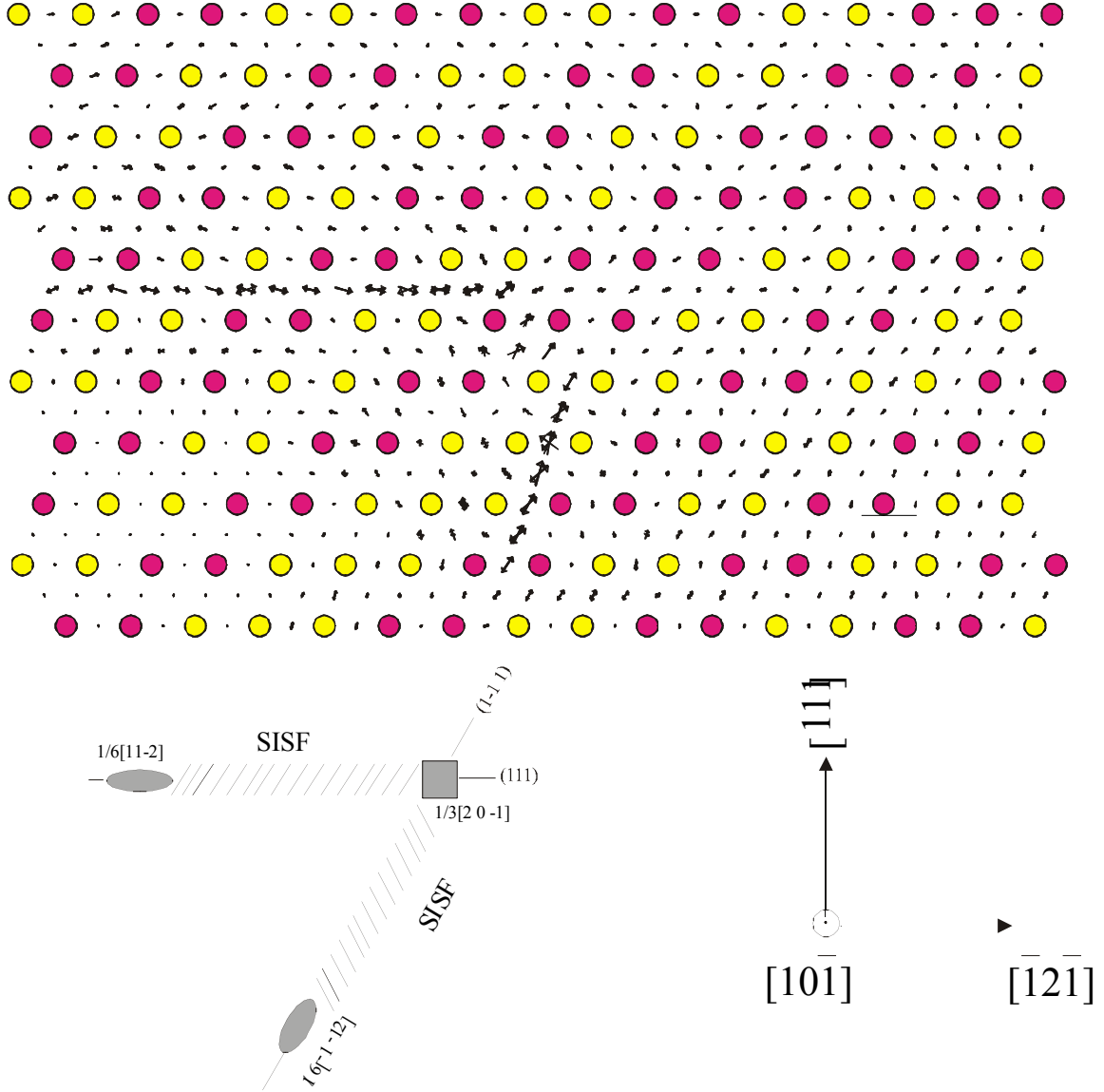


Figure 8.5 The non-planar core of the screw  $[10\bar{1}]$  superdislocation split into two  $\{111\}$  planes, forming a pair of SISFs, depicted by the edge component of the displacement along the  $[\bar{1}2\bar{1}]$  direction. The displacements are significantly smaller than in the case of the screw component therefore a finer scale for the arrows is used in this plot.

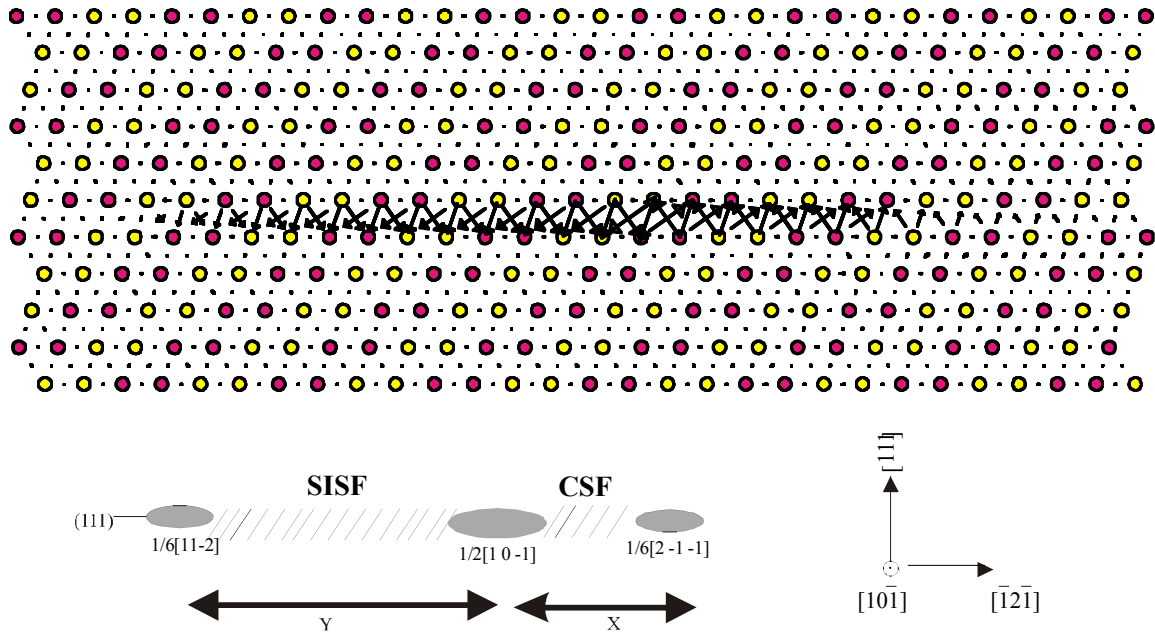


Figure 8.6 The planar core of the screw  $[10\bar{1}]$  superdislocation depicted by the screw component of the displacement.

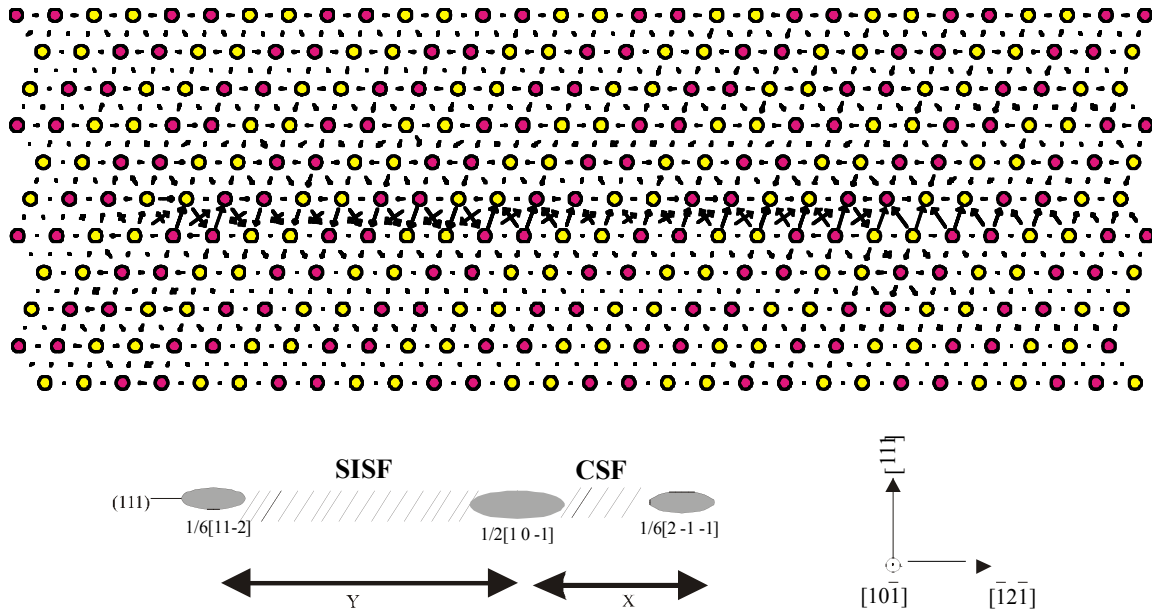


Figure 8.7 The planar core of the screw  $[10\bar{1}]$  superdislocation depicted by the edge component of the displacement in the  $[\bar{1}2\bar{1}]$  direction. The displacements are significantly smaller than in the case of the screw component therefore a finer scale for the arrows is used in this plot.

### 8.3. Elastic Analysis of Ordinary and Super Dislocations in L1<sub>0</sub> TiAl

In order to attain a better physical understanding of the outcomes of atomistic simulations, we used anisotropic theory of elasticity to analyze various splittings of both ordinary dislocations and superlattice dislocations. The elastic theory of dislocations in anisotropic media is standard and full description can be found in Hirth and Lothe (chapter 13), 1982; here we only briefly summarize the basic concepts used. The energy of a dislocation dissociated into two partials separated by a stacking fault type defect can be written as

$$(8.9) \quad E(x) = K_{12} \ln \frac{R}{x} + \gamma(x - r_0) + \sum_{i=1}^2 K_i^{self} \ln \frac{R}{r_0}$$

where  $K_{12}$  is the interaction energy coefficient between the two partials,  $K_i^{self}$  is the self-energy coefficient of the partial  $i$ ,  $x$  is the separation between the partials,  $\gamma$  is the energy of the stacking-fault type defect connecting the two partials,  $R$  is the outer cut-off radius and  $r_0$  the inner cut-off radius, often associated with the width of the dislocation core. Coefficients  $K_i^{self}$  and  $K_{12}$  depend on the Burgers vectors of the partial dislocations, elastic constants and the geometry of the configuration and can be evaluated numerically using the procedures summarized in Hirth and Lothe, 1982. The energy in the above expression is obviously determined only up to an additive constant. Equation (8.9) for the energy can be regrouped in the following way:

$$(8.10) \quad E(x) = K_{12} \ln \frac{Rr_0}{xr_0} + \gamma(x - r_0) + \sum_{i=1}^2 K_i^{self} \ln \frac{R}{r_0}$$

$$= -K_{12} \ln \frac{x}{r_0} + \gamma(x - r_0) + \left( K_{12} + \sum_{i=1}^2 K_i^{self} \right) \ln \frac{R}{r_0}$$

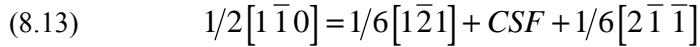
with the last term  $\left( K_{12} + \sum_{i=1}^2 K_i^{self} \right) \ln \frac{R}{r_0}$  representing the elastic energy of the undissociated dislocation. If we denote  $K^{tot} = \left( K_{12} + \sum_{i=1}^2 K_i^{self} \right)$  we can write

$$(8.11) \quad E(x) = -K_{12} \ln \frac{x}{r_0} + \gamma(x - r_0) + K^{tot} \ln \frac{R}{r_0}$$

The equilibrium width of the splitting,  $x_0$ , is obtained from the condition of minimization of  $E(x)$  with respect to  $x$ , i. e.  $\frac{dE(x)}{dx} = 0$ . This gives

$$(8.12) \quad x_0 = \frac{K_{12}}{\gamma}$$

We can now use equation (8.12) to estimate the width of the hypothetical splitting of an ordinary dislocation into two partials according to reaction



In this case  $\gamma = \gamma_{CSF} = 0.412 \text{ Jm}^{-2}$  (see Table 7.3 in Chapter 7). Coefficients  $K_{12}$  and  $K_i^{self}$ , calculated from the elastic theory, and the resulting equilibrium splitting widths  $x_0$  for the screw, 60°-mixed and edge dislocations are summarized in Table 8.1. For all three orientations the equilibrium width of splitting is close to one lattice parameter ( $a_0 = 4.005 \text{ \AA}$ ). Such narrow splittings have no physical meaning. This elastic calculation demonstrates that ordinary dislocations will most likely not dissociate into Shockley partials in one {111} plane. For the screw and 60°-mixed dislocation an alternative is

spreading into two crystallographically equivalent {111} planes, as observed in our atomistic modeling.

<b>Dislocation line orientation</b>	$K_{I2}$ [x 10 <sup>-9</sup> J/m]	$x_0$ [Å]
Screw	0.147051	3.57
60°-mixed	0.201298	4.89
Edge	0.221708	5.38

Table 8.1  $1/2[1\bar{1}0] = 1/6[1\bar{2}1] + CSF + 1/6[2\bar{1}\bar{1}]$  splitting of the ordinary dislocation.

Interaction energy coefficients and equilibrium widths of splitting for the screw, 60°-mixed and edge orientations of the dislocation line.

In the case of the  $[10\bar{1}]$  superdislocation we used anisotropic elasticity to calculate the equilibrium widths of splitting for several possible dissociations of the dislocation in screw orientation. We analyzed the two two-fold splittings, according to reactions (8.4) and (8.5), together with the two threefold splittings according to reactions (8.3) and (8.7). The two latter configurations were found to be metastable in our atomistic simulations.

The energetics of the twofold dissociations is again governed by equations (8.11) and the equilibrium width of this splitting is given by equation (8.12). Thus for the configuration (8.4)

$$(8.14) \quad x_0 = \frac{K_{12}}{\gamma_{SISF}}$$

with  $\gamma_{SISF} = 0.140 \text{ Jm}^{-2}$  ( see Table 7.3 in Chapter 7).

The results for this configuration are summarized in Table 8.2. Note that the energy

$$\text{coefficient of the undissociated dislocation } K^{tot} = \left( K_{12} + \sum_{i=1}^2 K_i^{self} \right) = 1.76335 \times 10^{-9} \text{ J/m}.$$

$K_{12}$ [x 10 <sup>-9</sup> J/m]	$K_1^{self}$ [x 10 <sup>-9</sup> J/m]	$K_2^{self}$ [x 10 <sup>-9</sup> J/m]	$x_0$ [\AA]
0.564550	1.032351	0.1664476	40.32

Table 8.2  $[10\bar{1}] = 1/6[5\bar{1}\bar{4}] + SISF + 1/6[11\bar{2}]$  splitting of the superdislocation. Interaction energy coefficients, self-energy coefficients and equilibrium width of splitting for the screw orientation of the total dislocation.

Similarly, for the splitting according to reaction (8.5) we can write

$$(8.15) \quad x_0 = \frac{K_{12}}{\gamma_{APB}}$$

where  $\gamma_{SISF} = 0.545 \text{ Jm}^{-2}$  ( see Table 7.3). Resulting values for this configuration are shown in Table 8.3. To test the correctness of the calculated values we can verify that energy coefficient of the undissociated dislocation  $K^{tot}$  is in this case the again equal to

$$K^{tot} = \left( K_{12} + \sum_{i=1}^2 K_i^{self} \right) = 1.76335 \times 10^{-9} \text{ J/m}.$$

$K_{12}$ [x 10 <sup>-9</sup> J/m]	$K_1^{self}$ [x 10 <sup>-9</sup> J/m]	$K_2^{self}$ [x 10 <sup>-9</sup> J/m]	$x_0$ [\AA]

0.881674	0.4408370	0.4408370	16.18
----------	-----------	-----------	-------

Table 8.3  $[10\bar{1}] = 1/2[10\bar{1}] + APB + 1/2[10\bar{1}]$  splitting of the superdislocation. Interaction energy coefficients, self-energy coefficients and equilibrium width of splitting for the screw orientation of the total dislocation.

The elastic analysis of the three-fold dissociations is slightly more complicated. The energy of the sessile non-planar splitting according to (8.7) has the following form

$$(8.16) \quad E(x) = -K_{12} \ln \frac{x}{r_0} - K_{13} \ln \frac{x}{r_0} - K_{23} \ln \frac{z}{r_0} + 2\gamma_{SISF}(x - r_0) + K^{tot} \ln \frac{R}{r_0}$$

with  $K^{tot} = K_{12} + K_{13} + K_{23} + \sum_{i=1}^3 K_i^{self}$ . The index 1 refers to the  $1/3[20\bar{1}]$  partial, the index 2 - to the  $1/6[11\bar{2}]$  partial and the index 3 - to the  $1/6[1\bar{1}\bar{2}]$  partial.  $x$  is the separation between the  $1/6\langle 112 \rangle$  partials bounding SISFs and the partial  $1/3[20\bar{1}]$  at the intersection of the  $\{111\}$  planes. Owing to the symmetry of the configuration the distance between the  $1/6\langle 112 \rangle$  partials, denoted as  $z$  (see Figure 8.4, equals  $z = \alpha x$ ; the coefficient  $\alpha = 2\sqrt{(1 + \lambda^2)/(5 + \lambda^2)}$ , where  $\lambda = c/a$ , is determined on the basis of the geometry of the configuration studied.

$K_{12}$ [ $\times 10^{-9}$ J/m]	0.364854
$K_{13}$ [ $\times 10^{-9}$ J/m]	0.364854

$K_{23}$ [x 10 <sup>-9</sup> J/m]	0.199695
$K_I^{self}$ [x 10 <sup>-9</sup> J/m]	0.5010494
$K_2^{self}$ [x 10 <sup>-9</sup> J/m]	0.1664477
$K_3^{self}$ [x 10 <sup>-9</sup> J/m]	0.1664477
$x_0$ [Å]	33.19
$z_0$ [Å]	38.53

Table 8.4  $[10\bar{1}] = 1/6[11\bar{2}] + SISF_{(111)} + 1/3[20\bar{1}] + SISF_{(1\bar{1}1)} + 1/6[1\bar{1}\bar{2}]$  splitting of the superdislocation. Interaction energy coefficients, self-energy coefficients and equilibrium splitting distances for the screw orientation of the total dislocation.

The equilibrium width of splitting,  $x_0$ , is again determined by minimization of (8.16) with respect to x which yields

$$(8.17) \quad x_0 = \frac{K_{12} + K_{13} + K_{23}}{2\gamma_{SISF}}$$

and consequently

$$(8.18) \quad z_0 = \alpha x_0 = \alpha \frac{K_{12} + K_{13} + K_{23}}{2\gamma_{SISF}}$$

The values of  $x_0$  and  $z_0$ , for the SISF energy found using the constructed BOP, are presented in Table 8.4. We again see that  $K^{tot} = K_{12} + K_{13} + K_{23} + \sum_{i=1}^3 K_i^{self} = 1.76335 \times 10^{-9}$  J/m.

The energy of the planar glissile configuration (8.2) depends on two parameters - the width of the APB, denoted as  $x$ , and the width of the SISF, denoted as  $y$

(8.19)

$$E(x,y) = -K_{12} \ln \frac{x}{r_0} - K_{23} \ln \frac{y}{r_0} - K_{13} \ln \frac{x+y}{r_0} + \\ + \gamma_{APB}(x-r_0) + \gamma_{SISF}(y-r_0) + \sum_{i=1}^3 K^{tot} \ln \frac{R}{r_0}$$

with  $K^{tot} = K_{12} + K_{13} + K_{23} + \sum_{i=1}^3 K_i^{self}$ . The index 1 refers to the partial  $1/2[10\bar{1}]$ , the index 2

- to  $1/6[2\bar{1}\bar{1}]$  partial and the index 3 - to  $1/6[11\bar{2}]$  partial. The equilibrium splitting distances  $x_0$  and  $y_0$  are determined by minimizing  $E(x,y)$  with respect to both  $x$  and  $y$

$(\frac{\partial E(x,y)}{\partial x} = \frac{\partial E(x,y)}{\partial y} = 0)$  which yields

$$(8.20) \quad \frac{K_{12}}{x} + \frac{K_{13}}{x+y} = \gamma_{APB} \quad \text{and} \quad \frac{K_{23}}{y} + \frac{K_{13}}{x+y} = \gamma_{SISF}$$

Solving this set of two equations we get the equilibrium widths of splitting  $x_0$  and  $y_0$ . The results are summarized in Table 8.5. As in the previous cases, the energy coefficient

correctly add up to give  $K^{tot} = K_{12} + K_{13} + K_{23} + \sum_{i=1}^3 K_i^{self} = 1.76335 \times 10^{-9} \text{ J/m}$ .

$K_{12}$ [ $\times 10^{-9}$ J/m]	0.432952
$K_{13}$ [ $\times 10^{-9}$ J/m]	0.448722
$K_{23}$ [ $\times 10^{-9}$ J/m]	0.115827

$K_1^{self}$ [x 10 <sup>-9</sup> J/m]	0.4408370
$K_2^{self}$ [x 10 <sup>-9</sup> J/m]	0.1585624
$K_3^{self}$ [x 10 <sup>-9</sup> J/m]	0.1664477
$x_0$ [Å]	9.84
$y_0$ [Å]	33.90

Table 8.5  $[10\bar{1}] = 1/2[10\bar{1}] + APB + 1/6[2\bar{1}\bar{1}] + SISF + 1/6[11\bar{2}]$  splitting of the superdislocation. Interaction energy coefficients, self-energy coefficients and equilibrium splitting distances for the screw orientation of the total dislocation.

In the case of the other planar configuration (8.3) the energy again depends on two parameters - the width of the CSF, denoted as  $x$ , and the width of the SISF, denoted as  $y$

(8.21)

$$E(x, y) = -K_{12} \ln \frac{x}{r_0} - K_{23} \ln \frac{y}{r_0} - K_{13} \ln \frac{x+y}{r_0} + \\ + \gamma_{CSF}(x - r_0) + \gamma_{SISF}(y - r_0) + \sum_{i=1}^3 K^{tot} \ln \frac{R}{r_0}$$

with  $K^{tot} = K_{12} + K_{13} + K_{23} + \sum_{i=1}^3 K_i^{self}$ . The index 1 now refers to the partial  $1/6[2\bar{1}\bar{1}]$ , the index 2 - to  $1/2[10\bar{1}]$  partial and the index 3 - to  $1/6[11\bar{2}]$  partial. The equilibrium splitting distances  $x_0$  and  $y_0$  are again determined by minimizing  $E(x, y)$  with respect to

both  $x$  and  $y$  ( $\frac{\partial E(x, y)}{\partial x} = \frac{\partial E(x, y)}{\partial y} = 0$ ) which yields

$$(8.22) \quad \frac{K_{12}}{x} + \frac{K_{13}}{x+y} = \gamma_{CSF} \quad \text{and} \quad \frac{K_{23}}{y} + \frac{K_{13}}{x+y} = \gamma_{SISF}$$

Solving this set of two equations we obtain the equilibrium widths of splitting  $x_0$  and  $y_0$ .

The results are summarized in Table 8.6. As in all the previous cases, the energy

coefficients correctly add up to give  $K^{tot} = K_{12} + K_{13} + K_{23} + \sum_{i=1}^3 K_i^{self} = 1.76335 \times 10^{-9} \text{ J/m}$ .

$K_{12}$ [ x $10^{-9}$ J/m]	0.432952
$K_{13}$ [ x $10^{-9}$ J/m]	0.115827
$K_{23}$ [ x $10^{-9}$ J/m]	0.448722
$K_1^{self}$ [ x $10^{-9}$ J/m]	0.1585624
$K_2^{self}$ [ x $10^{-9}$ J/m]	0.4408370
$K_3^{self}$ [ x $10^{-9}$ J/m]	0.1664477

$x_\theta$ [Å]	11.14
$y_\theta$ [Å]	38.47

Table 8.6  $[10\bar{1}] = 1/6[2\bar{1}\bar{1}] + CSF + 1/2[10\bar{1}] + SISF + 1/6[11\bar{2}]$  splitting of the superdislocation.

Interaction energy coefficients, self-energy coefficients and equilibrium splitting distances for the screw orientation of the total dislocation.

#### 8.4. Discussion of Results

Let us now take a closer look at the results of both the atomistic simulations and the analysis using anisotropic elasticity.

The elastic calculations predict that the ordinary  $1/2[1\bar{1}0]$  dislocation should remain undissociated since the possible splitting into Shockley partials is very narrow, in the range of one lattice parameter (see Table 8.1). Our atomistic calculations of ordinary dislocations with the screw and  $60^\circ$ -mixed orientations confirm that this is indeed the case; the ordinary dislocation does not display any tendency to dissociate into Shockley partials in one  $\{111\}$  plane (Figure 8.1 and Figure 8.2). Planar cores of this kind have, however, been found in both the Finnis-Sinclair calculations of Girshick (1997) and the EAM calculation of Simmons, Rao and Dimiduk (1997). The inclusion of covalent bonding in the Bond Order results in a very high energy of CSF ( $412 \text{ J/m}^2$ ) which disfavors such splitting. Moreover BOP accounts more properly for the changes in local bonding which may also be very important in the core of the partials. Thus in our calculations the cores of both the screw and  $60^\circ$ -mixed dislocation are always non-planar,

spread into two intersecting planes of the {111} type, namely (111) and (11 $\bar{1}$ ) for the 1/2[1 $\bar{1}$ 0] dislocation. This core configuration was found to be unique and no, even higher energy planar core, was detected. The non-planar core suggests that these dislocations will be difficult to move. This is, presumably, the reason why ordinary dislocations do not participate in the deformation of the single phase TiAl at lower temperatures. The non-planar core imposes an energy barrier hindering the motion of the dislocation. Only at elevated temperatures thermal activation can assist in overcoming the energy barrier increasing thus the mobility of ordinary dislocations which then play a role in the plastic yielding. To investigate the mobility of these dislocations it would be necessary to study the influence of applied stresses on the dislocation cores and evaluate the corresponding Peierls stresses needed to move the dislocation through the crystal. This study has not been performed in this thesis. However, it will be carried out in the near future and preliminary calculations, indeed, indicate a high Peierls stress for the ordinary screw dislocations.

As expected, the ⟨101] superdislocation displays more complex behavior than its ordinary counterpart. The results of our computer simulation exhibit a clear preference for splitting, since for both starting configurations we obtained relaxed structures corresponding to dissociation into partial dislocations. When using the singular ⟨101] dislocation as the starting configuration, the originally undissociated dislocation transformed during the process of relaxation into a dissociated dislocation composed of three partial dislocations (reaction (8.7)) with displacement spreading into two intersecting {111} planes.

For the other starting configuration - the planar splitting with three partial dislocations separated by SISF and APB (reaction (8.2)), the relaxation resulted in a core transformation to another planar configuration, the dissociation according to reaction (8.3). This is unlike in the study of Girshick (1997) where splitting according to (8.2) was predicted. Both (8.2) and (8.3) are threefold splittings involving the same types of partial dislocations, but in the case of (8.2) the splitting occurs via SISF and APB, while in the case of (8.3) it occurs via SISF and CSF. Since our potential, in agreement with ab-initio calculations, predicts the energy of CSF ( $0.412 \text{ J/m}^2$ ) to be lower than that of APB ( $0.545 \text{ J/m}^2$ ), preference for configuration (8.3) is logical. In the study of Girshick (1997) the central-force based Finnis-Sinclair potential used predicts the two energies to be virtually the same ( $\gamma_{APB} = \gamma_{CSF} = 0.275 \text{ Jm}^{-2}$ ).

The anisotropic elasticity analysis does not allow us to compare directly the energies of the two competing metastable configurations, the non-planar (8.7) and the planar (8.3), since the energies are determined up to an additive constant. On the other hand, the precision of atomistic simulations is not sufficient to decide which of the two configurations is energetically favored. Hence, the conclusion which can be drawn from this study is that the two metastable configurations of the  $\langle 101 \rangle$  superdislocation probably possess very similar energies and which of them is favored may depend sensitively on relatively minor deviations from ideal situation studies, such as local stresses, departure from stoichiometry, temperature, etc.

In the case of the planar metastable configuration dissociated according to the reaction (8.3) we can also compare the actual splitting width obtained from the atomistic

simulation with that predicted by the elastic estimates. As mentioned earlier, due to the relatively high energy of CSF ( $0.412 \text{ J/m}^2$ ) the width of the CSF should be small. The elastic calculations predict  $11.14 \text{ \AA}$ , which is about 3 lattice spacings. The width of the SISF, which has much lower energy ( $0.140 \text{ J/m}^2$ ), is larger – the value estimated from elastic calculations is  $38.47 \text{ \AA}$  (see Table 8.6). The width of the ribbon of the CSF cannot be meaningfully estimated from Figure 8.7. However, the total width of the splitting, including both the CSF and SISF, can be determined with much higher precision. In the atomistically simulated configuration this is about  $52 \text{ \AA}$ . The elastic estimate of this value is  $49.61 \text{ \AA}$  ( $49.61 = 11.14 + 38.47$ ) which is, indeed, very close to the atomistic result. Unfortunately, we are not able to do a similar comparison for the non-planar dissociation, (Figure 8.4), because in this case the SISF almost reached the block boundary which affects the width of splitting.

The existence of two metastable dislocation dissociations of the  $\langle 101 \rangle$  superdislocation, that are energetically very close, may have important implication for the deformation behavior of  $L1_0$  TiAl. Since the ordinary  $1/2[1\bar{1}0]$  dislocations have sessile non-planar cores – as our calculations suggest – the plastic deformation at lower temperatures will be governed by the  $\langle 101 \rangle$  superdislocations, assuming that these dislocations can move. The mobility of the  $\langle 101 \rangle$  superdislocation is obviously closely related to their core structure. If there were a strong energetic preference for the non-planar splitting over the planar one, the superdislocations would also be immobile at low temperature. On the other hand, if the planar core is energetically favored, or at least the energy difference between the two competing configurations is very small, the moving

superdislocations will possess the planar configuration which is likely to be much more glissile. The results of our calculations indicate that the latter is the case, and therefore superdislocation activity can be expected at lower temperatures. This is, indeed, observed in single phase TiAl where several experimental studies identified the superdislocation slip as the major deformation mode at lower temperatures (see e.g. Inui *et al.* 1997). However, the situation is different in the lamellar TiAl where ordinary dislocations and twinning dominate at lower temperatures. Explanation of these phenomena may require study of interaction of dislocations with lamellar interfaces which is another possible broad topic of future studies that can be made with the help of the BOPs developed in this study.

As already mentioned, the next logical step after finding the competing metastable core configurations would be to investigate the influence of the applied external stresses on the core structures and dislocation motion. As often happens, imposing external stresses can lead to dramatic changes in the core structure, causing, for example, a transformation of one configuration into another. Again these studies are obviously part of the short-term future research based on the constructed potentials for TiAl.

## **9. SUGGESTIONS FOR FUTURE RESEARCH**

Computer modeling has long become an integral part of the materials science research. It represents a powerful tool for structural analyses as well as in studies of broad variety of materials properties and it can be used to complement and verify theories proposed by experimental and analytical studies. Atomistic simulation techniques, employing different schemes for the description of atomic interactions, can help to attain deeper understanding of the key properties and mechanisms governing the behavior of the material. They provide an insight into the processes at the atomic level that is needed for the analysis of global phenomena taking place at larger length scales. Results presented in this thesis demonstrate a number of important implications of the microscopic characteristics of dislocations for the macroscopic mechanical behavior.

The Bond Orders Potentials for TiAl, developed in the course of this work, are well suited for studies of this type. Being based on the tight binding theory they are capable to capture all the important aspects of the covalent bonding in this, predominantly metallic, material. It would be desirable to have similar potentials constructed for other materials with mixed metallic and covalent, directional bonding. In our research group there is currently an ongoing parallel project focusing on the bond order potentials for elemental transition metals, such as Mo, Nb, W and Ta. Work on the more complex potential for Mo-Si alloys has also begun and other, possibly also non-metallic materials may follow. The experience gained during the construction of the BOPs for TiAl forms a basis for the development of potentials for other alloys. For, example, as discussed in Chapter 6, a

modification of the environment-dependent may be needed to accommodate the change in the nearest neighbor distance when using as a basis a potential for a pure element in a compound material.

There is still some room for improvements of the potential for TiAl. Among the possible amendments that could be made is such alteration of the potentials, that not only the Ti-Ti part, but also the part describing Al-Al interaction, be based on an existing potential for the pure element. A necessary precursor for this is obviously the development of bond order potentials for fcc Al. The availability of such potential would decrease the number of parameters that need to be determined for the potentials for TiAl, and a more consistent and comprehensive scheme would thus be established.

However, further important studies that have not been made in this thesis, can still be carried out using the developed potentials for TiAl. Since the work presented in this thesis focuses on structural features, the next logical step is the investigation of the mechanisms of dislocation glide. As a continuation of this work, the influence of applied external stresses should be investigated for all types of dislocations considered. Applying external stress to the crystal can be done via imposing a strain field corresponding to the given stress calculated from Hook's law. Structural changes and possible transformations of the dislocation core as a function of the applied stress can be examined in this manner. The quantity of interest is the Peierls stress - the threshold stress needed to move the dislocation through the lattice. Study of this kind, however, requires another major effort since it represents a new class of problems that have to be linked with experiments, and theories of dislocation motion. Studying the dislocation glide is therefore a task for

another thesis. In the case of the ordinary  $1/2\langle 110 \rangle$  dislocation where both the screw and  $60^\circ$  orientations display non-planar sessile cores, very interesting results can be expected. The sessile core of the dislocations affects significantly their mobility and, therefore, presumably, very high stresses will be needed for their motion at 0K. At finite temperatures their movement will be assisted by thermal activations and, similarly as in the case of bcc-metals (see e.g. Duesbury, 1989) a strong temperature dependence of the related glide stress can be expected.

Secondly, in this thesis we concentrated only on dislocations that produce plastic deformation by glide, while the other important deformation mode in the PST crystals – twinning – was not investigated. Specifically, no studies of the  $1/2\langle 112 \rangle$  ordinary dislocation, which is believed to play a crucial part in the process of twinning, were included. It would be therefore desirable to investigate the properties of this dislocation, namely the character of its core. First, the energetics of the core dissociation into various partials and related stacking fault-type defects need to be studied in detail. This is, however, also a task for another major study. For example experiments of Inkson and Humphreys, 1995, suggest a splitting according to the reaction



where SESF stands for the superlattice extrinsic stacking fault. However, many other possible reactions may take place, in particular if the splittings are spread in several layers. Indeed, more recent experimental work on the core structures of the  $1/2\langle 112 \rangle$  and  $\langle 101 \rangle$  dislocations (Inkson, 1998) discusses the possibility of splitting to partial

dislocation lying on two parallel  $\{111\}$  slip planes. Such cores would involve three partial dislocations, one of which is delocalized on two  $\{111\}$  planes, forming two ribbons of stacking faults. Since this kind of splitting cannot be safely identified by weak-beam transmission electron microscopy, it represents another interesting research topic for atomistic simulations with our potentials for TiAl.

The  $1/2\langle 112 \rangle$  ordinary dislocation can also play an important role as partial dislocation in the splitting of the  $\langle 101 \rangle$  superdislocation in reaction (8.6). Calculation of this splitting is also one of the possible goals of the future research.

Apart from studies of dislocations, there are other attractive directions for research in TiAl. As discussed earlier, in Chapter 2, the properties of TiAl change dramatically with varying the content of Al in the material. It would be very interesting to find out, using atomistic simulations, how compositional changes affect extended defects. This could also serve as another test of the applicability of bond order potentials to wide variety of possible local environments encountered in TiAl. Furthermore, our bond order potentials for TiAl have been shown to predict the correct structure and basic parameters, such as lattice constant, for 3:1 composition, i. e.  $Ti_3Al$  (see Chapter 7). Since  $Ti_3Al$  is an important component of the lamellar structure, its properties should also be investigated further using our potentials.

Structural and compositional studies of interfaces and boundaries in lamellar TiAl represent another area of possible future research. Segregation of excess Ti into boundaries in the PST crystal can have important effects on their energetics, which in turn may influence the overall mechanical behavior of the PST crystals. A study of such

segregation was carried out by Ito and Vitek, 1998, using the Finnis Sinclair potential.

Using the bond order potential capable of capturing effects of directional bonding might bring a new insight into this problem.

Finally, as an ultimate research goal, a combined study of interactions of dislocations with interfaces can be carried out. In the complex structure of PST crystals such interaction is very difficult to analyze by purely analytical or experimental means; therefore an atomistic simulation of this kind would contribute significantly to our understanding of dislocation-interfaces interactions and thus to comprehension of the main phenomena controlling the deformation behavior of lamellar TiAl.

## BIBLIOGRAPHY

Ackland, G. J., Tichy, G., Vitek, V., and Finnis, M. W., 1987, *Philos. Mag. A* **56**, 735

Andersen, O.K and Jepsen, O., 1984, *Phys. Rev. Lett.* **53**, 2571

Andersen, O. K., 1975, *Phys. Rev. B* **12**, 3060

Andersen, O. K., Jepsen O. and Glötzel D., 1985, in: "Highlights of Condensed-Matter Theory", edited by F. Bassani, F. Fumi, M. P. Tossi, (Amsterodam, Oxford, New York, Tokyo: North Holland), 59

Andersen, O.K, Jepsen, O. and Krier, G., 1994, in: "Lectures on Methods of Electronic Structure Calculations", edited by V. Kumar *et al.*, World Scientific, Singapore, 63

Aoki, M., 1993, *Phys. Rev. Lett.* **71**, 3842

Beer, N. and Pettifor, D.G., 1984, in "Electronic Structure of Complex Systems", edited by P. Phariseau and W.M. Temmerman, (New York: Plenum), 769

Blaha, P., Schwartz, K., Sorantin, P., and Trickey, S.B., 1990, *Comp. Phys. Commun.* **59**, 399

Bowler, D.R., Aoki, M., Goringe, C.M., Horsfield, A.P. and Pettifor,D.G., 1997,  
*Modelling and Simulation in Mat. Sci. Eng.* **5**, 199

Court, S. A., Vasudevan, V. K., and Fraser, H. L., 1990, *Philos. Mag. A* **61**, 141

Cyrot-Lackmann, F., 1968, *J. Phys. Chem. Solids* **29**, 1235

Daw, M. S., and Baskes, M. I., 1984, *Phys. Rev. B* **29**, 6443

Denquin A. and Naka S., 1993, *Philos. Mag. Lett.*, **68**, 13

Dimiduk D. M., Miracle D. B. and Ward C. H., 1992, *Mat. Sci. Technol.*, **8**, 367

Dimiduk, D.M., 1998, *Intermetallics* **6**, 613

Duesbery, M. S., 1989, in “Dislocations in Solids”, edited by F. R. N. Nabarro, (Amsterdam: North Holland) Vol. **8**, p. 67

Dimiduk, D.M.,1999, *Mat. Sci. Eng. A* **263**, 281

Duesberry, M.S. and Richardson, G.Y.,1991, *CRC Critical reviews in Solid State and Materials Science* **17**, 1

Ehmann, J. and Fahnle, M., 1998, *Philos. Mag. A* **77**, 701

Farkas, D., 1994, *Modelling Simul. Mater. Sci. Engng.* **2**, 975.

Feynman, R. P., 1939, *Phys. Rev.* **56**, 340

Finnis, M. W., and Sinclair, J. E., 1984, *Philos. Mag. A* **50**, 45

Foulkes, W. M. C., and Haydock, R., 1989, *Phys. Rev. B* **39**, 12520

Fu C. L. and Yoo M. H., 1990, *Phys. Rev. Lett.*, **62**, 159

Fujiwara, T., Nakamura, A., Hosomi, M., Nishitani, S. R., Shirai, Y. and Yamaguchi, M., 1990, *Philos. Mag. A* **61**, 591

Girshick, A. and Vitek, V., 1995, in “High-Temperature Ordered Intermetallic Alloys VI”, edited by J. A. Horton, I. Baker, S. Hanada, R. D. Noebe and D. S. Schwartz, Mat. Res. Soc. Symp. Proc., vol. 364, Part 1, (Pittsburgh, PA: Materials Research Society), p. 145

Girshick, A., 1997, Ph.D. Thesis, University of Pennsylvania

Girshick, A., Bratkovsky, A. M., Pettifor, D. G., and Vitek, V., 1997, *Philos. Mag. A* **77**, 981

Harris, J., 1985, *Phys. Rev. B* **31**, 1770

Haydock, R., 1980, *Solid State Physics*, edited by H. Ehrenreich and D. Turnbull, (New York: Academic Press) Vol. **35**, p. 216

Hazzledine P. M. and Kad B. K., 1995, *Mater. Sci. Eng. A*, **192/193**, 340

Hellmann, H., 1937, *Einführung in die Quantenchemie* (Leipzig: Deuticke)

Hemker, K.J., Viguer, B., Mills, M.J., 1993, *Materials Science and Engineering A* **164**, 391

Hirth, J. P., and Lothe, J., 1982, *Theory of Dislocations* (New York: Wiley-Interscience)

Hohenberg, P., and Kohn, W., 1964, *Phys. Rev.* **136**, B 864

Horsfield, A. P., and Bratkovsky, A. M., 1996, *Phys. Rev. B* **53**, 15381

Horsfield, A. P., Bratkovsky, A. M., Fearn, M., Pettifor, D. G., and Aoki, M., 1996, *Phys. Rev. B* **53**, 12694

Hug, G., Loiseau, A., and Lasalmonie, A., 1986, *Philos. Mag. A* **54**, 47

Hug, G., Loiseau, A., and Veyssiere, P., 1988, *Philos. Mag. A* **57**, 499

Hug, G., Phan-Courson, I., and Blance, G., 1995, *Mater. Sci. Eng. A* **192/193**, 673

Inkson, B. J., and Humphreys, C. J., 1995, *Philos. Mag. Lett.* **71**, 307

Inkson, B. J., 1998, *Philos. Mag A* **77**, 715

Inui H., Nakamura A., Oh M. H., Yamaguchi M., 1992a, *Philos. Mag. A*, **66**, 557

Inui H., Oh M. H., Nakamura A., and Yamaguchi M., 1992b, *Philos. Mag. A*, **66**, 539

Inui H., Oh M. H., Nakamura A. and Yamaguchi M., 1992c, *Acta Metall. Mater.*, **40**,  
3095

Inui, H., Toda Y. and Yamaguchi M., 1993, *Philos. Mag. A*, **67**, 1315

Inui, H., Matsumuro, M., Wu, D.-H., and Yamaguchi, M., 1997 , *Philos. Mag. A* **75**, 395

Ito, K. and Vitek,V., 1998, *Acta Mater* **46**, 5435

Kohn, W., and Sham, L. J., 1965, *Phys. Rev.* **140**, A 1133

Lanczos, C., 1950, *J. Res. Natl. Bur. Stand.* **45**, 225

Li, Z. X., and Whang, S. H., 1992, *Mater. Sci. Eng. A* **152**, 182

Lipsitt, H. A., Shechtman, D., and Schafrik, R. E., 1975, *Metall. Transactions A* **6A**, 1991

Lu L., Siegl R., Girshick A., Pope D.P. and Vitek V., 1996, *Scripta Materialia* **34**, 971

M. Methfessel, 1988, *Phys. Rev. B*, **38**, 1537

Milstein, F., Fang, H. E. and Marshall, J., 1994, *Philos. Mag A* **70**, 621

Min-Chul Kim, M. Nomura, V. Vitek and D. P. Pope: in “High-Temperature-Ordered Intermetallic Alloys VIII”, edited by E. George, M. Mills and M. Yamaguchi, MRS Symposium Proceedings, Vol. 552, p. KK3.1.1, 1999

Mishin, Y. and Herzog, C., 2000, *Acta mater.* **48**, 589

McCullough C., Valencia J. J., Levi C. G. and Mehrabian R., 1989, *Acta Metall.*, **37**, 1321

Morris, D. G., Gunter, S., and Leboeuf, M., 1994, *Philos. Mag. A* **69**, 527  
Nguyen-Manh, D., Pettifor, D. G., Shao, G., Miodownik, A. P., and Pasturel, A., 1996,  
*Philos. Mag. A* **74**, 1385

Nguyen-Manh, D., Pettifor, D.G., Znam , S., and Vitek, V., 1998, in "Tight-Binding  
Approach to Computational Materials Science", P.E.A. Turchi, A. Gonis and L.  
Colombo, ed., Vol 491, Materials Research Society, Pittsburgh, p.353.

Nguyen-Manh, D., Pettifor, D.G. and Vitek, V., 2000, *Phys. Rev. Lett.* **85**, 4136  
Nowak, H.J, Andersen, O.K., Fujiwara, T., Jepsen, O. and Vargas, P., 1991, *Phys. Rev.B*  
**44**, 3577

Paidar, V., Wang, L.G., Sob, M. and Vitek, V., 1999, *Modelling and Simulation in Mat.  
Sci. Eng.* **7**, 369

Panova, J. and Farkas, D., 1995, in "High-Temperature Ordered Intermetallic Alloys VI",  
edited by J. Horton, I. Baker, S. Hanada, R. D. Noebe and D. Schwartz, Vol. 364,  
(Materials Research Society, Pittsburgh) p. 151

Pearson W. B., 1958, *A Handbook of Lattice Spacings And Structures of Metals and  
Alloys*, vol. **2**, (New York: Pergamon Press)

Pettifor, D. G., 1977, *J. Phys F: Met. Phys.* **7**, 613

Pettifor, D. G., 1989, *Phys. Rev. Lett.* **63**, 2480

Pettifor, D.G. and Aoki, M., 1991, *Phil. Trans. Roy. Soc. London A* **334**, 439

Pettifor, D. G., 1995, *Bonding and Structure of Molecules and Solids* (Oxford: Oxford University Press)

Shechtman, D., Blackburn, M. J., and Lipsitt, H. A., 1974, *Metall. Transactions* **5**, 1373

Siegl, R., Vitek, V., Inui, H., Kishida, K., and Yamaguchi, M., 1997, *Philos. Mag. A* **75**, 1447

Simmons, J. P., Rao, S. I., and Dimiduk, D. M., 1993, in "High-Temperature Ordered Intermetallic Alloys V", edited by I. Baker, R. Darolia, J. D. Whittenberger and M. H. Yoo, Vol. 288, (Materials Research Society, Pittsburgh) p. 335

Simmons, J. P., Rao, S. I., and Dimiduk, D. M., 1997, *Philos. Mag. A* **75**, 1299

Simmons, G., and Wang, H., 1971, *Single Crystal Elastic Constants and Calculated Aggregate Properties: A Handbook*, (London: M. I. T. Press)

Skriver, H.L., 1984, *The LMTO Method*, Springer, New York

Slater, J. C., and Koster, G. F., 1954, *Phys. Rev.* **94**, 1498

\_ob, M. and Vitek, V., 1996, in "Stability of Materials: NATO Advanced Science Institute", A. Gonis, P.E.A. Turchi and J. Kudrnovsky, ed., Plenum Press, New York, p.449

\_ob, M., Wang, L.G. and Vitek, V., 1997, *Comp. Mat. Sci.* **8**, 100

Song Y., Tang S. P., Xu J. H., Mryasov O. N., Freeman A. J., Woodward C., Dimiduk D. M., 1994, *Philos. Mag. B*, **70**, 987

Sriram, S., Vasudevan, V. K., and Dimiduk, D. M., 1995, *Mater. Sci. Eng. A* **192/193**, 217

Stechel, E.B., Williams, A.R. and Feibelman, P.J., 1994, *Phys. Rev. B*, **49**, 10008

Stucke, M. A., Vasudevan, V. K., and Dimiduk, D. M., 1995, *Mater. Sci. Eng. A* **192/193**, 195

Sutton, A. P., Finnis, M. W., Pettifor, D. G., and Ohta, Y., 1988, *J. Phys. C* **21**, 35

Turchi P. and Ducastelle F., 1985, in "The Recursion Method and Its Applications", edited by D.G. Pettifor and Weaire, Springer-Verlag, Solid-State Science, vol. 58.

Tanaka, K., Ichitsubo, T., Inui, H., Yamaguchi, M., and Koiwa, M., 1996, *Philos. Mag. Lett.* **73**, 71

Vitek, V., 1968, *Philos. Mag. A* **18**, 773

Vitek, V., Perrin, R.C. and Bowen, D.K., 1970, *Philos. Mag. A* **74**, 337

Vitek, V., 1992, *Progr. Mater. Sci.* **36**, 1

Vitek, V., Ito, K., Siegl, R. and Znam, S., 1997a, *Mat. Sci. Eng. A* **240**, 752

Vitek, V., Girshick, A., Siegl, R. and Yamaguchi, M., 1997b, in "Properties of Complex Inorganic Solids", A. Gonis., A.-M. Meike and P.E.A. Turchi, ed., Plenum press, New York, p.355

Wiezorek, J. M. K., and Humphreys, C. J., 1995, *Scripta Met. Mater.* **33**, 451

Woodward C., Kajihara S., 1998, *Phys. Rev. B* **57**, 13459

Woodward C., MacLaren J. M. and Rao S., 1991, in "High-Temperature Intermetallic

Alloys IV,” edited by L. A. Johnson, D. P. Pope, J. O. Stiegler, Mat. Res. Soc. Symp. Proc., vol. 213, (Pittsburgh, PA: Materials Research Society), 715  
Yamaguchi, M., Vitek, V., Pope, D. P., and Umakoshi, Y., 1981, *Philos. Mag. A* **43**, 1265

Yamaguchi M. and Inui H., 1993, in ”Structural Intermetallics”, edited by R. Darolia, J.

Lewandowski, C. T. Liu, P. L. Martin, D. B. Miracle and M. V. Nathal, Proc. of Internat. Symp. on Structural Intermetallics, Seven Springs, PA, USA, Sept. 26-30, 1993, (Warrendale, PA: TMS Publications), 127

Yamaguchi, M., Inui, H., Kishida, K., Matsumuro, M., and Shirai, Y., 1995, in “High-Temperature Intermetallic Alloys VI, Part 1”, edited by J. A. Horton, I. Baker, S. Hanada, R. D. Noebe and D. S. Schwartz, Mat. Res. Soc. Symp. Proc., vol. 364, (Pittsburgh, PA: Materials Research Society), p. 3